**UNIVERSIDADE FEDERAL DE SANTA CATARINA**
**PROGRAMA DE PÓS-GRADUAÇÃO EM ENGENHARIA MECÂNICA**

Hermínio Tasinafo Honório

TESE DE DOUTORADO

# A STABILIZATION TECHNIQUE FOR TREATING NUMERICAL INSTABILITIES IN THREE-DIMENSIONAL POROELASTICITY

Orientador: Clovis R. Maliska

Florianopólis
2018

Hermínio Tasinafo Honório

# A STABILIZATION TECHNIQUE FOR TREATING NUMERICAL INSTABILITIES IN THREE-DIMENSIONAL POROELASTICITY

Tese de Doutorado submetida ao Programa de Pós-Graduação em Engenharia Mecânica para a obtenção do grau de Doutor em Engenharia Mecânica.

Orientador: Clóvis R. Maliska

Florianopólis
2018

Ficha de identificação da obra elaborada pelo autor, através do Programa de Geração Automática da Biblioteca Universitária da UFSC.

Honório, Hermínio Tasinafo
A stabilization technique for treating numerical instabilities in three-dimensional poroelasticity / Hermínio Tasinafo Honório ; orientador, Clovis R. Maliska, 2018.
138 p.

Tese (doutorado) - Universidade Federal de Santa Catarina, Centro Tecnológico, Programa de Pós Graduação em Engenharia Mecânica, Florianópolis, 2018.

Inclui referências.

1. Engenharia Mecânica. 2. poroelasticidade. 3. estabilização. 4. volumes finitos. 5. malhas não estruturadas. I. Maliska, Clovis R.. II. Universidade Federal de Santa Catarina. Programa de Pós-Graduação em Engenharia Mecânica. III. Título.

Hermínio Tasinafo Honório

# A STABILIZATION TECHNIQUE FOR TREATING NUMERICAL INSTABILITIES IN THREE-DIMENSIONAL POROELASTICITY

Esta tese de doutorado foi julgada adequada para a obtenção do título de “Doutor em Engenharia Mecânica”, e aprovada em sua forma final pelo Programa de Pós-Graduação em Engenharia Mecânica.

Florianopólis, 21 de Maio 2018.

Prof. Jonny Carlos da Silva, Dr.Eng., Coordenador

Clóvis R. Maliska, Ph.D., Orientador

**BANCA EXAMINADORA**

Clóvis R. Maliska, Ph.D., Presidente

Marcio Arab Murad, Dr.Eng., Relator

Leonardo José do Nascimento Guimarães, Ph.D.

Sérgio Peters, Dr.Eng.

Eduardo Alberto Fancello, Dr.Eng.

António Fábio Carvalho da Silva, Dr.Eng.

# AGRADECIMENTOS

A todos os integrantes do SINMEC, que de uma forma ou de outra contribuíram para a realização desta tese ao longo desses 4 anos. Em especial ao Ricieri e Gustavo pelas constantes discussões em torno de diferentes aspectos da geomecânica.

À Tatiane, por colocar ordem na casa e proporcionar um ambiente profissional e ao mesmo tempo descontraído.

Ai professori Carlo Janna e Massimiliano Ferronato per avermi ricevuto in Italia e per avermi proporzionato le condizioni ideale per sviluppare questa tesi. Vorrei ringraziare anche per le partite di Tetris dopo pranzo.

Ao professor Maliska, pela confiança depositada em mim, pelas inúmeras discussões, pelas oportunidades oferecidas e por toda a orientação dispendida desde a escolha do tema à defesa da tese.

Aos meus pais, por todo o amor, carinho e dedicação que nunca me faltaram desde que cheguei ao mundo.

Aos meus irmãos, pelo exemplo, por estarem presentes, e por me darem sobrinhos lindos.

À minha namorada e esposa Isabelle, pelos 11 anos de companheirismo, cumplicidade, paciência, dedicação e amor. Devo deixar registrado que apesar dela não ter sequer lido o texto (os agradecimentos ela vai ler), eu não posso imaginar como seria esta tese sem sua presença ao meu lado.

*“O homem vangloria-se de ter imitado o vôo das aves com uma complicação técnica que elas dispensam.”*

Carlos Drummond de Andrade

# CONTENTS

# LIST OF FIGURES

# LIST OF TABLES

# LIST OF SYMBOLS

## Latin Letters

| | |
|---|---|
| $\mathbb{A}$ | Global matrix accounting for the accumulation terms |
| $\mathbb{B}$ | Gradient operator |
| $\mathbb{B}_s$ | Symmetric gradient operator |
| $b^p$ | Source term of the mass conservation equation |
| $\tilde{b}^p$ | Source term of the mass conservation equation due to PIS |
| $\mathbf{b^u}$ | Source term of the stress equilibrium equations |
| $\mathbb{C}$ | Fourth-order constitutive tensor or constitutive matrix |
| $C$ | Component of the constitutive matrix |
| $\mathbf{C}^e$ | Matrix containing the global coordinates of the element vertices |
| $c_f$ | Fluid compressibility |
| $c_s$ | Solid compressibility |
| $\mathbf{D}$ | Matrix containing the shape function local derivatives |
| $G$ | $2^{nd}$ Lamè's parameter (shear modulus) |
| $\mathbf{g}$ | Acceleration gravity vector |
| $\mathbf{G}_{ip}$ | Local matrix accounting volumetric flux crossing *ip* |
| $\mathbf{H}_{ip}$ | Local matrix accounting Darcy velocity crossing *ip* |
| $\tilde{\mathbf{H}}_{ip}$ | Local matrix accounting for PIS |
| $h$ | Characteristic length of the element |
| $\mathbb{H}$ | Global matrix accounting for diffusive fluxes |
| $\tilde{\mathbb{H}}$ | Global matrix accounting for PIS |
| $\mathbf{I}$ | Second-order identity tensor |

| | |
|---|---|
| $\mathbf{J}$ | jacobian matrix |
| $\mathbf{K}$ | Absolute permeability tensor |
| $\mathbf{L}_{ip}$ | Local matrix accounting for the pore pressures on *ip* |
| $\mathbb{L}$ | Global matrix pore pressures |
| $L_d$ | Diffusive length |
| $L_x$ | Diffusive length in x direction |
| $L_y$ | Diffusive length in y direction |
| $L_z$ | Diffusive length in z direction |
| $M$ | Biot modulus |
| $m$ | Number of vertices of the element |
| $\dot{m}$ | Mass flux |
| $\mathbf{M}_{ip}$ | Local matrix accounting for the force vector acting on *ip* |
| $\mathbb{M}$ | Global stiffness matrix |
| $n$ | Number of nodes of the grid |
| $N_i$ | Element shape function associated to the $i^{th}$ vertex |
| $\mathbf{N}$ | Array containing the element shape functions |
| $\mathbf{N}_s$ | Special arrangement of the element shape functions |
| $\hat{\mathbf{n}}$ | Unitary vector normal to a surface |
| $\hat{\mathbf{n}}_s$ | Symmetric arrangement of the unitary vector normal to a surface |
| $p$ | Pore pressure |
| $\mathbf{Q}_{ip}$ | Local matrix accounting volumetric strain acting on *ip* |
| $q$ | Rate of fluid volume injected or removed per unit of volume |
| $R$ | Specific gas constant |
| $r_w$ | Well radius |
| $\mathbf{r}^f$ | Position vector of the fluid phase |
| $\mathbf{r}^s$ | Position vector of the solid phase |
| $\mathbf{r}^{f/s}$ | Position vector of the fluid phase relative to the solid phase |
| $\mathbf{s}_f$ | Area vector of face $f$ |
| $\mathbf{s}_s$ | Special arrangement of the area vector components |
| $T$ | Final time or temperature |

| | |
|---|---|
| $u$ | Component of the displacement vector in x direction |
| $\bar{u}$ | Prescribed pore pressure value |
| $\mathbf{u}$ | Displacement vector |
| $\bar{u}$ | Prescribed displacement vector |
| $v$ | Component of the displacement vector in y direction |
| $\mathbf{v}$ | Darcy velocity |
| $\tilde{\mathbf{v}}$ | Pseudo-velocity |
| $x$ | Coordinate x in the real domain |
| $y$ | Coordinate y in the real domain |
| $z$ | Coordinate z in the real domain |
| $w$ | Component of the displacement vector in z direction |
| $WI$ | Well index |

## Greek Letters

| | |
|---|---|
| $\alpha$ | Biot-Willis' coefficient |
| $\gamma$ | Coordinate $\gamma$ in transformed domain |
| $\Gamma$ | Surface boundary and diffusivity |
| $\boldsymbol{\epsilon}$ | Strain tensor |
| $\epsilon$ | Volumetric strain |
| $\eta$ | Coordinate $\eta$ in transformed domain |
| $\lambda$ | $1^{st}$ Lamè's parameter |
| $\tilde{\boldsymbol{\lambda}}$ | Pseudo-mobility tensor |
| $\boldsymbol{\lambda}$ | Mobility tensor |
| $\mu$ | Fluid viscosity |
| $\nu$ | Drained Poisson's ration |
| $\nu_u$ | Undrained Poisson's ration |
| $\xi$ | Coordinate $\xi$ in transformed domain |
| $\Pi$ | Well pressure |
| $\rho$ | Medium density |
| $\rho_f$ | Fluid phase density |
| $\rho_f$ | Fluid phase density |

| | |
|---|---|
| $\rho_s$ | Solid phase density |
| $\boldsymbol{\sigma}$ | Total stress tensor |
| $\boldsymbol{\sigma'}$ | Effective stress tensor |
| $\sigma$ | Total volumetric stress |
| $\phi$ | Porosity |
| $\Phi$ | General scalar quantity |
| $\boldsymbol{\Phi}^e$ | Vector containing the general scalar quantities associated to its vertices |
| $\Omega$ | Domain of calculus |
| $\dot{\omega}$ | Volumetric flux |

## Subscripts

| | |
|---|---|
| $0$ | Relative to initial state ($t = 0$) |
| $D$ | Dirichlet boundary condition |
| $e$ | evaluated at face $e$ |
| $E$ | Evaluated at node $E$ |
| $f$ | Fluid phase |
| $N$ | Neumann boundary condition |
| $ip$ | Evaluated at the integration point |
| $P$ | Evaluated at node $P$ |
| $s$ | Solid phase or sub-element |
| $\dot{s}$ | Evaluated at the centroid of the sub-element |
| $x, y, z$ | Derivative relative to global coordinates |
| $\xi, \eta, \gamma$ | Derivative relative to local coordinates |

## Superscripts

| | |
|---|---|
| $e$ | Relative to element $e$ |
| $p$ | Relative to pressure |
| $o$ | Used when the property is evaluated at the previous time step level |

| | |
|---|---|
| $T$ | Transpose |
| $\mathbf{u}$ | Relative to displacement vector |
| $x, y, z$ | Components $x$, $y$ and $z$ of a vector |

## Special Symbols

| | |
|---|---|
| $\nabla$ | Nabla operator |
| $\nabla_s$ | Symmetric nabla operator |
| $\nabla^2$ | Laplacian operator |
| $\partial_x$ | Partial derivative with respecto to x |
| $\Delta t$ | Time step size |
| $\Delta V_s$ | Volume of the sub-element |
| $\mathrm{d}\overline{V}$ | Differential volume in the transformed domain |
| $\Delta \overline{V}_s$ | Volume of the sub-element $s$ in the transformed domain |
| $\Delta\Omega_i$ | Volume of the control volume $i$ |
| $\mathrm{d}\Omega_i$ | Differential volume in the real domain |
| $\mathrm{d}\Gamma$ | Differential area |
| $L(\cdot)$ | General differential operator |
| $f(\mathbf{x})$ | General function |
| $r(\mathbf{x})$ | Residue function |
| $\mathrm{tr}(\cdot)$ | Trace of a tensor |
| $\tilde{u}(\mathbf{x})$ | Approximate solution |
| $\phi_j(\mathbf{x})$ | j$^{th}$ trial function |
| $w_j(\mathbf{x})$ | j$^{th}$ test function |
| $\mathscr{S}_p$ | Finite function space for pressure |
| $\mathscr{S}_u$ | Finite function space for displacements |
| $\mathscr{S}_p^h$ | Discrete finite function space for pressure |
| $\mathscr{S}_u^h$ | Discrete finite function space for displacements |
| $\mathscr{W}$ | Test space |
| $\mathscr{E}^i$ | Set of element sharing the same vertex $i$ |

# RESUMO

Esta tese apresenta uma formulação numérica unificada para a solução de problemas de poroelasticidade (geomecânica) acoplada. O Método dos Volumes Finitos baseado em Elementos é utilizado para a obtenção das equações discretizadas do modelo matemático. Além disso, a metodologia numérica é aplicada a malhas não estruturadas tridimensionais, compostas por diferentes tipos de elementos, a saber: tetraedros, hexaedros, prismas e pirâmides. A formulação numérica obtida, portanto, além apresentar alta flexibilidade geométrica para a discretização de geometrias complexas, também garante a conservação da massa e de quantidade de movimento localmente em cada volume de controle da malha computacional. A contribuição principal do presente trabalho, no entanto, reside em propor uma técnica de estabilização no âmbito dos volumes finitos. Em problemas de poroelasticidade existe uma condição crítica, denominada consolidação não drenada, que produz oscilações espúrias nos campos de pressão e deslocamento quando determinadas formulações numéricas são empregadas. Uma forma de se resolver este problema é a utilização de técnicas de estabilização. Existem inúmeras técnicas já desenvolvidas empregando o método dos elementos finitos, mas não foi encontrada na literatura nenhuma estratégia de estabilização no âmbito dos volumes finitos. A alternativa proposta nesta tese é utilizar o chamado *Physical Influence Scheme* (PIS) para aproximar o vetor velocidade da fase sólida presente na equação de conservação da massa para meios porosos deformáveis. Essa técnica foi originalmente desenvolvida para a solução de escoamentos incompressíveis governados pelas equações de Navier-Stokes. O presente trabalho identifica as semelhanças entre problemas de consolidação não drenada e escoamentos incompressíveis justificando, assim, o emprego do PIS também em problemas de poroelasticidade, o que caracteriza o aspecto inovador desta tese. Os resultados apresentados mostram que, de fato, a formulação numérica não estabilizada produz campos de pressão com a presença de oscilações espúrias, desprovidas de sentido físico. O uso do PIS, no entanto, é capaz de eliminar tais inconsistências, produzindo soluções suaves e livres de instabilidades. Para os casos de malhas compostas por elementos prismáticos e piramidais, notou-se que o cálculo do comprimento difusivo, utilizado no PIS, é uma etapa que pode ser aperfeiçoada em trabalhos futuros.

**Palavras-chave:** Geomecânica, Poroelasticidade, Volumes Finitos, Estabilização, Malhas Não Estruturadas

# RESUMO EXPANDIDO

## Introdução

A geomecânica é a área do conhecimento que estuda o comportamento mecânico de estruturas geológicas, como rochas e solos. Diferente da maioria dos materiais, que são constituídos por apenas uma fase, estruturas geológicas são compostas pela própria matriz sólida e por um fluido que preenche sua rede de poros e, portanto, duas fases podem ser identificadas: uma fase sólida e outra fase fluido (gasosa e/ou líquida). Na presença de uma solicitação mecânica, parte da carga externa aplicada à estrutura é suportada pela fase sólida e a outra parte pela fase fluido. Como consequência, as alterações do campo de pressão devido ao escoamento de fluido pela rede de poros representa um desequilíbrio de forças para a matriz porosa. Esta, por sua vez, tende a buscar uma nova configuração de equilíbrio e, ao se deformar, o próprio escoamento é afetado. O tratamento de problemas acoplados de escoamento/geomecânica é feito através da teoria da consolidação de Biot, composta pela equação de conservação da massa para meios porosos deformáveis e pela equação de equilíbrio de forças considerando também a influência das pressões de poro (princípio das tensões efetivas de Terzaghi). A solução numérica dessas equações ainda apresentam inúmeros desafios. Um deles está ligado à escolha dos métodos de discretização e às malhas computacionais empregadas. Apesar do que se verifica comumente na indústria, existe um esforço significativo da comunidade científica em utilizar a mesma metodologia numérica e mesma malha computacional para a solução de ambas as equações. Neste cenário, o método dos elementos finitos e suas vertentes tem papel predominante, apesar de alguns avanços recentes utilizando o método dos volumes finitos também serem observados. Nesta tese, será proposta uma formulação totalmente conservativa utilizando o método dos volumes finitos baseado em elementos. Além disso, serão utilizadas malhas não estruturadas tridimensionais compostas por diferentes tipos de elementos. Outra dificuldade enfrentada pelos métodos numéricos para a solução dessas equações é como tratar os modos espúrios que podem surgir no campo de pressão em determinadas situações. O método PIS (Physical Influence Scheme) é uma técnica utilizada para solucionar um problema muito similiar que surge ao se resolver as equações de Navier-Stokes. A partir dessa similaridade, essa tese propõe a aplicação do método PIS em problemas de geomecânica acoplada para eliminar os campos oscilatórios de pressão.

**Objetivos**

Este trabalho pretende apresentar uma formulação numérica unificada para a solução de problemas de poroelasticidade acoplada. O objetivo é resolver tanto o modelo de escoamento quanto o modelo geomecânico utilizando o Método dos Volumes Finitos baseado em Elementos (*Element based Finite Volume Method* – EbFVM). Além de garantir a conservação da massa e de quantidade de movimento em cada volume de controle, o EbFVM é naturalmente aplicável a malhas não estruturadas. Neste trabalho serão empregadas malhas não estruturadas tridimensionais compostas por elementos tetraédricos, hexaédricos, piramidais e prismáticos.

O principal objetivo, no entanto, é propor uma técnica de estabilização no âmbito do método dos volumes finitos para a solução de problemas de poroelasticidade. A proposta desta tese é utilizar o método *Physical Influence Scheme* (PIS) para calcular o vetor velocidade da fase sólida presente na equação de conservação da massa. Esta técnica foi originalmente proposta para a solução das equações de Navier-Stokes para escoamentos incompressíveis, e sua aplicação em problemas de poroelasticidade caracteriza o aspecto inédito desta tese.

**Metodologia**

A implementação computacional da metodologia numérica foi realizada utilizando a linguagem C++. Foi utilizada também uma biblioteca desenvolvida no laboratório SINMEC, chamada EFVLib, que oferece suporte numérico e geométrico para a implementação do Método dos Volumes Finitos baseado em Elementos. A biblioteca PETSc foi empregada para a solução dos sistemas lineares. As malhas computacionais foram geradas utilizando tanto um código próprio, escrito em Python, quanto o software ICEM CFD 15.0. A biblioteca Matplotlib foi utilizada para a geração de todos os gráficos apresentados e a visualização de resultados e geração de imagens foi realizada no software Kraken 2.1.6.

**Resultados e Discussão**

Foram implementadas duas formulações numéricas: uma formulação tradicional e não estabilizada e outra formulação estabilizada utilizando o PIS. Os resultados foram planejados para avaliar diferentes aspectos

dessas formulações. Primeiramente, foram resolvidos problemas clássicos de poroelasticidade, que possuem solução analítica, além de alguns problemas que ilustram aplicações reais na engenharia. Esses problemas permitiram avaliar a correta implementação e a consistência de ambas as formulações estabilizada e não estabilizada. Em seguida, foram realizados testes de convergência para avaliar a ordem de aproximação das variáveis pressão e deslocamento. Como esperado, as formulações apresentadas possuem segunda ordem de aproximação para ambas as variáveis, independente do tipo de elementos empregado. Tal informação indica que instabilidades numéricas devem surgir em situações de consolidação não drenada. Desse modo, a última bateria de resultados foi planejada com o intuito de avaliar o desempenho de ambas as formulações durante a consolidação não drenada. Em todos os casos esta condição foi obtida utilizando-se um passo de tempo suficientemente pequeno. Os resultados mostram que a técnica de estabilização pelo PIS é eficaz na eliminação das instabilidades numéricas na maior parte dos casos. Para malhas compostas por elementos prismáticos e piramidais, que são elementos de transição apenas, o cálculo adequado do comprimento difusivo provavelmente irá produzir melhores resultados. Além disso, foram resolvidos problemas com forte acoplamento entre as equações, onde foram capturados efeitos como o de Mandel-Cryer e o efeito de Noordbergum.

**Considerações Finais**

Nesta tese foram resolvidos problemas de poroelasticidade tridimensionais utilizando malhas não estruturadas híbridas. O Método dos Volumes Finitos baseado em Elementos foi utilizado para a discretização das equações diferenciais parciais. Uma formulação estabilizada foi obtida empregando-se o chamdado *Physical Influence Scheme*, que se mostrou como uma alternativa viável e inovadora. O sucesso da aplicada desta técnica indica um novo caminho para a solução de problemas de poroelasticidade acoplada, permitindo a aplicação de técnicas originalmente desenvolvidas para a solução de problemas de escoamentos incompressíveis na área de mecânica dos fluidos.

**Palavras-chave:** Geomecânica, Poroelasticidade, Volumes Finitos, Estabilização, Malhas Não Estruturadas

# ABSTRACT

This thesis presents an unified numerical formulation for solving coupled poroelasticity (geomechanics) problems. The Element based Finite Volume Method is employed for obtaining the algebraic representation of the model equations. Additionally, the numerical methodology is applied to three-dimensional unstructured grids composed of different types of elements, namely: tetrahedra, hexahedra, prisms and pyramids. The resulting numerical scheme, therefore, besides ensuring mass and momentum conservation for each control volume of the grid, it also presents great geometrical flexibility for discretizing complex geometries. The main contribution of the present work, however, is to propose a stabilization technique in the finite volume framework. In poromechanics there is a critical situation, known as undrained consolidation, that causes spurious oscillations to be observed in the pressure and displacement fields when some numerical schemes are employed. An alternative to circumvent this problem is to employ a stabilization technique. There are quite a few stabilization techniques using the finite element method, but none has been found in the literature that employs a finite volume formulation. The strategy proposed in this thesis is to use the Physical Influence Scheme (PIS) for approximating the velocity vector of the solid phase that appears in the mass conservation equation for deformable porous media. This technique was originally developed for solving incompressible fluid flows governed by the Navier-Stokes equations. The present work identifies some similarities between incompressible fluid flows and undrained consolidation in order to back up the application of PIS in poroelasticity as well. This particular point has been found to be a novelty and characterizes the inovative aspect of this thesis. The results show that, indeed, the non-stabilized formulation provides pressure fields with spurious oscillations devoid of physical meanings. The use of PIS, however, is capable of mitigating such inconsistencies and produces stable and smooth solutions. In cases where grids composed of pyramids or prisms are employed, it is observed that further improvements should be undertaken for computing the diffusive length in order for the PIS to be fully effective.

**Keywords:** Geomechanics, Poroelasticity, Finite Volume, Stabilization, Unstructured Grids

CHAPTER

# 1

# INTRODUCTION

This thesis mainly deals with the numerical aspects of coupled poroelasticity, where geomechanics is included. Although poroelasticity and geomechanics present a variety of applications, they are placed here in the context of oil and gas exploitation, since this work has been partially funded by ANP (Agência Nacional do Petróleo, Gás Natural e Biocombustíveis) through the PRH-ANP/MCT (Programa de Recursos Humanos da ANP para o setor de Petróleo e Gás). Thereby, the presentation begins by highlighting the role of reservoir simulations in oil and gas industry and then common practices and recent advances for incorporating geomechanical effects into these simulators are presented. In the sequence, an important discussion is provided about stability issues related to the numerical solution of poroelasticity problems. Finally, the main goals and contributions of this work are established and the outline of this thesis is presented.

## 1.1 Oil and gas exploitation

Petroleum is a natural resource that has been widely exploited since the second half of 18th century, when it has become known as “black gold” due to the wide variety of byproducts that could be obtained from it (fuels, plastics, ink, cosmetics, asphalt, tires, and so on). After the advent of internal combustion engines, petroleum has established itself as one of the most important energy resources, detaining nowadays the largest share of the world's energy resources.

The complete process of oil and gas exploitation is a complex activity that involves significant amounts of financial resources. From prospection and well drilling stages to oil and gas exploitation, geologist and engineers have to deal with several technological challenges in order to ensure not just the success but also the efficiency of the process. Particularly during the exploitation stage, after the reservoir viability is confirmed, engineers use reservoir simulators for assessing different scenarios and deciding for the best production strategy. The need for increasingly accurate and reliable predictions of hydrocarbon production leads to a constant development and improvement of reservoir simulators.

Basically, two branches of development in reservoir simulators can be identified. The first branch relates to the numerical techniques employed to solve partial differential equations. In general, these equations are considerably complex and must be solved in irregular domains, hence looking for approximate solutions is the only alternative left. The first step for performing this task is to obtain the correspondent algebraic equations that somehow represent the discrete form of the original partial differential equations (continuous form). At this point, several discretization methods can be chosen (finite volume, finite element, finite difference, etc) for obtaining such algebraic equations, and each of them has its own particular characteristics. One of the major issues of this choice has to do with the computational grid. As will be discussed in Chapter 3, the discretization method is intimately related to the computational grid, and the quality and flexibility of this grid significantly affects accuracy and applicability to complex geometries. Once the set of algebraic equations is obtained, the second step is to solve the resulting system of equations. In real applications, linear systems with millions of unknowns are common to find, which leads to the development of *ad-hoc* preconditioners and parallel computing in order to reduce computational time.

The second branch refers to the development of mathematical models for a wide variety of physical phenomena involved in oil and gas exploitation. In some situations, single phase flow models are sufficient for predicting oil production. Secondary recovery by water injection is another common situation in which at least an imiscible two phase flow model for slightly compressible fluids is required. If $CO_2$ is to be injected instead of water, then not just the compressibility of the gas phase has to be modeled but possibly the exchange of mass between oil and gas phases should be also considered. When oil, water and gas phases are simultaneously present, the black oil model is often the most suitable choice. Compositional models are also available for simulating multiphase flows with arbitrary number of components and phases with exchange of mass between phases. Some Enhanced Oil Recovery (EOR) techniques involve also chemical reactions, *in-situ* oil combustion and even microbial activity (Microbial EOR - MEOR). In addition to flow models, there are also fracture models (propagation, activation, etc), heat transfer models, well models and many others. Most of these processes are also coupled to one another increasing even more their complexity. These complex physical phenomena are very challenging to be mathematically modeled and implemented into reservoir simulators and they are a matter of concern of a number of researchers and software developers around the world.

Among the numerous physical phenomena present in oil and gas exploitation, the geomechanical effects is increasingly gaining attention from the scientific community due to its large impact on productivity predictions and even on reservoir integrity. Geomechanics is a research field that studies the mechanical behavior of geological formations subjected to a force imbalance. The fluid flow developed inside the pore channels of reservoirs causes variations in the internal pressure field (pore pressure) which in turn induce the mechanical response of the porous matrix. In other words, the reservoir structure deforms as the fluid flow takes place and the consequences of this mechanism are countless. Some of the consequences caused by the induced stress fields are: wellbore damage; fault activation and oil leakage; induced seismicity; subsidence, which can create flooding areas and threaten civil buildings; loss of production due to rock compaction and pore space clogging; and many others. In any case, it is easy to conclude that the geomechanical response to oil and gas production is a physical phenomenon to be taken under strict control.

## 1.2 Reservoir simulators and geomechanics

Traditionally, reservoir simulators have always focused on solving multiphase flows in porous media as it is indeed the prevailing phenomenon occurring inside reservoirs. As widely accepted in scientific community, ensuring mass conservation in a discrete level is of utmost importance for an accurate solution of any type of fluid flow problem. This is precisely the basic premise of the Finite Volume Method (FVM), which justifies its generalized usage in most commercial and academic codes for solving fluid flows in porous media. In parallel, corner-point grids have gained ground due to its low computational cost, easiness of generation and reasonable flexibility when compared to Cartesian grids. As a consequence, the Finite Volume Method applied to corner-point grids is the most common landscape when it comes to reservoir simulation. By contrast, the Finite Element Method (FEM) has always been the natural choice for solving solid mechanics (geomechanics included), and it is naturally applied to unstructured grids, which allows for the discretization of complex geometries and local refinements. Therefore, when geomechanical problems are to be addressed, the most common approach is to solve the structural part by FEM with unstructured grids, and FVM applied to corner-point grids for solving the fluid flow in deformable porous media. These two types of grids are schematically represented in Figures 1.1a and 1.1b.

Despite being the standard procedure for solving geomechanics in oil and gas companies, treating two naturally coupled problems (fluid flow and geomechanics), defined in the same domain, in a separate manner poses a series of drawbacks that deserves further attention. Treating both problems in a separate manner means that both problems are solved in different grids with different numerical schemes: the mass conservation is solved by FVM for obtaining the pressure field in the corner-point grid (Figure 1.1a), and the displacement field is computed in the

**Figure 1.1** – (a) Corner-point grid, (b) unstructured grid and (c) overlapping grids.

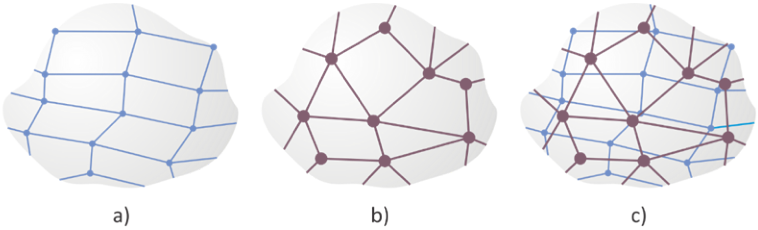

Source: Courtesy of Taisa Beatriz Pacheco Grein.

unstructured grid (Figure 1.1b) by solving the equilibrium equations with FEM. As a coupled problem, the mass conservation equation requires the displacement field, which is defined in another grid, in order to be solved. Conversely, the pressure field, defined in the corner-point grid, is needed for solving the stress equilibrium equations in the unstructured grid. This situation requires data interpolations between the two overlapping grids (Figure 1.1c) and it represents an extra source of numerical errors in the approximated solution. Furthermore, if an in-house code is to be developed, implementing two different numerical methodologies can be cumbersome. Otherwise, if two separate commercial software are to be used, at least data exchange and time synchrony have to be carefully managed, and it can be a painful task to be performed as well.

In this context, several researchers have been proposing unified methodologies that use a single grid to tackle coupled geomechanics. For instance, Gutierrez *et al.* (2001) employed the FEM for discretizing both multiphase flow and geomechanical models. Later on, White & Borja (2008) used a finite element fomulation for solving single phase and geomechanics, but they also adressed some stability issues. A mass conservative mixed finite element (Mixed FEM) formulation has been proposed for single phase flows in deformed porous media by Ferronato *et al.* (2010). Yang *et al.* (2013) applied another Mixed FEM for solving multiphase flows coupled to geomechanics. More recently, Choo & Borja (2015) presented a stabilized Mixed FEM for solving geomechanics in porous media with double porosity. This list of works is not exhaustive by any means but it illustrates the efforts made by the finite element community in solving coupled geomechanics in a unified manner.

Alternatively, a few important attempts for solving coupled geomechanics by using the FVM have also been presented in recent years. Recognizing the predominance of FVM in commercial reservoir simulators, Shaw & Stone (2005) considered the solution of linear elasticity equations also by a finite volume approach. In their pioneer work, Shaw & Stone (2005) employed three-dimensional unstructured cell-centered grids, although emphazis has been placed on corner-point grids. Later on, dal Pizzol (2013a); dal Pizzol & Maliska (2012) presented a finite volume formulation of coupled geomechanics in Cartesian staggered grids for two-dimensional problems. Important advances on cell-centered finite volume formulations were also developed by Nordbotten (2014, 2015, 2016) and Both *et al.* (2017) for two-dimensional unstructured grids. More recently, Ribeiro (2016) presented an Element-based Finite Volume formulation for coupled geomechanics using two-dimensional unstructured grids. In his work, Ribeiro (2016) compared the solution of the geomechanical model by using the EbFVM and FEM and concluded that both formulations provide virtually the same results. From these few advances in coupled geomechanics with finite volumes, only the work of Nordbotten (2016) tackled the problem of stability, where he provides evidences of a stable discretization "with respect to the limits of incompressible fluids and small time-steps". A discussion on numerical stability on geomechanics is addressed in the sequence.

## 1.3 Stability issues on geomechanics

Single-phase fluid flows in porous media coupled with geomechanics is mathematically modeled by a system of coupled partial differential equations that are usually solved by numerical techniques. The numerical solution of these equations poses a series of obstacles that deserve careful attention. A well known difficulty when solving coupled geomechanical problems has to do with the numerical instabilities that can appear under certain circunstances, as first reported by Vermeer & Verruijt (1981) almost 40 years ago. In his work, Vermeer & Verruijt (1981) studied the uncoupled one-dimensional consolidation problem and showed that there is a lower time step size limit under which unstable solutions might be obtained with standard finite element formulations. According to Vermeer & Verruijt (1981), stable solutions are obtained if the following relation is satisfied:

$$\Delta t \geqslant \frac{1}{6}\frac{h^2}{c} \tag{1.1}$$

where $h$ is the size of the grid element (considering an equally-spaced grid) and $c$ is the consolidation coefficient, that considers the material permeability, compressibilities and poromechanical properties (see Equation A.3 in Appendix A). The term $h^2/6c$ is the lowest time step size that produces a stable solution. In numerical methods, solution accuracy is usually increased by reducing the time step size, so having a lower limit for the time step size is a quite counterintuitive statement. In fact, unstable solutions may be obtained close to loaded drained boundaries or at the interface between different materials if the minimum time step criterion is not satisfied. In their own words, Vermeer & Verruijt (1981) says: "A physical explanation of the lower limit of the time steps may be that in the very beginning consolidation is merely a surface phenomenon, with a singularity in the derivative of the excess pore pressures at the draining surface or at the interface between strata of different permeability, and it is not feasible to approximate that by a series of straight line segments. Only after consolidation has progressed deep enough into the medium to affect the pore stresses in the first row of nodes in the interior of the medium, can a reasonable approximation by straight line segments be expected.Roughly speaking, the first time step should be of the order of magnitude of the consolidation time of the elements near the draining boundary".

Although the one-dimensional analysis performed by Vermeer & Verruijt (1981) has its value, the actual reason for obtaining unstable solutions happens to be related to the choice of interpolation pairs for pressure and displacements. Babuška (1971) and Brezzi (1974) developed the underlying theory that poses a limitation on the choice of the interpolation pairs in order to obtain stable solutions for incompressible elasticity and incompressible fluid flows. Also known as the Ladyžhenskaya-Babuška-Brezzi (LBB) condition (Guzmán *et al.*, 2013), this theory provides necessary and sufficient conditions for the well-posedness of saddle point problems, such as those arising from incompressible solid and fluid mechanics. Zienckiewicz *et al.* (1990) pointed out that this is precisely the mechanism behind soil mechanics as it also becomes a saddle point problem in limiting cases (undrained consolidation). A few years later, Murad & Loula (1992, 1994) provided error estimates on finite element approximations and showed that the instabilities generated in the beginning of the consolidation exponentially decay in time, which is indeed observed in numerical experiments.

Based on the discussion above, several strategies have been proposed for obtaining robust numerical formulations for solving coupled geomechanics. Apart from performing local refinements in order to satisfy the minimum time step criteria of Vermeer & Verruijt (1981), the strategies developed by researchers for avoiding numerical instabilities range from stabilization techniques to mixed finite element formulations. Some of these strategies are briefly discussed later on Chapter 5. It is important to notice that all of these strategies were developed in the context of finite element methods, since geomechanics is a fairly unexplored field for the finite volume community.

## 1.4 Work purposes and contributions

This work proposes the solution of fluid flows in deformable porous media coupled with linear geomechanics by using a unified formulation. In this case, the Element-based Finite Volume Method (EbFVM) has been chosen for solving the flow and geomechanical models for two main reasons. First of all, as a finite volume method the EbFVM ensures mass conservation in discrete levels, which is an important feature for fluid flow problems. It also ensures momentum conservation, which is in fact a combination of Newton's laws. In addition, the EbFVM naturally handles hybrid unstructured grids, composed of tetrahedra and hexahedra with prisms and pyramids for performing transitions between elements. These types of grids provide great flexibility for discretizing specific regions of the domain. One good example is the possibility of building radial grids in the near-well region, as illustrated in Figure 1.2, for better capturing the radial flow pattern in this region. It is out of the scope of this thesis, however, to explore all potentials of unstructured grids to reservoir simulators, although an unstructured grid with a radial portion in the near-well region is employed in one of the examples shown in the results chapter.

**Figure 1.2** – Unstructured grid in the near-well region.

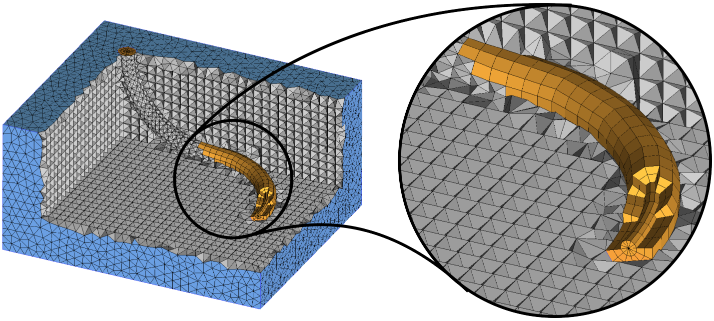

Source: Own authorship.

The main goal in this thesis, however, is to obtain a stable formulation that produces smooth solutions under critical situations. The idea is to employ the so-called Physical Influence Scheme (PIS) for computing the solid velocities for the mass conservation equation [1]. This technique has been successfully applied for solving incompressible (Alisadeghi & Karimian, 2011; Karimian & Schneider, 1994; Schneider & Raw, 1987) and compressible (Karimian & Schneider, 1995; Schneider & Karimian, 1994) fluid flows governed by the Navier-Stokes equations, and its applicability in geomechanics has been found to be a novelty in the literature.

### 1.4.1 Specific goals

The specific goals of this work are:

- Use three-dimensional unstructured grids composed of different types of elements;
- Identify the similarities between pressure-velocity coupling in general fluid flows and pressure-displacement coupling in geomechanics;
- Use PIS for obtaining a consistent interpolation function for the displacement in 1D and 3D cases;
- Obtain a stable formulation for tetrahedral, hexahedral, prismatic and pyramidal elements;
- Verify the numerical model against analytical solutions;
- Check the orders of approximation of pressure and displacement thorough a convergence test;
- Assess the efficiency of PIS at preventing the solution from numerical instabilities;
- Test the proposed formulation in tightly coupled consolidation problems.

---

[1] The Physical Influence Scheme is actually employed for evaluating displacements, which are then used for computing solid velocities.

## 1.5 Outline of the thesis

This thesis is organized as follows.

Chapter 2 present a brief discussion on poroelasticity theory, in which geomechanics is included to. A detailed description of the geomechanical model (equilibrium equations) is also carried out. The Darcy velocity and solid velocity are defined and the fluid flow model for deformable porous media is finally derived. A discussion on initial and boundary conditions for poroelasticity problems close this chapter.

Chapter 3 discusses the various geometrical entities related to unstructured grids. It introduces the concepts of primal and dual grids and gives special attention to the dual entities that appear in the EbFVM. This chapter also present some important numerical aspects of unstructured grids that will be used along this thesis.

In chapter 4 the Element-based Finite Volume Method is presented by means of the Weighted Residuals Method and the model equations are fully discretized. Some notes on the resulting linear system are also provided.

In chapter 5 the main contributions of this work are found. It provides a brief review on stabilization techniques developed for geomechanics in the framework of the Finite Element Method. The similarities between coupled poroelasticity and fluid mechanics are identified, which is the main argument for using the Physical Influence Scheme in geomechanics. Finally, the interpolation function is obtained for the displacements and the diffusive lengths are defined for each type of element.

In chapter 6, a series of numerical tests are designed to test specific aspects of the proposed formulation. First, the consistency and correct implementation of the stabilized and non-stabilized formulations are verified against analytical solutions. A couple of real case problems are also presented. After a convergence test is performed, numerical tests are run in order to verify the efficiency of PIS at removing pressure wiggles.

Chapter 7 closes this work with the final conclusions. Suggestions for future investigations on this field are also provided in this chapter.

CHAPTER

# 2

# MATHEMATICAL MODEL

In this chapter, the mathematical model for describing single-phase flows in porous media coupled with geomechanics is presented. Geomechanics is the area of knowledge that studies the mechanical behavior of geological formations subjected to a force imbalance. Geological formations refer to a wide variety of soils and rocks found in nature. In most cases, the internal structure of these formations present a certain amount of fluid-filled pores, which are often connected to each other forming channels that allow the fluid to flow. When the fluid moves through the pore channels it causes the pore pressure field to be modified, which represents an internal force imbalance for the porous matrix (geological formation). As a response, the porous matrix deforms, which in turn modifies the pore channels. By modifying the pore channels, the fluid flow is also affected. In other words, the fluid flow depends on the mechanical response of solid matrix, and vice versa. Therefore, there is an evident coupling between the fluid flow and geomechanics. In fact, geomechanical problems cannot be addressed without a fluid flow model for deformable porous media. These types of problems are treated in a broader context by the theory of poroelasticity, which is discussed in the next section. In what follows, the mathematical models for both geomechanics and fluid flows in compacting media are presented.

## 2.1 Theory of poroelasticity: a brief review

The mechanical behavior of poroelastic materials subjected to external loads and internal pressure variations is treated, in the most general cases, by the theory of poroelasticity. Evidently, geological formations with elastic behavior fall within the phenomena described by the poroelastic theory. Some of the phenomena described by this theory are the subsidence caused by groundwater drawdown, which is the case of Venice for example (Comerlati *et al.*, 2004), surface uplifting due to underground $CO_2$ storage (Teatini *et al.*, 2011) as well as fault reactivation (Pereira *et al.*, 2014), among others. However, despite its main applicability points towards geomechanics, other areas are also contemplated by the theory of poroelasticity. For instance, in the field of bioengineering Roose *et al.* (2003) were successful in predicting the stress levels developed in brain structures due to tumor growth; and Swan *et al.* (2003) studied the mechanical behavior of bone structures subjected to external loads using the poroelastic theory.

Despite being a broader topic, the initial developments of the poroelastic theory have been pushed by researchers working on the field geomechanics, particularly on soil consolidation. Terzaghi (1923) has published the first work on this topic where he presented the concept of effective stresses by studying the one-dimensional consolidation of a soil column undergoing a compressive load. This concept states that an external load (total stress) applied to a porous medium is partially sustained by the solid matrix (effective stress) and partially by the fluid occupying the pore spaces (pore pressure). Almost two decades later, Biot (1941) presented a three-dimensional formulation for consolidation problems based on the theory already developed by Terzaghi. This theory is most known as Biot's theory of consolidation, and it was also extended to anisotropic and non-linear materials (Biot, 1955, 1956a). Rice & Cleary (1976) introduced the concept of drained and undrained conditions and Detournay & Cheng (1993) discussed the separate treatment of the fluid and solid phases by using a micromechanical approach. More recently, Lewis & Schrefler (1999) presented a complete work on theoretical, practical and numerical aspects of geomechanical problems, and Coussy (2004, 2010) definitely formalized the classical poroelastic theory in a unified thermodynamic framework.

## 2.2 Geomechanical model

The dynamic behavior of saturated porous media is described by the momentum equations, as presented by Biot (1956b). However, by considering that the porous matrix is only subjected to quasi-static loads, the dynamic terms vanish and these equations reduce to the stress equilibrium equations:

$$\nabla \cdot \boldsymbol{\sigma} + \rho \mathbf{g} = 0 \tag{2.1}$$

where $\nabla$ is the nabla operator, $\boldsymbol{\sigma}$ denotes the second-order symmetric total stress tensor, $\rho$ is the medium density and $\mathbf{g}$ is the gravity vector. In Cartesian coordinates, these tensor quantities can be represented as:

$$\nabla = \begin{bmatrix} \partial_x \\ \partial_y \\ \partial_z \end{bmatrix}, \quad \boldsymbol{\sigma} = \begin{bmatrix} \sigma_{xx} & \sigma_{xy} & \sigma_{xz} \\ \sigma_{xy} & \sigma_{yy} & \sigma_{yz} \\ \sigma_{xz} & \sigma_{yz} & \sigma_{zz} \end{bmatrix} \quad \text{and} \quad \mathbf{g} = \begin{bmatrix} g_x \\ g_y \\ g_z \end{bmatrix}. \tag{2.2}$$

where $\partial_x$ is a short for $\partial/\partial x$. As a consequence, the three equilibrium equations in Cartesian coordinates read:

$$\begin{gathered} \frac{\partial \sigma_{xx}}{\partial x} + \frac{\partial \sigma_{xy}}{\partial y} + \frac{\partial \sigma_{xz}}{\partial z} + \rho g_x = 0 \\ \frac{\partial \sigma_{xy}}{\partial x} + \frac{\partial \sigma_{yy}}{\partial y} + \frac{\partial \sigma_{yz}}{\partial z} + \rho g_y = 0. \\ \frac{\partial \sigma_{xz}}{\partial x} + \frac{\partial \sigma_{yz}}{\partial y} + \frac{\partial \sigma_{zz}}{\partial z} + \rho g_z = 0 \end{gathered} \tag{2.3}$$

The solution of Equations 2.1 provides the stress equilibrium state of any continuum material under the assumption of quasi-static load, including fluid statics. In geomechanical problems, in particular, the continuous medium is composed of a solid phase (porous matrix) and a fluid phase filling the pore channels. Therefore, the density in Equation 2.1 represent, in fact, a porosity weighted average of the solid phase density, $\rho_s$, and the fluid phase density, $\rho_f$, that is,

$$\rho = \phi \rho_f + (1 - \phi) \rho_s \tag{2.4}$$

with $\phi$ being the porosity defined by the ratio between the pore volume and a fixed bulk volume.

### 2.2.1 Terzaghi's effective stress and Biot's constant

According to Terzaghi (1923), the effective stress $\boldsymbol{\sigma}'$ is defined as the stress field developed in the porous matrix, i.e. in the solid structure. The effective stress is an internal stress field that must balance the external loads acting on the porous matrix. The external load is composed of two contributions: the total stress, $\boldsymbol{\sigma}$, and the normal stresses caused by the pore pressure, $p$, represented by a spherical tensor. In this work, positive sign is conventioned to represent traction. Furthermore, by considering the porous matrix to present a certain compressibility, as discussed by Biot (1941), the effective stress is given by:

$$\boldsymbol{\sigma}' = \boldsymbol{\sigma} + \alpha p \mathbf{I}. \tag{2.5}$$

In Equation 2.5, $\mathbf{I}$ is the second-order identity tensor and $\alpha$ is the Biot's coefficient (Biot & Willis, 1957), which is also known as the Biot-Willis' coefficient. The Biot's coefficient relates the solid compressibility, $c_s$, and the bulk compressibility, $c_b$, in the following manner,

$$\alpha = 1 - \frac{c_s}{c_b}. \tag{2.6}$$

The bulk compressibility represents the total compressibility of the porous matrix, which is composed of the compressibility of the solid grains, $c_s$, and the compressibility due to the solid grains rearrangement. Under an external load, the volume of the pore channels can change due to a rearrangement of the solid grains. For instance, if the solid grains are considered to be incompressible ($c_s = 0$), the porous matrix still presents some compressibility due to the variations in the pore channels' volume. In this manner, $c_b$ is always greater than $c_s$, thus $\alpha$ is always less or equal to one, but never zero. In fact, as discussed in Berryman (1992), the minimum value of $\alpha$ is precisely the porosity $\phi$. The conclusion that follows from this discussion and from Equations 2.5 and 2.6 is that the bigger the solid compressibility $c_s$, the smaller the impact of the pore pressure field in the effective stress $\boldsymbol{\sigma}'$, since $\alpha$ tends to its minimum value $\phi$. Conversely, as considered by Terzaghi (1923), if the solid compressibility is negligible ($c_s = 0$), the pore pressure has its major contribution to the effective stress tensor.

Finally, the stress equilibrium equations for deformable porous media is obtained by substituting Equation 2.5 into Equation 2.1, yielding

$$\nabla \cdot (\boldsymbol{\sigma}' - \alpha p \mathbf{I}) + \rho \mathbf{g} = 0. \tag{2.7}$$

By expanding Equation 2.7 in Cartesian coordinates, the three stress equilibrium equations read

$$\begin{aligned}
\frac{\partial \sigma'_{xx}}{\partial x} + \frac{\partial \sigma'_{xy}}{\partial y} + \frac{\partial \sigma'_{xz}}{\partial z} + \rho g_x &= \alpha \frac{\partial p}{\partial x} \\
\frac{\partial \sigma'_{xy}}{\partial x} + \frac{\partial \sigma'_{yy}}{\partial y} + \frac{\partial \sigma'_{yz}}{\partial z} + \rho g_y &= \alpha \frac{\partial p}{\partial y}. \\
\frac{\partial \sigma'_{xz}}{\partial x} + \frac{\partial \sigma'_{yz}}{\partial y} + \frac{\partial \sigma'_{zz}}{\partial z} + \rho g_z &= \alpha \frac{\partial p}{\partial z}
\end{aligned} \tag{2.8}$$

## 2.2.2 Voigt notation

Although the mathematical notation of Equation 2.7 is correct, it is often convenient to write the stress equilibrium equations by using the Voigt notation. In order to do so, we define the symmetric nabla operator, $\nabla_s$, and redefine the effective stress and identity tensors as follows:

$$\nabla_s = \begin{bmatrix} \partial_x & 0 & 0 \\ 0 & \partial_y & 0 \\ 0 & 0 & \partial_z \\ \partial_y & \partial_x & 0 \\ 0 & \partial_z & \partial_y \\ \partial_z & 0 & \partial_x \end{bmatrix}, \quad \boldsymbol{\sigma}' = \begin{bmatrix} \sigma'_{xx} \\ \sigma'_{yy} \\ \sigma'_{zz} \\ \sigma'_{xy} \\ \sigma'_{yz} \\ \sigma'_{xz} \end{bmatrix} \quad \text{and} \quad \mathbf{I} = \begin{bmatrix} 1 \\ 1 \\ 1 \\ 0 \\ 0 \\ 0 \end{bmatrix}, \tag{2.9}$$

It is also worth noticing that the use of the Voigt notation for representing the effective stress and identity tensors is only possible because they are symmetric tensors. By employing Equation 2.9, the stress equilibrium equations in Voigt notation take the following form:

$$\nabla_s \cdot (\boldsymbol{\sigma}' - \alpha p \mathbf{I}) + \rho \mathbf{g} = 0. \tag{2.10}$$

It should be also kept in mind that, although $\boldsymbol{\sigma}'$ and $\mathbf{I}$ appear in both Equations 2.7 and 2.10, they are written in terms of the Voigt notation in Equation 2.10. In fact, the symbols $\boldsymbol{\sigma}'$ and $\mathbf{I}$ hereafter denote the effective stress and the identity tensors in Voigt notation, except when indicated otherwise.

### 2.2.3 Strain-displacement relations

The strain state at a given point in a continuum body is described by a second-order symmetric tensor, that is,

$$\boldsymbol{\epsilon} = \begin{bmatrix} \epsilon_{xx} & \epsilon_{xy} & \epsilon_{xz} \\ \epsilon_{xy} & \epsilon_{yy} & \epsilon_{yz} \\ \epsilon_{xz} & \epsilon_{yz} & \epsilon_{zz} \end{bmatrix}. \tag{2.11}$$

On the other hand, the displacement of a point from an initial (undeformed) state to a deformed configuration is represented by the displacement vector,

$$\mathbf{u} = \begin{bmatrix} u \\ v \\ w \end{bmatrix}. \tag{2.12}$$

In this work, the hypothesis of small strains is assumed, so the strain tensor becomes linear. Under this assumption, the strain tensor can be completely described by the symmetric part of the displacement gradient tensor. That is,

$$\boldsymbol{\epsilon} = \frac{1}{2}\left(\nabla \mathbf{u} + \nabla \mathbf{u}^T\right) \tag{2.13}$$

The normal components of the linear strain tensor, according to Equations 2.13, are,

$$\epsilon_{xx} = \frac{\partial u}{\partial x}, \qquad \epsilon_{yy} = \frac{\partial v}{\partial y} \qquad \text{and} \qquad \epsilon_{zz} = \frac{\partial w}{\partial z}, \tag{2.14}$$

and the shear strains are give by,

$$\begin{aligned}\epsilon_{xy} &\equiv \frac{\gamma_{xy}}{2} = \frac{1}{2}\left(\frac{\partial v}{\partial x} + \frac{\partial u}{\partial y}\right)\\ \epsilon_{xz} &\equiv \frac{\gamma_{xz}}{2} = \frac{1}{2}\left(\frac{\partial w}{\partial x} + \frac{\partial u}{\partial z}\right).\\ \epsilon_{yz} &\equiv \frac{\gamma_{yz}}{2} = \frac{1}{2}\left(\frac{\partial v}{\partial z} + \frac{\partial w}{\partial y}\right),\end{aligned} \tag{2.15}$$

where $\gamma_{ij}$ represent the engineering shear strains.

It is also convenient to use the Voigt notation to represent the strain tensor in Equation 2.11 and to use the engineering shear strains $\gamma_{ij}$ instead of $\epsilon_{ij}$ when $i \neq j$. In this manner, the strain tensor is written as,

$$\boldsymbol{\epsilon} = \begin{bmatrix}\epsilon_{xx} & \epsilon_{yy} & \epsilon_{zz} & \gamma_{xy} & \gamma_{yz} & \gamma_{xz}\end{bmatrix}^T. \tag{2.16}$$

By the definition of the symmetric nabla operator (Equation 2.9) and the strain tensor represented in Voigt notation, Equation 2.13 can be recovered in a convenient manner by the following expression:

$$\boldsymbol{\epsilon} = \nabla_s \mathbf{u}. \tag{2.17}$$

### 2.2.4 Constitutive model

The constitutive model of a given material refers to the relationship between the stress and strain tensors. Evidently, different materials behave differently when subjected to a certain level of external load. Newtonian fluids, for instance, continuously deform when subjected to shear stresses. Conversely, the stress-strain relationship of non-Newtonian fluids depends on the level of stress (or strain) they are undergoing, which characterizes a non-linear behavior. Solid materials, in general, present a linear stress-strain relationship up to a certain level (the yield point), beyond which the material undergoes a plastic flow until its rupture.

In Equation 2.10, the effective stress tensor $\boldsymbol{\sigma}'$ refers to the the stress field established in the porous solid matrix, thus a constitutive model is required only for the porous matrix. The stress-strain relationship is represented by the following expression,

$$\boldsymbol{\sigma}' = \mathbb{C} : \boldsymbol{\epsilon} \tag{2.18}$$

where $\mathbb{C}$ represent a fourth-order constitutive tensor, with 81 independent constants that fully represent the constitutive relations of the material. Alternatively, by employing indicial notation and the Einstein summation convention, Equation 2.18 can be rewritten as:

$$\sigma'_{ij} = C_{ijkl}\epsilon_{kl}. \tag{2.19}$$

In addition, the symmetries of the stress ($\sigma_{ij} = \sigma_{ji}$) and strain ($\epsilon_{ij} = \epsilon_{ji}$) tensors imply that,

$$C_{ijkl} = C_{jikl} = C_{ijlk} = C_{klij}, \tag{2.20}$$

which reduces the number of independent constants from 81 to 36. As a result, the Voigt notation can again be employed to represent the constitutive tensor (hereafter referred to as constitutive matrix):

$$\mathbb{C} = \begin{bmatrix} C_{11} & C_{12} & C_{13} & C_{14} & C_{15} & C_{16} \\ C_{21} & C_{22} & C_{23} & C_{24} & C_{25} & C_{26} \\ C_{31} & C_{32} & C_{33} & C_{34} & C_{35} & C_{36} \\ C_{41} & C_{42} & C_{43} & C_{44} & C_{45} & C_{46} \\ C_{51} & C_{52} & C_{53} & C_{54} & C_{55} & C_{56} \\ C_{61} & C_{62} & C_{63} & C_{64} & C_{65} & C_{66} \end{bmatrix}. \tag{2.21}$$

Furthermore, by considering the generalized Hooke's law for isotropic materials, the number of independent constants is further decreased to only two. In this manner, the constitutive matrix takes the following form:

$$\mathbb{C} = \begin{bmatrix} 2G+\lambda & \lambda & \lambda & 0 & 0 & 0 \\ \lambda & 2G+\lambda & \lambda & 0 & 0 & 0 \\ \lambda & \lambda & 2G+\lambda & 0 & 0 & 0 \\ 0 & 0 & 0 & G & 0 & 0 \\ 0 & 0 & 0 & 0 & G & 0 \\ 0 & 0 & 0 & 0 & 0 & G \end{bmatrix}, \tag{2.22}$$

with $\lambda$ and $G$ being the $1^{st}$ and $2^{nd}$ Lamè's parameters, respectively. Parameter $G$ is also known as the shear modulus. The effective stress tensor can then be written as a matrix-vector product, that is:

$$\boldsymbol{\sigma}' = \mathbb{C}\boldsymbol{\epsilon}. \tag{2.23}$$

Moreover, by employing Equation 2.17, the stress tensor is conveniently written in terms of the displacement vector:

$$\boldsymbol{\sigma}' = \mathbb{C}\nabla_s \mathbf{u}. \tag{2.24}$$

### 2.2.5 Final form of the geomechanical model

Finally, the equilibrium equations are conveniently written in terms of the displacement vector by substituting Equation 2.24 into Equation 2.10, leading to:

$$\nabla_s \cdot (\mathbb{C}\nabla_s \mathbf{u} - \alpha p \mathbf{I}) + \rho \mathbf{g} = 0. \tag{2.25}$$

Although it is important to explicitly represent the divergent in Equation 2.25 by keeping the dot product "$\cdot$", it might also be of some help to point out that Equation 2.25 is equivalent to:

$$\nabla_s^T (\mathbb{C}\nabla_s \mathbf{u} - \alpha p \mathbf{I}) + \rho \mathbf{g} = 0. \tag{2.26}$$

Alternatively, by considering the constitutive matrix of Equation 2.22, the stress equilibrium equations can be explicitly written in terms of the Lamè's parameters, that is:

$$G\nabla^2 \mathbf{u} + (\lambda + G)\nabla(\nabla \cdot \mathbf{u}) + \rho \mathbf{g} = \alpha \nabla p \tag{2.27}$$

The stress equilibrium equations presented above represent the equilibrium of forces in the three coordinate directions acting on a infinitesimal volume. As already discussed before (see Equations 2.8), these equations actually split into three equations and the unknown functions are the displacement components $u_x$, $u_y$ and $u_z$ and the pore pressure $p$. So far we have three equations and four unknown functions, which requires an additional equation in order to have a closed problem. This additional equation is the mass conservation equation for deformable porous media, presented in the sequence.

## 2.3 Flow model

In this section the mathematical model for single phase flows in deformable porous media is presented. There are several paths for obtaining the mass conservation equation for deformable porous media. For the purposes of this work, it is interesting to follow the approach as presented by Verruijt (2016), where the mass conservation equations for the fluid phase and solid phase are combined to produce the global mass conservation equation for deformable porous media. This procedure is presented in the following subsections.

### 2.3.1 Velocity components

When dealing with fluid flows in deformable porous media, different velocities come into play so they should be well defined in order to avoid misunderstandings. With this purpose, Figure 2.1 shows a porous material with the indicated inertial coordinate system and a body-fixed coordinate system placed on the solid phase. The position of a particle on the fluid phase relative to the inertial reference frame is denoted by $\mathbf{r}^f$. In the same way, $\mathbf{r}^s$ denotes the position of a particle on the solid phase relative to the inertial reference frame. Finally, the position of a fluid phase point relative to the body-fixed reference frame placed on the solid phase is represented by $\mathbf{r}^{f/s}$. As depicted in Figure 2.1, these positions relate to each other by the following expression:

**Figure 2.1** – Velocity components for deformable porous media.

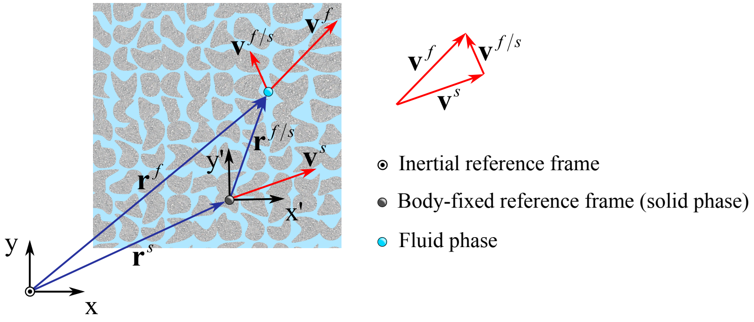

Source: Own authorship.

$$\mathbf{r}^f = \mathbf{r}^s + \mathbf{r}^{f/s}. \tag{2.28}$$

The time derivative of Equation (2.28) provides a relationship between the absolute velocities of the fluid ($\mathbf{v}^f$) and solid ($\mathbf{v}^s$) phases and the fluid velocity relative to the solid phase ($\mathbf{v}^{f/s}$):

$$\mathbf{v}^f = \mathbf{v}^s + \mathbf{v}^{f/s}. \tag{2.29}$$

The relative velocity $\mathbf{v}^{f/s}$ actually represents the velocity of the fluid moving through the pore channels of the porous matrix. It is interesting to notice that if the relative velocity $\mathbf{v}^{f/s}$ is zero, i.e. if there is no relative movement between solid and fluid phases, the absolute velocity of the fluid phase may still be different from zero if $\mathbf{v}^s \neq 0$. Conversely, if the solid phase (porous matrix) does not move at all, then

$$\mathbf{v}^s = \frac{\partial \mathbf{r}^s}{\partial t} = 0 \qquad \therefore \qquad \mathbf{v}^f = \mathbf{v}^{f/s}, \tag{2.30}$$

which is the starting point for obtaining the mathematical model for fluid flows in non-deformable porous media.

## 2.3.2 Average velocities

The velocity components presented in the previous subsection do not refer to the actual velocity profiles that develop inside the pore channels. Instead, the velocities $\mathbf{v}^f$, $\mathbf{v}^s$ and $\mathbf{v}^{f/s}$ actually represent an average value of the real velocity profiles $\left[\mathbf{v}^{f/s}\right]$, $[\mathbf{v}^s]$ and $\left[\mathbf{v}^f\right]$, respectively, at each pore channel of the porous matrix. When multiplied by porosity, these velocities represent the volume of material crossing an unit area per unit time, regarding that this unit area is sufficiently larger than the cross section area of the pore channels. A visual representation of these velocities is depicted in Figure 2.2.

Figure 2.2 illustrates a cross section area of a porous medium with the real velocity profiles inside the pore channels denoted by $\left[\mathbf{v}^{f/s}\right]$, $[\mathbf{v}^s]$ and $\left[\mathbf{v}^f\right]$. For obtaining these velocity profiles, the mass and momentum conservation equations have to be solved through the pore channels, which implies that the morphological structure of the flow path has to be known. This approach is impracticable for obvious reasons. The alternative is to consider average velocities in order to compute the mass fluxes over a cross section area. For instance, given a surface $S$ of area $\Delta S$, the total mass flux crossing this surface can be computed as:

**Figure 2.2** – Velocity profiles and average velocities.

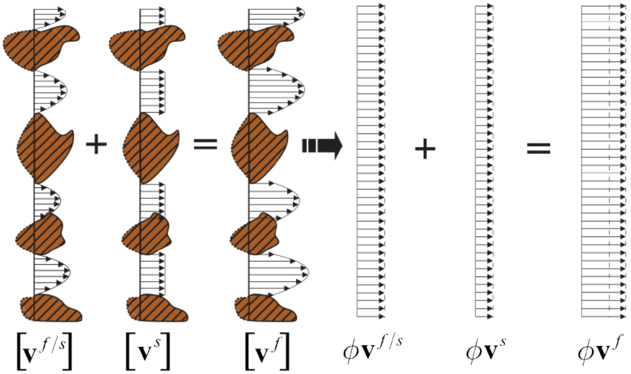

Source: Adapted from dal Pizzol (2013b).

$$\dot{m} = \int_S \rho_f \left[\mathbf{v}^f\right] \cdot \hat{\mathbf{n}}\, \mathrm{d}S = \rho_f \phi \mathbf{v}^f \cdot \hat{\mathbf{n}} \Delta S \tag{2.31}$$

where $\hat{\mathbf{n}}$ is a unit vector normal to the surface $S$ and $\rho_f$ is the density of the fluid phase. The important message of Equation 2.31 is that, instead of integrating the real velocity profile $\left[\mathbf{v}^f\right]$ along the surface $S$, one can simply use the average velocity $\mathbf{v}^f$ multiplied by the porosity in order to compute the mass flux $\dot{m}$.

## 2.3.3 Darcy's law and specific discharge

One of the main concepts to be considered when it comes to porous media is the macroscopic approach to the fluid flow through the pore channels. This is a convenient way to handle this phenomenon as it eliminates the necessity of knowing exactly the internal pore structures. Instead, from a macroscopic perspective, the only two parameters that really matter are the fluid viscosity and the absolute permeability of the porous medium. Based on these two parameters, the fluid flow takes place according to the pressure gradient and body forces (usually the gravitational field). Therefore, according to Darcy's law, the apparent velocity of the fluid subjected to a pressure gradient and the gravitational field is given by:

$$\mathbf{v} = -\frac{\mathbf{K}}{\mu} \cdot \left(\nabla p - \rho_f \mathbf{g}\right) \tag{2.32}$$

where $\mu$ is the fluid viscosity and $\mathbf{K}$ is a second-order tensor that represents the absolute permeability of the porous medium. As a symmetric tensor, in the most general case, the permeability tensor is composed of six different components. If the porous medium is orthotropic, then only the three diagonal components are non-zeros and different from each other. For isotropic materials, all the three diagonal components are the same, that is, $K_{ii} = k$ and $K_{ij} = 0$ for all $i \neq j$, so only one component is required.

In groundwater, the Darcy velocity, $\mathbf{v}$, in Equations 2.32 is also known as the specific discharge (seepage velocity and apparent velocity are also common nomenclatures). As it turns out, the specific discharge is precisely the porosity multiplied by the average velocity of the fluid phase relative to the solid phase, that is,

$$\mathbf{v} = \phi \left(\mathbf{v}^f - \mathbf{v}^s\right) = \phi \mathbf{v}^{f/s} \tag{2.33}$$

as first reported by Gersevanov (1934).

### 2.3.4 Fluid phase

By using the concepts of average velocities previously defined, the mass conservation equation for the fluid phase can be written in the following manner,

$$\frac{\partial}{\partial t}\left(\phi \rho_f\right) + \nabla \cdot \left(\rho_f \phi \mathbf{v}^f\right) = 0 \tag{2.34}$$

In this work, the fluid is assumed to be slightly compressible, so the product between the fluid phase velocity and the fluid density gradient can be disregarded. In addition, the chain rule is applied to the time derivative of Equation 2.34 and the definition of fluid compressibility is employed, that is,

$$\frac{1}{\rho_f}\frac{\partial \rho_f}{\partial t} = \frac{1}{\rho_f}\frac{\partial \rho_f}{\partial p}\frac{\partial p}{\partial t} = c_f \frac{\partial p}{\partial t} \tag{2.35}$$

which leads to,

$$\frac{\partial \phi}{\partial t} + \phi c_f \frac{\partial p}{\partial t} + \nabla \cdot \left( \phi \mathbf{v}^f \right) = 0. \tag{2.36}$$

It is interesting to notice that, as the solid phase moves, it also carries mass of fluid with it. This is the reason why the fluid velocity $\mathbf{v}^f$ is in Equation 2.36. If the solid phase is static, then $\mathbf{v}^f = \mathbf{v}^{f/s}$ and the Darcy velocity (Equations 2.32 and 2.33) can be readily substituted in Equation 2.36.

## 2.3.5 Solid phase

The mass conservation equation for a solid phase with density $\rho_s$ takes the following form:

$$\frac{\partial}{\partial t} \left[ (1 - \phi) \rho_s \right] + \nabla \cdot \left[ (1 - \phi) \rho_s \mathbf{v}^s \right] = 0. \tag{2.37}$$

in which the term $(1 - \phi)$ represent the volume fraction of the solid phase. For evaluating the time derivative of Equation 2.37, the following relationship, as shown in Appendix C, is useful:

$$\frac{\partial \rho_s}{\partial t} = -\frac{\rho_s c_s}{1 - \phi} \left( \frac{\partial \sigma_v}{\partial t} + \phi \frac{\partial p}{\partial t} \right), \tag{2.38}$$

where the volumetric stress is given by $\sigma_v = \operatorname{tr}(\boldsymbol{\sigma})/3$ and the solid compressibility is defined as:

$$c_s = \frac{1}{\rho_s} \frac{\partial \rho_s}{\partial p}. \tag{2.39}$$

Substituting Equation 2.38 into Equation 2.37 leads to

$$-\frac{\partial \phi}{\partial t} - c_s \frac{\partial \sigma_v}{\partial t} - c_s \phi \frac{\partial p}{\partial t} + \nabla \cdot \left[ (1 - \phi) \mathbf{v}^s \right] = 0. \tag{2.40}$$

A further manipulation is conveniently performed in Equation 2.40 by recognizing that,

$$\sigma_v = \sigma'_v - \alpha p = \frac{\epsilon_v}{c_b} - \alpha p \qquad \therefore \qquad \frac{\partial \sigma_v}{\partial t} = \frac{1}{c_b} \frac{\partial \epsilon_v}{\partial t} - \alpha \frac{\partial p}{\partial t}, \tag{2.41}$$

with $\epsilon_v$ denoting the volumetric strain, which is equal to the divergence of the displacement vector, that is, $\epsilon_v = \nabla \cdot \mathbf{u}$. In addition, it is useful to emphasize that the solid velocity is given by the time derivative of the displacement vector, such that,

$$\nabla \cdot \mathbf{v}^s = \nabla \cdot \frac{\partial \mathbf{u}}{\partial t} = \frac{\partial}{\partial t} (\nabla \cdot \mathbf{u}) = \frac{\partial \epsilon_v}{\partial t}. \tag{2.42}$$

Thus, by substituting Equations 2.41 and 2.42 into Equation 2.40 and using the definition of the Biot's coefficient (Equation 2.6), the mass conservation equation for the solid phase is finally obtained in a convenient form:

$$-\frac{\partial \phi}{\partial t} + \alpha \frac{\partial \epsilon_v}{\partial t} - c_s (\alpha + \phi) \frac{\partial p}{\partial t} - \nabla \cdot (\phi \mathbf{v}^s) = 0. \tag{2.43}$$

### 2.3.6 Global mass conservation

The final mass conservation equation for single phase flows in deformable porous media is obtained by adding Equations 2.36 and 2.43. The benefit from this procedure is that the time derivative of the porosity is eliminated, which yields to:

$$\frac{1}{M} \frac{\partial p}{\partial t} + \alpha \frac{\partial \epsilon_v}{\partial t} + \nabla \cdot \mathbf{v} = 0 \tag{2.44}$$

with $M$ being the Biot modulus (Biot & Willis, 1957), given by

$$M = \left[ \phi \, c_f + (\alpha - \phi) \, c_s \right]^{-1}, \tag{2.45}$$

and $\mathbf{v}$ denotes the specific discharge (or Darcy velocity), which relates to the fluid and solid phase velocities by Equation 2.33.

Equation 2.44 can be also written in terms of the solid velocity by using Equation 2.42. In addition, a source term can be added to the global mass conservation, that is,

$$\frac{1}{M} \frac{\partial p}{\partial t} + \nabla \cdot (\mathbf{v} + \alpha \mathbf{v}^s) = q \tag{2.46}$$

where $q$ is the rate of fluid volume injected or removed per unit of volume.

## 2.4 Initial and boundary conditions

For closuring the model equations, the initial and boundary conditions must be specified. The domain occupied by the porous medium can be denoted by $\Omega$ and its surface boundary by $\Gamma$. In addition, let $\hat{\mathbf{n}}$ be a unitary normal vector defined over the boundary $\Gamma$ and pointing outwards the domain $\Omega$. The surface boundary can be divided into regions subjected to Dirichlet boundary conditions, denoted by $\Gamma_D^p$ and $\Gamma_D^{\mathbf{u}}$ for $\mathbf{u}$ and $p$, respectively, and to Neumann boundary conditions, denoted by $\Gamma_N^p$ and $\Gamma_N^{\mathbf{u}}$, respectively. These sets are illustrated in Figure 2.3.

**Figure 2.3** – Domain $\Omega$, surface boundary $\Gamma$ and its subdivisions $\Gamma_N^p$, $\Gamma_D^p$, $\Gamma_N^{\mathbf{u}}$ and $\Gamma_D^{\mathbf{u}}$.

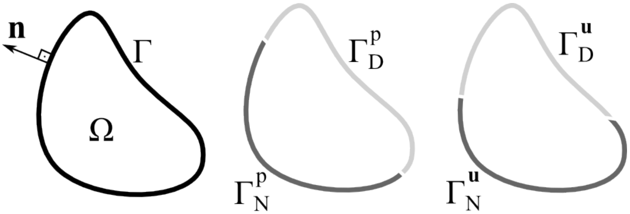

Source: Own authorship.

The problem can be stated as finding $p = p(\mathbf{r}, t)$ and $\mathbf{u} = \mathbf{u}(\mathbf{r}, t)$ such that:

$$\nabla_s^T (\mathbb{C}\nabla_s \mathbf{u} - \alpha p \mathbf{I}) + \rho \mathbf{g} = 0 \quad \text{on } \Omega \tag{2.47}$$

$$\frac{1}{M}\frac{\partial p}{\partial t} - \nabla \cdot \left[ \frac{\mathbf{K}}{\mu} \cdot \left( \nabla p - \rho_f \mathbf{g} \right) - \alpha \frac{\partial \mathbf{u}}{\partial t} \right] = q \quad \text{on } \Omega \tag{2.48}$$

$$(\boldsymbol{\sigma}' - \alpha p \mathbf{I}) \cdot \hat{\mathbf{n}} = \mathbf{t} \quad \text{on } \Gamma_N^{\mathbf{u}} \tag{2.49}$$

$$\mathbf{u} = \bar{\mathbf{u}} \quad \text{on } \Gamma_D^{\mathbf{u}} \tag{2.50}$$

$$-\mathbf{v} \cdot \hat{\mathbf{n}} = \dot{\omega} \quad \text{on } \Gamma_N^p \tag{2.51}$$

$$p = \bar{p} \quad \text{on } \Gamma_D^p \tag{2.52}$$

$$p(\mathbf{r}, 0) = p_0 \quad \forall\ \mathbf{r} \in \Omega \tag{2.53}$$

$$\mathbf{u}(\mathbf{r}, 0) = \mathbf{u}_0 \quad \forall\ \mathbf{r} \in \Omega \tag{2.54}$$

where $\mathbf{t}$ is the traction vector, $\bar{\mathbf{u}}$ and $\bar{p}$ are the prescribed displacement vector and pressure, $\dot{\omega}$ is the volumetric flux and $p_0$ is the pore pressure field at the initial state $t = 0$.

CHAPTER

# 3

# COMPUTATIONAL GRID

Before introducing the numerical formulation of the mathematical models present in the previous chapter, it is convenient to perform a detailed description of the computational grid employed in this work. The term “computational grid", hereafter, refers to spatial domains, as it can be also applied to time domains. The basic geometric entities composing a three-dimensional unstructured grid are presented, as well as the procedure for building each of them. Finally, it is shown how the computational grid is employed as a geometric base for the numerical computations during the discretization process.

Strictly speaking, some of the topics discussed in this section are not essential for the main goals of this work, but it does contribute with the completeness of the overall presentation.

## 3.1 Geometrical aspects

The numerical solution of partial differential equations (PDE’s) is achieved by solving a system of algebraic equations obtained through a discretization method. The discretization of PDE’s refers exactly to the procedure of obtaining these algebraic equations. There are several discretization methods for PDE’s and most of them (not all, e.g. meshless methods) is closely linked to a computational grid. This is the case, for instance, for the finite volume, finite difference and finite element methods.

As well defined by Hurtado (2011), a computational grid is composed of geometrical entities used for obtaining a discrete representation of a continuum domain, and its purpose “is to provide geometrical support for the discretization process of governing equations defined in this domain". In other words, prior to the discretization of the PDE’s, the domain has to be discretized, i.e. a computational grid has to be generated in order to represent the solution domain in a discrete manner.

There are several types of grids and each of them is suitable for a different type of discretization technique. In a structured grid, for example, the numbering of the different geometrical entities follows a logical ordering, and each element (except for the boundaries) has always the same number of neighbors. Due to these features, structured grids are indispensable when finite difference or spectral methods are to be used. However, structured grids lack of geometrical flexibility precisely because it requires a logical numbering of geometrical entities, which makes them unsuitable for representing complex and irregular domains. Alternatively, unstructured grids are much more flexible as they do not require an ordered numbering of entities. Instead, the connectivity (Frey & George, 2000) between nodes is explicitly informed (Hurtado, 2011), which allows for the use of elements of different types (e.g. tetrahedra, hexahedra, pyramids and prisms), as well as local grid refinements. These features provide significant geometrical flexibility for unstructured grids. Finite element and finite volume methods are naturally applied to these types of grids.

Most of the grid generators for three-dimensional unstructured grids rely on tetrahedral elements, as they are easier to perform. Although they are difficult to generate, hexahedral grids are also attractive as they are usually more accurate than tetrahedral grids. For instance, hexahedral elements are often applied close to walls in order to better capture boundary layers, or in the near-well region in reservoir simulations, where the pressure field has a radial pattern. In this context, hybrid grids are particularly attractive as they mix elements of different types. These types of grids try to find a balance between efficiency, by applying tetrahedral elements in the vast majority of the domain, and accuracy, by employing hexahedra in specific regions of interest. Evidently, as discussed by Hurtado (2011), a grid composed of hexahedral and tetrahedral elements necessarily requires special elements in order to perform the transition between triangular and quadrilateral facets [1]. In general, these special elements are prisms with triangular base (also known as wedges) and pyramids with a quadrilateral base.

The grid generators provide to the user the so-called *primal* grid, that is, the grid composed of basic element shapes, e.g. tetrahedra, hexahedra, wedges and/or pyramids. Roughly speaking, the primal grid is provided as a table of node coordinates (element vertices) and a table of connectivity specifying the element indexes and how the nodes are connected in order to compose the elements, as detailed in Hurtado (2011). The finite element method, as well as the cell-center finite volume formulation (where the elements themselves are the control volumes), are directly applied to the primal grid. By contrast, a cell-vertex method, as the EbFVM, creates control volumes around every grid node, which is recognized as a second grid and it is often called *dual* grid. A representation of these two grids is illustrated in Figure 3.1. A primal grid is represented in Figure 3.1a, with the elements colored with slightly different colors. Figure 3.1b, the correspondent dual grid is illustrated, where different colors are assigned to the control volumes associated to each node of the grid.

**Figure 3.1** – (a) Primal grid and (b) dual grid.

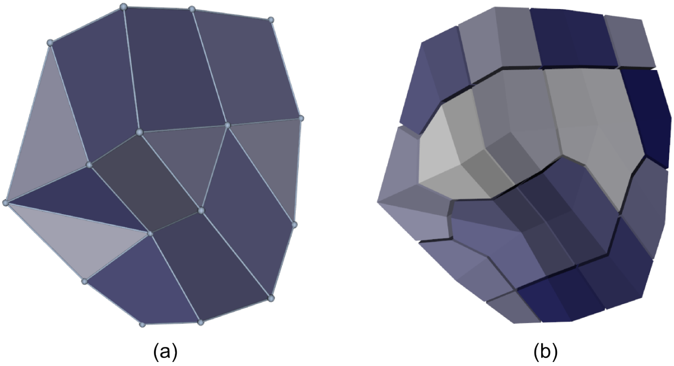
(a) (b)

Source: Own authorship.

It is important to stress that the primal and dual grids are not independent from each other, since one is built based on the other. That is to say, for a given primal grid, there is always one dual grid associated. In

---

[1] The concept of facet is defined later in this chapter.

fact, even with the control volume being the most important geometrical entity in the EbFVM (and in any other FVM), both grids are simultaneously employed for the numerical formulation. The following sections provide some details on the geometrical aspects of these two types of grids.

### 3.1.1 Primal grid

The basic entities of a three-dimensional primal grid are the elements, the facets[2], the edges and the vertices, as indicated in Figure 3.2. These entities present a hierarchical relationship, where an entity of dimension $d = N$ is directly composed of entities with dimension $d = N - 1$. For instance, three-dimensional elements ($d = 3$) are composed of facets ($d = 2$), which are composed of edges ($d = 1$), and each edge is composed of two vertices with dimension $d = 0$, as they represent a point with no dimensions in space. Each one of these primal entities are depicted in Figure 3.2.

**Figure 3.2** – Basic entities composing the primal grid.

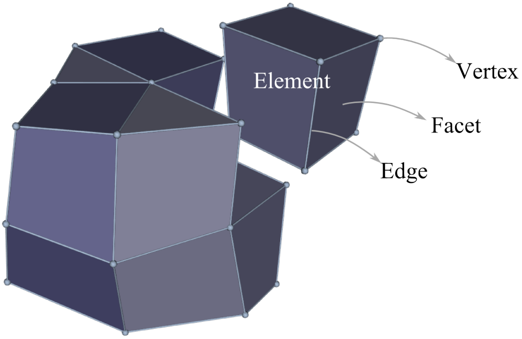

Source: Own authorship.

According to Frey & George (2000), the topology of a three-dimensional element can be completely described in terms the its facets, edges and vertices. However, for the purposes of this work, the topologies of the four

---

[2] As adopted by Hurtado (2011), the word “facet” refers to the external faces of the element. The word “face” is reserved to the internal faces of the element, as explained later on this chapter.

**Figure 3.3** – Lists of coordinates and connectivity of a portion of primal grid.

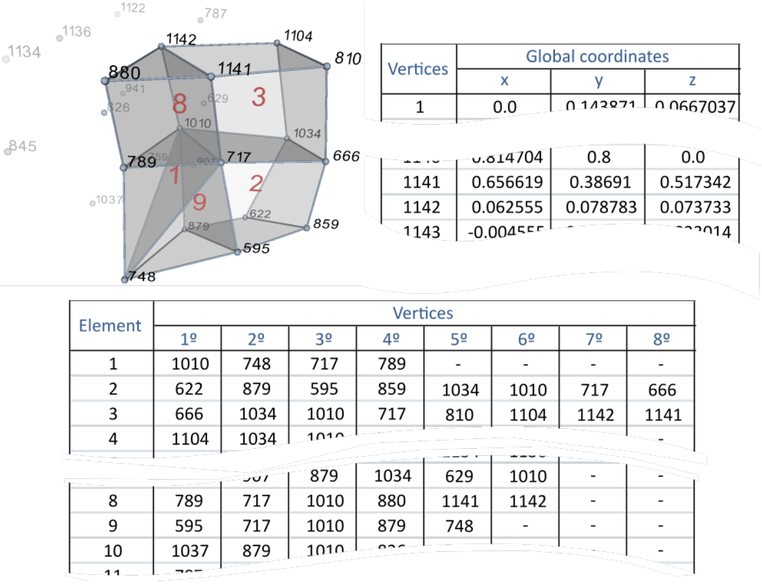

| Vertices | Global coordinates | | |
|---|---|---|---|
| | x | y | z |
| 1 | 0.0 | 0.143871 | 0.0667037 |
| [illegible] | 0.814704 | 0.8 | 0.0 |
| 1141 | 0.656619 | 0.38691 | 0.517342 |
| 1142 | 0.062555 | 0.078783 | 0.073733 |
| 1143 | [illegible] | [illegible] | [illegible] |

| Element | Vertices | | | | | | | |
|---|---|---|---|---|---|---|---|---|
| | 1º | 2º | 3º | 4º | 5º | 6º | 7º | 8º |
| 1 | 1010 | 748 | 717 | 789 | - | - | - | - |
| 2 | 622 | 879 | 595 | 859 | 1034 | 1010 | 717 | 666 |
| 3 | 666 | 1034 | 1010 | 717 | 810 | 1104 | 1142 | 1141 |
| 4 | 1104 | 1034 | [illegible] | [illegible] | [illegible] | [illegible] | [illegible] | - |
| [illegible] | [illegible] | [illegible] | 879 | 1034 | 629 | 1010 | - | - |
| 8 | 789 | 717 | 1010 | 880 | 1141 | 1142 | - | - |
| 9 | 595 | 717 | 1010 | 879 | 748 | - | - | - |
| 10 | 1037 | 879 | [illegible] | [illegible] | [illegible] | [illegible] | [illegible] | - |

Source: Own authorship.

types of elements are described by their vertex connectivity only. This can be achieved by adopting a logical numbering for the element vertices in such a way that the facets and edges can be implicitly built. As already mentioned, the primal grid is provided by the grid generator through a list of coordinates of each vertex, where for each vertex (node) is assigned an index from 1 to the number of vertices, $n$, and a list of connectivity of the vertices of each element. An example of these lists is illustrated in Figure 3.3.

The grid generator is responsible for organizing the vertices in the table of connectivity by following a fixed ordering for each type of element. In this manner, the grid flexibility is not affected and facets and edges can be implicitly taken in terms of the element vertices. In the sequence, the topology of each type of element, as well as the logical ordering of their vertices, are presented.

#### 3.1.1.1 Tetrahedron

A tetrahedron has the most simple topology among the three-dimensional elements. It is composed of only 4 vertices, 4 facets and 6 edges. The numbering of its vertices is performed following the right-hand rule, with the positive sense pointing to the opposite vertex. An example of such procedure is depicted in Figure 3.4. One of the possible choices would be 1-2-3-4, since vertex 4 is in the positive side of the facet 1-2-3. The vertices indicated in Figure 3.4 receive local numbers from 1 to 4, however, to each of them is assigned a global index corresponding to the indexes in the list of coordinates. Considering the tetrahedral element with index 1 in the table of coordinates of Figure 3.3, another valid sequence could be 717-1010-748-789.

**Figure 3.4** – Local vertex numbering of facets and edges of a tetrahedral element.

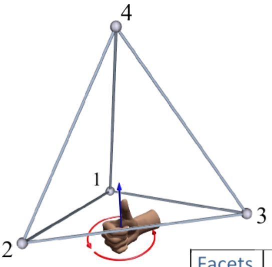

| Edges | Vertices | |
|---|---|---|
| 1 | 1 | 2 |
| 2 | 2 | 3 |
| 3 | 3 | 1 |
| 4 | 4 | 1 |
| 5 | 4 | 2 |
| 6 | 4 | 3 |

| Facets | Vertices | | |
|---|---|---|---|
| 1 | 1 | 3 | 4 |
| 2 | 1 | 2 | 3 |
| 3 | 1 | 4 | 2 |
| 4 | 2 | 3 | 4 |

Source: Own authorship.

#### 3.1.1.2 Hexahedron

The hexahedral element has 8 vertices, 6 facets and 12 edges. Each facet of a hexahedron is composed of four vertices, which implies that their are not necessarily coplanar. By choosing a given facet, its vertices are numbered following the right-hand rule with the thumb (positive sense) pointing to the opposite facet. Once the vertices of the first facet are numbered, the vertices of the opposite facet are numbered in the same sense as the previous facet. The vertices of the hexahedron of Figure 3.5, for example, can be numbered as 3-7-8-4-2-6-5-1. The numbering of the vertices belonging to facets and vertices is taken implicitly and it is also illustrated in Figure 3.5.

**Figure 3.5** – Local vertex numbering of facets and edges of a hexahedral element.

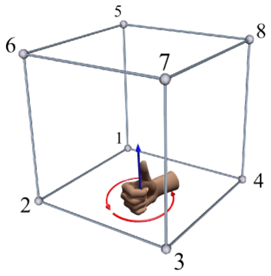

| Facets | Vertices | | | |
|---|---|---|---|---|
| 1 | 1 | 5 | 6 | 2 |
| 2 | 2 | 6 | 7 | 3 |
| 3 | 3 | 7 | 8 | 4 |
| 4 | 4 | 8 | 5 | 1 |
| 5 | 1 | 2 | 3 | 4 |
| 6 | 5 | 8 | 7 | 6 |

| Edges | Vertices | |
|---|---|---|
| 1 | 1 | 2 |
| 2 | 2 | 3 |
| 3 | 3 | 4 |
| 4 | 4 | 1 |
| 5 | 5 | 6 |
| 6 | 6 | 7 |
| 7 | 7 | 8 |
| 8 | 8 | 5 |
| 9 | 1 | 5 |
| 10 | 2 | 6 |
| 11 | 3 | 7 |
| 12 | 4 | 8 |

Source: Own authorship.

#### 3.1.1.3 Prism (wedge)

In the context of the present work, a prism refers to a solid figure with two opposite triangular facets. The three remaining facets are quadrilaterals and not necessarily coplanar. Since it is not exactly the definition os a prism, according to Hornby (2000), the word "wedge" is often used to refer to the solid shape as depicted in Figure 3.6. In this context, the prism (or wedge) have 6 vertices, 5 facets and 9 edges. The numbering of its vertices is performed exactly in the same manner as for the hexahedron, but starting necessarily from one of its triangular facets. By considering the prismatic element of Figure 3.6, for instance, a possible numbering could be 1-2-3-4-5-6 or else 4-6-5-1-3-2. The numbering of its facets and edges are also indicated in Figure 3.6.

**Figure 3.6** – Local vertex numbering of facets and edges of a prismatic element.

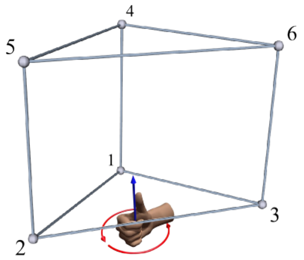

| Edges | Vertices | |
|---|---|---|
| 1 | 1 | 2 |
| 2 | 2 | 3 |
| 3 | 3 | 1 |
| 4 | 4 | 5 |
| 5 | 5 | 6 |
| 6 | 6 | 4 |
| 7 | 1 | 4 |
| 8 | 2 | 5 |
| 9 | 3 | 6 |

| Facets | Vertices | | | |
|---|---|---|---|---|
| 1 | 1 | 2 | 3 | - |
| 2 | 4 | 5 | 6 | - |
| 3 | 1 | 4 | 5 | 2 |
| 4 | 2 | 5 | 6 | 3 |
| 5 | 3 | 6 | 4 | 1 |

Source: Own authorship.

#### 3.1.1.4 Pyramid

A pyramid is defined as a solid shape with the base facet composed of an arbitrary number of edges (a polygon). The remaining facets are all triangular and they all share a common vertex that does not belong to the base facet. In this definition, the tetrahedal element also fits in this category. However, in this work, the word "pyramid" always refers to the case where the base facet is quadrilateral. As a consequence, the pyramid referred hereafter is composed of 5 vertices, 8 edges and 5 facets (1 quadrilateral and 4 triangular facets). The vertex numbering is performed in the same manner as in the tetrahedron, but starting from the quadrilateral facet. For instance, 4-1-2-3-5 is a valid sequence. The vertex connectivities of its edges and facets are also indicated in Figure 3.7.

### 3.1.2 Dual grid

As already mentioned, the EbFVM is a cell-vertex formulation since the control volumes are built around the grid nodes of the primal grid, which originates a second grid called dual grid. These control volumes are built in such a way that there is a one-to-one correspondence between the primal and the dual grid. In other words, for a given primal grid there exist

**Figure 3.7** – Local vertex numbering of facets and edges of a pyramidal element.

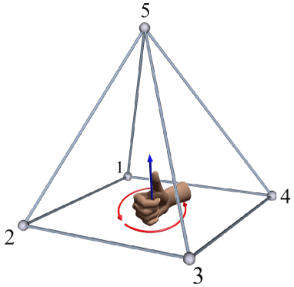

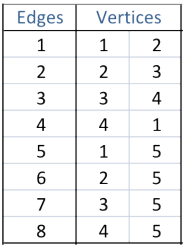

| Edges | Vertices | |
|---|---|---|
| 1 | 1 | 2 |
| 2 | 2 | 3 |
| 3 | 3 | 4 |
| 4 | 4 | 1 |
| 5 | 1 | 5 |
| 6 | 2 | 5 |
| 7 | 3 | 5 |
| 8 | 4 | 5 |

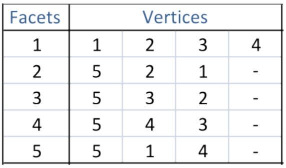

| Facets | Vertices | | | |
|---|---|---|---|---|
| 1 | 1 | 2 | 3 | 4 |
| 2 | 5 | 2 | 1 | - |
| 3 | 5 | 3 | 2 | - |
| 4 | 5 | 4 | 3 | - |
| 5 | 5 | 1 | 4 | - |

Source: Own authorship.

only one correspondent dual grid associated, and vice versa. In addition, there is also a one-to-one relationship between the individual entities of the primal and dual grids. These individual entities are referred hereafter as primal entities and dual entities. This relationship ensures that for a given primal entity there is always a correspondent dual entity. The most important dual entities are the element faces, the sub-elements and the control volumes, which, as it will be discussed, is regarded as a composite dual entity. The procedure for building each of these dual entities are now described. Further details can be found in Hurtado (2011).

#### 3.1.2.1 Faces

The element faces are dual entities associated to the edges of the primal grid. This means that every edge of an element has a correspondent face associated to it. For instance, Figure 3.8 illustrates the faces associated to the edges 1-2 of a hexahedron, a tetrahedron and a prism. For these elements the face associated to the edge 1-2 is built by connecting points A-B-C-D, where A is the midpoint of edge 1-2, C is the barycenter of the element vertices and points B and D are the barycenters of the two facets sharing the same edge 1-2.

**Figure 3.8** – Faces of hexahedral, tetrahedral and prismatic elements.

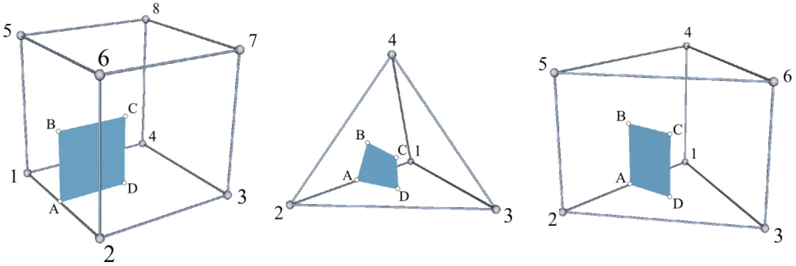

Source: Own authorship.

This procedure for building the element faces is called barycentric, and it ensures that the quadrilateral faces are coplanar if the element facets are coplanar as well. For the pyramid, however, this cannot be ensured and thus the procedure for building its faces is slightly modified (Hurtado, 2011). In this type of element, point C coincides with the barycenter of the base facet (quadrilateral facet), which implies that the faces associated to the edges belonging to the base facet are all triangular, and thus planar. The element faces associated to the remaining edges are still quadrangular though, as depicted in Figure 3.9.

**Figure 3.9** – Faces of a pyramid.

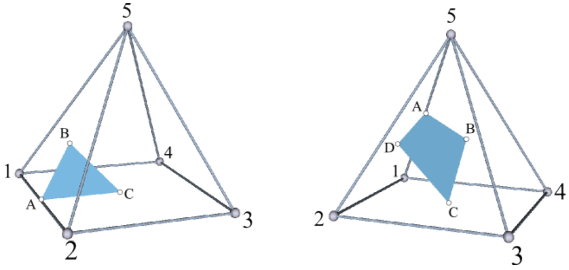

Source: Own authorship.

It should be also noted that, to each edge of a given element only one face is associated. However, a given edge can be shared by more than one element, and in this case the edge can have as many faces as there are elements sharing this edge. Furthermore, it can be said that a given face is associated to only one edge, but this edge can have more than one face associated depending on the number of elements sharing it.

#### 3.1.2.2 Sub-elements

A sub-element is a dual entity associated to each vertex of an element. In this sense, the sub-element can be interpreted as portions of the element surrounding its vertices. In order to understand how the sub-elements are build, it is convenient to introduce the concept of sub-facet, which is nothing but subdivisions of the element facets. These subdivisions are realized by connecting the barycenter of the facet to the midpoints of its edges. Figure 3.10, for example, shows the sub-facets of a tetrahedral element. In this figure, point C is the barycenter of facet 1-2-4 and points A, B and C are the midpoints of edges 1-2, 2-4, 4-1, respectively. The procedure for building the sub-facets is exactly the same for the other types of elements.

**Figure 3.10** – Sub-facets associated to facet 1-2-4 of a tetrahedral element.

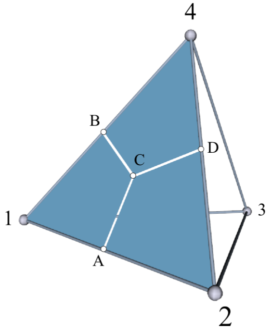

Source: Own authorship.

Except when it comes to boundary grids, as it will be shown later in this chapter, the sub-facet is not regarded as a dual entity. Instead, it is merely a formalism to define the region comprised by the sub-element. In this manner, the sub-element is the portion of the element bounded by all faces and sub-facets associated to the set of edges and facets, respectively, sharing a same vertex. Figure 3.11 shows the faces and sub-facets associated to vertex 1 and its correspondent sub-element.

**Figure 3.11** – Set of faces and sub-facets that compose a sub-element.

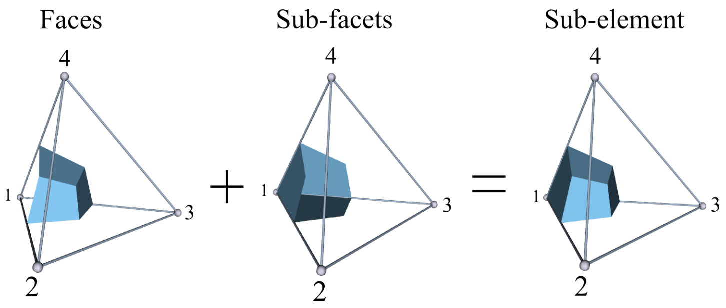

Source: Own authorship.

The procedure for building the sub-elements is exactly the same for the four types of elements. Figure 3.12 shows an exploded view of the sub-elements associated to each vertex of a hexahedron, a pyramid, a tetrahedron and a prism.

**Figure 3.12** – Sub-elements associated to the vertices of a (a) hexahedron, (b) tetrahedron, (c) pyramid and (d) prism.

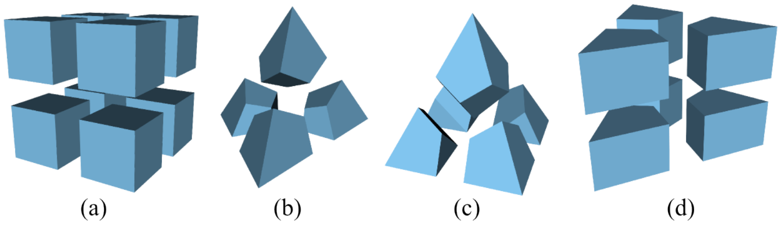

Source: Own authorship.

#### 3.1.2.3 Composite dual entities

To every primal entity is associated dual entities and composite dual entities. As a general rule, every primal entity is shared by more than one element, which means that this primal entity actually has more than one dual entity associated to it depending on the number of elements that share the same primal entity. In this manner, the composite dual entity is composed of the union of all dual entities associated to a given primal entity. In this work restricts to presenting only the composite dual entity

**Figure 3.13** – Control volume built around an internal vertex, shown as a pink dot in the exploded view on the right.

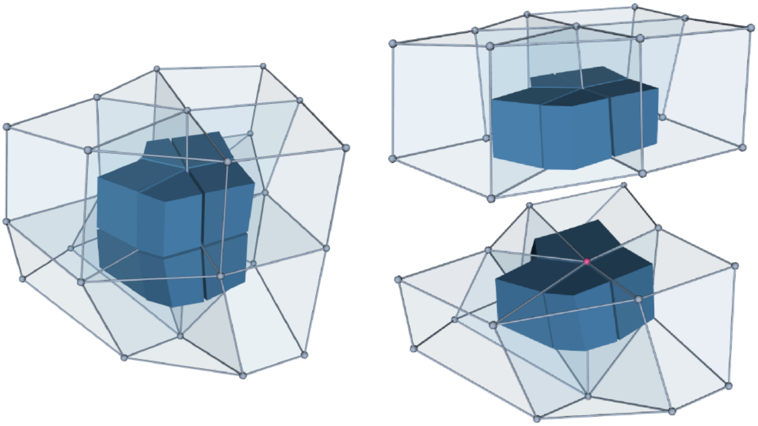

Source: Own authorship.

associated to the nodes of the grid, as it is the main entity of the dual grid for the EbFVM. More details about the remaining composite dual entities are provided by Hurtado (2011).

By considering the set of elements sharing a common vertex, the union of all sub-elements associated to this common vertex forms its composite dual entity, which is called control volume. The sub-elements that compose the control volume are also often referred to as sub-control volumes. Alternatively, one can state that the control volume associated to an internal vertex[3] of the grid is bounded by the set of faces associated to all the edges connecting to this internal vertex. Figure 3.13 shows the control volume built around an internal vertex of a portion of unstructured grid. On the right of this figure, the portion of the grid is split into two parts in order to highlight the internal vertex to which the control volume is associated to. By taking a closer look on the left image of Figure 3.13 it can be seen small gaps between the sub-control volumes. These gaps are only for visualization purposes and they do not actually exist.

---

[3] The vertex is said to be internal if it does not belong to the boundary.

### 3.1.3 Boundary grids

It is imperative to identify the regions of the grid that coincide with the boundaries of the computational domain, since this is precisely where the boundary conditions are applied. During the geometry preparation, the user has to inform the software where the boundaries of the domain are, so when the grid is generated a boundary grid file is also available. The boundary grid file has to provide the vertex connectivity and the numbering of the boundary elements. The three-dimensional elements considered in this work originate triangular and quadrilateral boundary elements, and the numbering of their vertices also follows the right-hand rule, with positive sense (the thumb) pointing outward the geometry. The boundary grid file does not have to provide a list of coordinates of the vertices, but the indexes of its vertices must correspond to the global indexes provided in the list of coordinates of the three-dimensional grid.

The concepts of primal and dual grid are also applied to the boundary grid. The triangular and quadrilateral elements associated to the boundaries of the geometry compose the primal boundary grid, which is provided by the grid generator. The dual boundary grid is built based on the primal entities through the same process already described for building the sub-facets, as illustrated in Figure 3.10. The important thing to keep in mind when it comes to boundary grid is that the facet of a primal three-dimensional element correspond to the primal boundary element itself and, therefore, the sub-facets depicted in Figure 3.10 correspond to a sub-element of the boundary element. Figure 3.14 depicts a primal and a dual boundary grid. Also in this case these two grids present a one-to-one relationship.

The last thing to address is how to build the control volume associated to a vertex belonging to the boundary of the domain. As already discussed, the control volume is bounded by the set of faces associated to every edge sharing a common vertex. This set of faces can be named as a control surface. When the vertex belongs to the boundary of the domain, the control surface associated to this vertex is not exclusively composed of the element faces anymore. In this case, as indicated in Figure 3.15, the sub-elements[4] (or sub-facets of the three-dimensional element) of the

---

[4] Remember that, in the case of a boundary grid, the sub-element is the same as the subfacet in the three-dimensional grid

**Figure 3.14** – (a) Primal and (b) dual boundary grids.

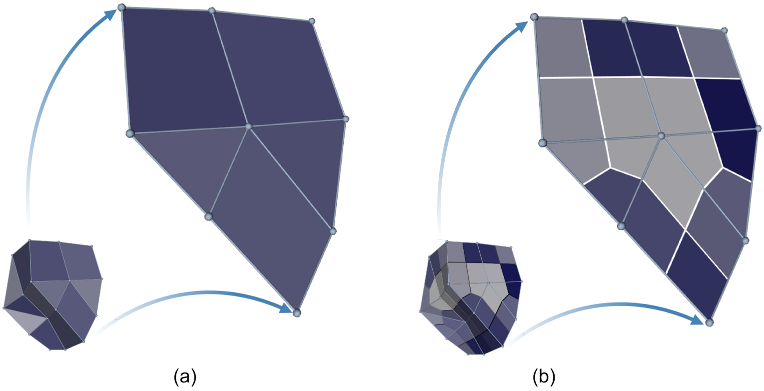

Source: Own authorship.

**Figure 3.15** – Control volume associated to a boundary vertex.

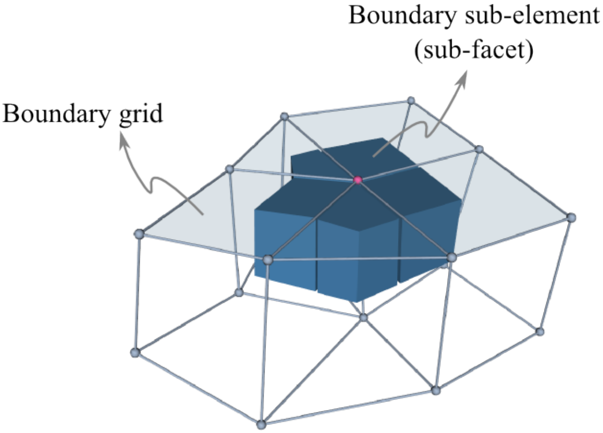

Source: Own authorship.

boundary grid associated to the vertex will also compose the control surface. It is important to stress that a boundary element corresponds to one of the facets of a three-dimensional element in contact with the boundary of the domain. In this manner, there is a correspondence between the boundary element and a facet, and between a boundary sub-element and a sub-facet.

## 3.2 Numerical aspects

In the previous section, it was presented, in a qualitative manner, the geometrical entities of a three-dimensional unstructured grid. It was introduced the concepts of primal and dual grids an their respective geometrical entities. The topology of the primal elements was also discussed, as well as the logical procedure for numbering the element vertices and how it allows for an implicit construction of facets and edges. It was also shown how to build the dual entities, namely the faces, sub-elements and the control volumes. To this point, the main concern was to identify and expose the relationships between the different geometrical entities associated to the primal and dual grids.

The computational grid, however, merely serves as a geometrical support for performing numerical computations. The discretization process of partial differential equations requires the computation of face areas, volumes, interpolation of variables and approximation of gradients on different positions over the computational grid. Thus, it still remains to be defined how exactly the grid will be employed as a geometrical support for the numerical method (in this case, the EbFVM). As it should be expected, there are different ways of performing this task and a careful definition of this subject, aside from affecting the flexibility of the numerical method in dealing with different equations, can significantly improve the code implementation. These issues are discussed in the following subsections.

### 3.2.1 Coordinate transformation

Coordinate transformations are a common practice when using curvilinear structured grids generated from a generalized coordinate system, as it makes the computations easier to perform. A coordinate transformation relates the irregular geometry defined in the real domain of calculus to a regular geometry, with fixed dimensions, in a transformed domain. In this manner, all the computations are carried out in the transformed domain, since the transformed geometry is always regular[5] and

---

[5] By regular, we mean the geometry does not have a complex shape. Usually it takes the form of a cube in the transformed domain.

never changes. This is performed, however, at the cost of having to compute the metrics of the transformation (Maliska, 2004), but this is a procedure that can be easily automated and it can be performed just in the beginning of the simulation. This is, therefore, a very convenient strategy from a practical point of view.

The coordinate transformation is often applied to unstructured grids as well. In this case, however, the transformation is not applied to the geometry as a whole. Instead, a local transformation is applied to each element of the grid. By doing so, the irregular element in the real domain becomes into a regular element in the transformed domain. In this work, the local coordinate transformation applied to each element of the grid will be used in order to perform the numerical computations based on the grid. In what follows, it is shown how these transformations are applied to each type of element of the primal grid.

### 3.2.2 Shape functions

When dealing with local coordinate transformations, it is common to adopt the terms *global* and *local* coordinate systems. The former refers to the coordinate system from which the computational grid was originally generated, whereas the local coordinate system defines the transformed domain, whose axes are denoted in this work as $\xi$, $\eta$ and $\gamma$. An element represented in the transformed domain, evidently, also holds the same primal and dual entities already discussed. That is, facets, faces, sub-elements, etc., are also defined in the transformed domain. The local coordinates defining these entities in the transformed domain are known and immutable. By defining a linear transformation between these two types of coordinate systems, it is possible to perform all the required computations exclusively on the transformed domain and then transfer the results back to the original domain (global coordinate system). In Figure 3.16 is illustrated an example of a distorted hexahedron in the global coordinate system and its representation in the local coordinate system, where it assumes a regular shape. As an example, the local coordinates of point B of the element in the transformed domain are $\xi = \eta = \gamma = 1/2$, which represents the barycenter of the element vertices. The linear transformation must be capable of mapping the global coordinates of point B from the transformed domain to the real domain.

**Figure 3.16** – A distorted element in the real domain and its representation in the transformed domain. Point B represents the barycenter of the element vertices.

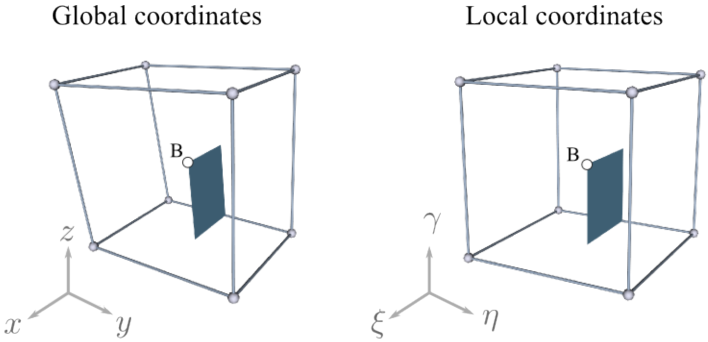

Source: Own authorship.

In unstructured grids it is common to use the so-called element shape as a linear transformation between the two coordinate systems. In this manner, by considering a given point $\bar{\mathbf{r}} = (\xi, \eta, \gamma)$ in the transformed domain, the correspondent $x$ coordinate in the real domain is given by:

$$x(\bar{\mathbf{r}}) = \sum_{i=1}^{m} N_i(\bar{\mathbf{r}})\, x_i, \tag{3.1}$$

where $m$ denotes the number of vertices of the element, $x_i$ is the $x$ coordinate of each vertex $i$ of the element, which are known from the list of coordinates (see Figure 3.3), and $N_i(\xi, \eta, \gamma)$ is the element shape function associated to vertex $i$ evaluated at the local coordinates $\bar{\mathbf{r}} = (\xi, \eta, \gamma)$, that is, $N_i(\bar{\mathbf{r}}) = N_i(\xi, \eta, \gamma)$. Therefore, in the EbFVM, each element of the grid has always $m$ shape functions[6]. The shape functions are known expressions that depend on the local coordinates $(\xi, \eta, \gamma)$ and are defined for each type of element. Each shape function $N_i$ assumes the unit value when evaluated at vertex $i$, zero at the other vertices and some value in between zero and one at the remaining positions inside the element. In addition, the summation of all shape functions at a given point inside the element is always equal to one, that is:

---

[6] In FEM, higher order elements, where the number of nodes of an element is greater than its number of vertices, might also be used. In this case, the number of shape functions is different from the number of vertices $m$.

$$\sum_{i=1}^{m} N_i\left(\xi,\eta,\gamma\right)=1 \tag{3.2}$$

The Equation 3.1 for obtaining the $x$ coordinate corresponding to a local coordinate $\bar{\mathbf{r}}$ can be also written in matrix notation, which will be particularly convenient throughout the text,

$$x\left(\bar{\mathbf{r}}\right)=\mathbf{N}^T\left(\bar{\mathbf{r}}\right)\mathbf{x}^e \tag{3.3}$$

where $\mathbf{N}$ is a $(m\times 1)$ vector containing the element shape functions, that is:

$$\mathbf{N}=\begin{bmatrix}N_i & \cdots & N_m\end{bmatrix}^T \tag{3.4}$$

and $\mathbf{x}^e$ is a $(m\times 1)$ vector containing the $x$ coordinates of the element vertices:

$$\mathbf{x}^e=\begin{bmatrix}x_i & \cdots & x_m\end{bmatrix}^T. \tag{3.5}$$

In order to keep a clean and concise notation, when the position in the transformed domain is not strictly important, the term $(\bar{\mathbf{r}})$ might be dropped from Equation 3.3, so it can be written as:

$$x=\mathbf{N}^T\mathbf{x}^e \tag{3.6}$$

The global coordinates $\mathbf{r}=[x,y,z]^T$ correspondent to a point $\bar{\mathbf{r}}=(\xi,\eta,\gamma)$ can also be written in terms of the global coordinates of the element vertices by the following matrix multiplication:

$$\mathbf{r}=\mathbf{N}_s^T\mathbf{r}^e \tag{3.7}$$

where $\mathbf{N}_s$ is a special arrangement of the element shape functions, that is,

$$\mathbf{N}_s^T=\begin{bmatrix}\mathbf{N}^T & 0 & 0\\ 0 & \mathbf{N}^T & 0\\ 0 & 0 & \mathbf{N}^T\end{bmatrix}. \tag{3.8}$$

In addition,

$$\mathbf{r}^e=\begin{bmatrix}x_1 & \cdots & x_m & y_1 & \cdots & y_m & z_1 & \cdots & z_m\end{bmatrix}^T \tag{3.9}$$

or simply,

$$\mathbf{r}^e = \left[ (\mathbf{x}^e)^T \quad (\mathbf{y}^e)^T \quad (\mathbf{z}^e)^T \right]^T. \tag{3.10}$$

As it can be verified, the dimensions of $\mathbf{N}_s^T$ and $\mathbf{r}^e$ are $(3 \times 3m)$ and $(3m \times 1)$, respectively.

The shape functions represent the linear transformation responsible for transferring information from one domain to another. Although they have been presented, to this point, in a qualitative manner, they have not been defined yet. In fact, each type of element has a different set of shape functions associated to it. The linear transformations for each type of element is now presented.

### Tetrahedron

Figure 3.11 shows a tetrahedral element in the transformed domain. The table on the right-side of this figure shows the local coordinates $(\xi, \eta, \gamma)$ of each one of its four vertices. The shape functions associated to these vertices are the following:

**Figure 3.17** – Tetrahedral representation in the transformed domain.

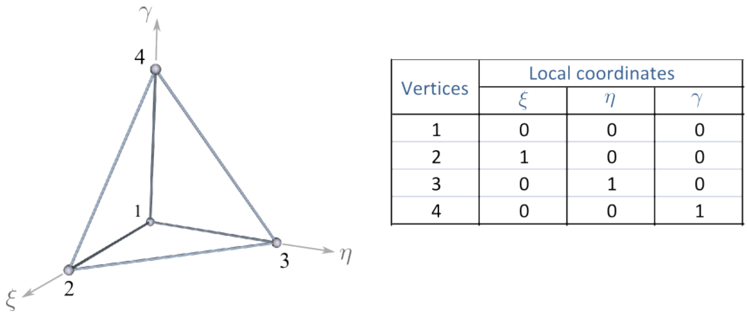

| Vertices | Local coordinates | | |
|---|---|---|---|
| | ξ | η | γ |
| 1 | 0 | 0 | 0 |
| 2 | 1 | 0 | 0 |
| 3 | 0 | 1 | 0 |
| 4 | 0 | 0 | 1 |

Source: Own authorship.

$$\begin{aligned} N_1(\xi,\eta,\gamma) &= 1-\xi-\eta-\gamma, \\ N_2(\xi,\eta,\gamma) &= \xi, \\ N_3(\xi,\eta,\gamma) &= \eta, \\ N_4(\xi,\eta,\gamma) &= \gamma. \end{aligned} \tag{3.11}$$

**Figure 3.18** – Hexahedral representation in the transformed domain.

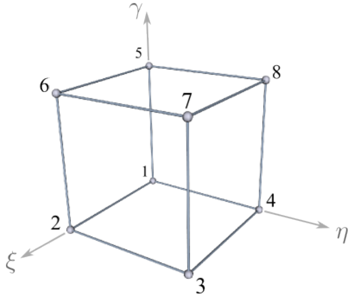

| Vertices | Local coordinates | | |
|---|---|---|---|
| | $\xi$ | $\eta$ | $\gamma$ |
| 1 | 0 | 0 | 0 |
| 2 | 1 | 0 | 0 |
| 3 | 1 | 1 | 0 |
| 4 | 0 | 1 | 0 |
| 5 | 0 | 0 | 1 |
| 6 | 1 | 0 | 1 |
| 7 | 1 | 1 | 1 |
| 8 | 0 | 1 | 1 |

Source: Own authorship.

As it can be seen, the shape functions associated to tetrahedral element are linear, so their derivatives with respect to the local coordinates are all constant.

### Hexahedron

When a hexahedron is mapped into a transformed plane it conveniently takes the form of a cube with unitary edges, as shown in Figure 3.18. This element in the transformed domain is always bounded by $0 \leqslant \xi \leqslant 1$, $0 \leqslant \eta \leqslant 1$ and $0 \leqslant \gamma \leqslant 1$. From the local coordinates provided in the table of Figure 3.18 it can be concluded that the facets in the transformed domain are always coplanar. The shape functions associated with the vertices of a hexahedral element depicted in Figure 3.18 are the following:

$$
\begin{aligned}
N_1(\xi,\eta,\gamma) &= (1-\xi)(1-\eta)(1-\gamma), \\
N_2(\xi,\eta,\gamma) &= \xi(1-\eta)(1-\gamma), \\
N_3(\xi,\eta,\gamma) &= \xi\eta(1-\gamma), \\
N_4(\xi,\eta,\gamma) &= (1-\xi)\eta(1-\gamma), \\
N_5(\xi,\eta,\gamma) &= (1-\xi)(1-\eta)\gamma, \\
N_6(\xi,\eta,\gamma) &= \xi(1-\eta)\gamma, \\
N_7(\xi,\eta,\gamma) &= \xi\eta\gamma, \\
N_8(\xi,\eta,\gamma) &= (1-\xi)\eta\gamma.
\end{aligned}
\tag{3.12}
$$

The shape functions of a hexahedron are always trilinear and their derivatives with respect to the local coordinates also depend on the local coordinates.

### Prism

The prismatic element, by its turn, is bounded by $0 \leqslant \xi \leqslant 1-\eta$, $0 \leqslant \eta \leqslant\leqslant 1-\xi$ and $0 \leqslant \gamma \leqslant 1$, as shown in Figure 3.19. The local coordinates of its vertices are also presented in the table of Figure 3.19 and the shape functions are given by:

$$\begin{aligned}
N_1(\xi,\eta,\gamma) &= (1-\xi-\eta)(1-\gamma), \\
N_2(\xi,\eta,\gamma) &= \xi(1-\gamma), \\
N_3(\xi,\eta,\gamma) &= \eta(1-\gamma), \\
N_4(\xi,\eta,\gamma) &= (1-\xi-\eta)\gamma, \\
N_5(\xi,\eta,\gamma) &= \xi\gamma, \\
N_6(\xi,\eta,\gamma) &= \eta\gamma.
\end{aligned} \tag{3.13}$$

The shape functions in Equation 3.13 are bilinear and their derivatives also depend on the local positions.

### Pyramid

Finally, the pyramidal element in the transformed domain assumes the shape illustrated in Figure 3.20. The base of this element is a unit square bounded by $0 \leqslant \xi \leqslant 1$ and $0 \leqslant \eta \leqslant 1$. The local coordinates of

**Figure 3.19** – Prism represented in the transformed domain.

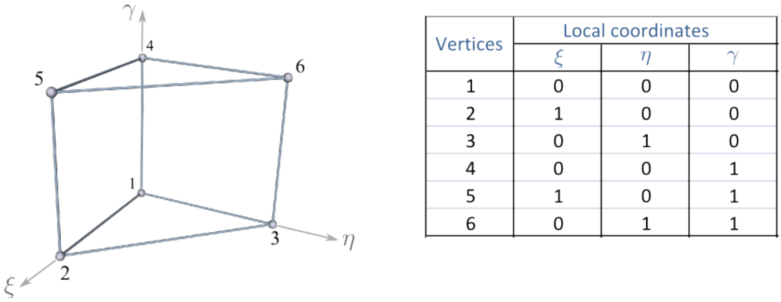

| Vertices | Local coordinates | | |
|---|---|---|---|
| | $\xi$ | $\eta$ | $\gamma$ |
| 1 | 0 | 0 | 0 |
| 2 | 1 | 0 | 0 |
| 3 | 0 | 1 | 0 |
| 4 | 0 | 0 | 1 |
| 5 | 1 | 0 | 1 |
| 6 | 0 | 1 | 1 |

Source: Own authorship.

its vertices are also shown in the table of Figure 3.20, from which it can be concluded that its facets in the transformed domain are also coplanar. The five shape functions in this case are the following:

**Figure 3.20** – Pyramid represented in the transformed domain.

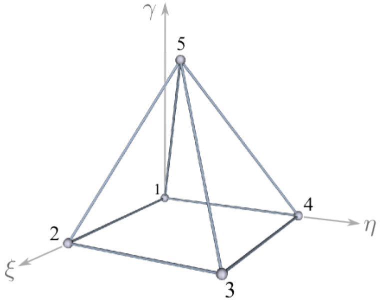

| Vertices | Local coordinates | | |
|---|---|---|---|
| | $\xi$ | $\eta$ | $\gamma$ |
| 1 | 0 | 0 | 0 |
| 2 | 1 | 0 | 0 |
| 3 | 1 | 1 | 0 |
| 4 | 0 | 1 | 0 |
| 5 | 1/2 | 1/2 | 1 |

Source: Own authorship.

$$\begin{aligned}
N_1(\xi,\eta,\gamma) &= (1-\xi)(1-\eta) - \tfrac{1}{4}\gamma + \left(\xi-\tfrac{1}{2}\right)\left(\eta-\tfrac{1}{2}\right)\gamma/(1-\gamma),\\
N_2(\xi,\eta,\gamma) &= \xi(1-\eta) - \tfrac{1}{4}\gamma - \left(\xi-\tfrac{1}{2}\right)\left(\eta-\tfrac{1}{2}\right)\gamma/(1-\gamma),\\
N_3(\xi,\eta,\gamma) &= \xi\eta - \tfrac{1}{4}\gamma + \left(\xi-\tfrac{1}{2}\right)\left(\eta-\tfrac{1}{2}\right)\gamma/(1-\gamma),\\
N_4(\xi,\eta,\gamma) &= (1-\xi)\eta - \tfrac{1}{4}\gamma - \left(\xi-\tfrac{1}{2}\right)\left(\eta-\tfrac{1}{2}\right)\gamma/(1-\gamma),\\
N_5(\xi,\eta,\gamma) &= \gamma.
\end{aligned} \tag{3.14}$$

The shape functions of Equation 3.14 present an odd behavior when they are evaluated at the local coordinates of vertex 5 ($\xi = \eta = 1/2$ and $\gamma = 1$). At this position the shape function $N_5$ results 1, as expected, but the remaining shape functions fall into an indeterminate division (0/0). Nevertheless, these shape functions are perfectly valid since, in practice, they are never required to be evaluated at the vertices of the element.

### 3.2.3 Jacobian matrix

Basically, the Jacobian matrix is responsible for transferring a vector from one domain to another. In the three-dimensional case the Jacobian matrix is defined as follows:

$$\mathbf{J}^T = \begin{bmatrix} x_\xi & y_\xi & z_\xi \\ x_\eta & y_\eta & z_\eta \\ x_\gamma & y_\gamma & z_\gamma \end{bmatrix}, \tag{3.15}$$

where $x_\xi$ is a short for $\partial x/\partial\xi$. The local derivatives[7] of the global coordinates are obtained by taking the local derivatives of the shape functions. The derivative $x_\xi$, for example, is obtained by deriving Equation 3.3 (or Equation 3.6) with respect to $\xi$. Regarding that the global coordinates $x_i$ are constant, $x_\xi$ is given by:

$$\frac{\partial x}{\partial \xi} = \sum_{i=1}^{m} N_{i,\xi} x_i = \mathbf{N}_\xi^T \mathbf{x}^e \tag{3.16}$$

with $N_{i,\xi}$ being a short for $\partial N_i/\partial\xi$ and,

$$\mathbf{N}_\xi^T = \begin{bmatrix} N_{1,\xi} & \cdots & N_{m,\xi} \end{bmatrix} \tag{3.17}$$

Expressions similar to Equation 3.16 are employed to compute the remaining entries of the Jacobian matrix of Equation 3.15, thus it can be computed as,

$$\mathbf{J}^T = \begin{bmatrix} N_{1,\xi} & N_{2,\xi} & \cdots & N_{m,\xi} \\ N_{1,\eta} & N_{2,\eta} & \cdots & N_{m,\eta} \\ N_{1,\gamma} & N_{2,\gamma} & \cdots & N_{m,\gamma} \end{bmatrix} \begin{bmatrix} x_1 & y_1 & z_1 \\ x_2 & y_1 & z_1 \\ \vdots & \vdots & \vdots \\ x_m & y_m & z_m \end{bmatrix}. \tag{3.18}$$

The matrices in the right-hand side of Equation 3.16 can be named as **D** and $\mathbf{C}^e$, respectively, so the Jacobian matrix can be written in the following compact form:

$$\mathbf{J}^T = \mathbf{D}\mathbf{C}^e. \tag{3.19}$$

Matrix **D** contains the local derivatives of the element shape functions and matrix $\mathbf{C}^e$ stores the global coordinates of the element vertices.

---

[7] In this case, a local derivative refers to a derivative with respect to the local coordinates.

### 3.2.4 Gradient approximation

Based on the global coordinates of the element vertices, the shape functions allow for the computation of the global coordinates of any position inside the element regarded that the local coordinates $(\xi,\eta,\gamma)$ of the desired position is known. In the same way, a general scalar field $\phi$, stored at the element vertices, can be interpolated at any position inside the element by the following expression:

$$\phi = \sum_{i=1}^{m} N_i \Phi_i \tag{3.20}$$

The local derivatives of $\phi$ are given by:

$$\begin{bmatrix} \phi_\xi \\ \phi_\eta \\ \phi_\gamma \end{bmatrix} = \begin{bmatrix} N_{1,\xi} & N_{2,\xi} & \cdots & N_{m,\xi} \\ N_{1,\eta} & N_{2,\eta} & \cdots & N_{m,\eta} \\ N_{1,\gamma} & N_{2,\gamma} & \cdots & N_{m,\gamma} \end{bmatrix} \begin{bmatrix} \Phi_1 \\ \Phi_2 \\ \vdots \\ \Phi_m \end{bmatrix} \equiv \mathbf{D}\,\mathbf{\Phi}^e, \tag{3.21}$$

where $\mathbf{\Phi}^e = \begin{bmatrix} \Phi_1 & \Phi_2 & \cdots & \Phi_m \end{bmatrix}^T$. On the other hand, the chain rule applied to the local derivatives of $\phi$ leads to:

$$\begin{aligned} \phi_\xi &= \phi_x x_\xi + \phi_y y_\xi + \phi_z z_\xi \\ \phi_\eta &= \phi_x x_\eta + \phi_y y_\eta + \phi_z z_\eta, \\ \phi_\gamma &= \phi_x x_\gamma + \phi_y y_\gamma + \phi_z z_\gamma \end{aligned} \tag{3.22}$$

or, in the matrix form,

$$\begin{bmatrix} \phi_\xi \\ \phi_\eta \\ \phi_\gamma \end{bmatrix} = \begin{bmatrix} x_\xi & y_\xi & z_\xi \\ x_\eta & y_\eta & z_\eta \\ x_\gamma & y_\gamma & z_\gamma \end{bmatrix} \begin{bmatrix} \phi_x \\ \phi_y \\ \phi_z \end{bmatrix} = \mathbf{J}^T \nabla\phi \tag{3.23}$$

In the right-hand side of Equation 3.23, it can be recognized the Jacobian matrix and the gradient of the scalar function, that is,

$$\nabla\phi = \begin{bmatrix} \phi_x & \phi_y & \phi_z \end{bmatrix}^T. \tag{3.24}$$

The local derivatives of $\Phi$ on the left-hand side of Equation 3.23 is represented as in Equation 3.21. Thereby, the gradient of a scalar field $\phi$

is computed by the following matrix products:

$$\mathbf{J}^T \nabla \phi = \mathbf{D}\,\mathbf{\Phi}^e \qquad \therefore \qquad \nabla \phi = \mathbf{J}^{-T} \mathbf{D}\,\mathbf{\Phi}^e, \tag{3.25}$$

where $\mathbf{B} = \mathbf{J}^{-T}\mathbf{D}$. Matrix $\mathbf{B}$ is often called the gradient operator, since its columns contain the coefficients that multiply the values of $\phi$ at the element vertices in order to recover its gradient.

### Gradient operators

The matrix product $\mathbf{J}^{-T}\mathbf{D}$ contains the global derivatives of the shape functions. Due to its importance, it is convenient to define a matrix $\mathbf{B}$ such that:

$$\mathbf{B} = \mathbf{J}^{-T}\mathbf{D} = \nabla \mathbf{N}^T = \begin{bmatrix} \mathbf{N}_x \\ \mathbf{N}_y \\ \mathbf{N}_z \end{bmatrix} = \begin{bmatrix} N_{1,x} & \cdots & N_{m,x} \\ N_{1,y} & \cdots & N_{m,y} \\ N_{1,z} & \cdots & N_{m,z} \end{bmatrix}, \tag{3.26}$$

where the nabla operator is $\nabla = \begin{bmatrix} \partial_x & \partial_y & \partial_z \end{bmatrix}^T$. Matrix $\mathbf{B}$ is often called the gradient operator, since its columns contain the coefficients that multiply the values of $\phi$ at the element vertices in order to recover its gradient.

Another useful definition is the symmetric gradient operator $\mathbf{B}_s$, which is obtained by the matrix product between the symmetric nabla operator (Equation 2.9) and the special arrangement of the element shape functions (Equation 3.8). Thus, the symmetric gradient operator is given by:

$$\mathbf{B}_s = \nabla_s \mathbf{N}_s = \begin{bmatrix} \mathbf{N}_x & 0 & 0 \\ 0 & \mathbf{N}_y & 0 \\ 0 & 0 & \mathbf{N}_z \\ \mathbf{N}_y & \mathbf{N}_x & 0 \\ 0 & \mathbf{N}_z & \mathbf{N}_y \\ \mathbf{N}_z & 0 & \mathbf{N}_x \end{bmatrix}. \tag{3.27}$$

As it can be verified, matrix $\mathbf{B}_s$ is just a special arrangement of the entries of matrix $\mathbf{B}$, thus the entries of matrix $\mathbf{B}_s$ are taken directly from Equation 3.26.

### 3.2.5 Areas and volumes

During the discretization of the partial differential equations, it is often required to compute areas and volumes of different entities of the computational grid. Being able to perform these computations is of fundamental importance for a finite volume method, as it requires the evaluation of surface and volumetric integrals on the dual grid. More specifically, efficient procedures must be defined for computing volumes of subelements and for building area vectors on the element faces.

**Figure 3.21** – Quadrilateral and triangular faces of a pyramid.

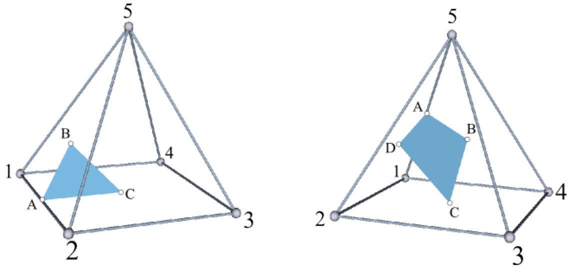

Source: Own authorship.

The face of an element can be characterized by its superficial area and by its orientation, thus an area vector $\mathbf{s}_f$ shall be computed for properly representing it. For the purposes of illustration, a pyramid is represented in Figure 3.21, where a triangular and a quadrilateral face are highlighted. For the quadrilateral face, the area vector can be computed by half of the cross product between the two vectors along its diagonals (Hurtado, 2011), that is:

$$\mathbf{s}_f = \frac{1}{2}\overrightarrow{DB} \times \overrightarrow{AC}. \tag{3.28}$$

For the triangular face in Figure 3.21, the area vector is computed in a similar way:

$$\mathbf{s}_f = \frac{1}{2}\overrightarrow{AB} \times \overrightarrow{AC}. \tag{3.29}$$

The procedure is exactly the same for computing the area vector of faces of every other type of element.

For computing the volume of sub-elements it is convenient to work on the transformed domain. In this coordinate system, the volumes of the sub-elements are always the same and a direct relationship with the volume of the corresponding sub-elements in the real domain can be established. This relationship is given by the determinant of the Jacobian matrix, as defined in Equation 3.15. Thus, the volume $\Delta V_s$ of a sub-element $s$ can be obtained by the following volumetric integral:

$$\Delta V_s = \int_s |\mathbf{J}| \mathrm{d}\overline{V}, \tag{3.30}$$

where $\mathrm{d}\overline{V}$ is a differential volume in the transformed domain. The integral of Equation 3.30 can be evaluated by a Gaussian quadrature in only one point located at the baricenter $\dot{s}$ of the sub-element. In this manner, the volumetric integral is replaced by:

$$\Delta V_s \approx |\mathbf{J}|_{\dot{s}} \Delta\overline{V}, \tag{3.31}$$

where $\Delta\overline{V}$ is the volume of the sub-element in the transformed domain and $|\mathbf{J}|_{\dot{s}}$ indicates that the determinant is evaluated at the baricenter of the sub-element. The volume as computed by Equation 3.31 is exact for a sub-element of a tetrahedral element, whereas it is only approximated for other types of elements (Hurtado, 2011).

CHAPTER

# 4

# NUMERICAL FORMULATION

In this chapter, the Element-base Finite Volume Method (EbFVM) is employed for obtaining the discrete representation of the governing equations described in Chapter 2. The EbFVM is firstly introduced in the context of the Weighted Residuals Method, which is a common root of a wide variety of numerical methods (see Figure 4.1). The reason for beginning with the WRM is twofold. On the one hand, it is interesting to provide a mathematical perspective on how the EbFVM works, since most of finite volume approaches are mainly based on physics and conservation principles. Besides, some readers used to Finite Element Methods may find easier to tackle the basic principles of EbFVM by recognizing its common roots with FEM. On the other hand, by fitting the EbFVM into the WRM framework it is possible to identify, based on the literature, some mathematical aspects of the discrete equations that may be the cause of the numerical instabilities in poroelasticity.

After providing this alternative perspective, some particular characteristics of the EbFVM are also presented. Most of the geometrical and numerical aspects discussed Chapter 3 are employed here for obtaining the discrete representation of mass and stress equilibrium equations. Finally, some details about the resulting linear system close this chapter.

**Figure 4.1** – Relationships between the various discretization methods for partial differential equations.

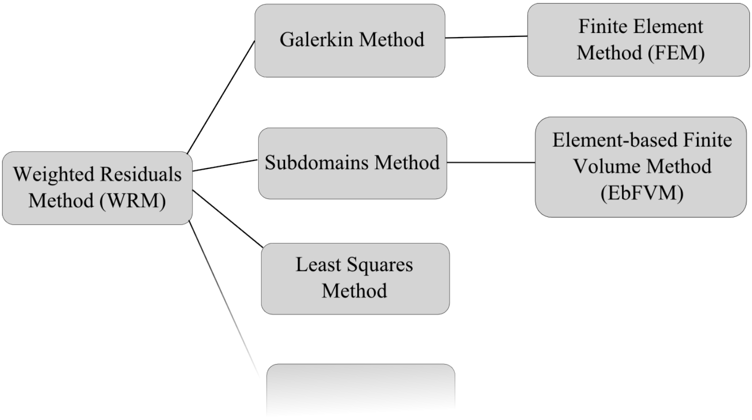

Source: Own authorship.

## 4.1 Weighted residuals method

The weighted residuals method (WRM) is a general framework from which several discretization techniques are based upon. In order to present this method, a general partial differential equation defined in the domain $\Omega$ is written as follows:

$$L(u) - f(\mathbf{x}) = 0, \qquad \mathbf{x} \in \Omega \tag{4.1}$$

where $f(\mathbf{x})$ is a known function and $L(\cdot)$ is a general differential operator that applies to the unknown function $u = u(\mathbf{x})$ in order to resemble any partial differential equation. In fact, Equation 4.1 equals to zero because $u = u(\mathbf{x})$ is regarded to be the exact solution of the PDE. However, $u = u(\mathbf{x})$ is often impossible to find, which leads to the use of numerical methods in order to obtain an approximate solution $\tilde{u}(\mathbf{x})$ for Equation 4.1. In this case, the residue $r(\mathbf{x})$ of Equation 4.1 is not zero, that is,

$$r(\mathbf{x}) = L(\tilde{u}) - f(\mathbf{x}) \neq 0. \tag{4.2}$$

Nonetheless, an approximate solution can be acceptable if the residue is restricted to a certain tolerance. The goal is then to find an approximate solution $\tilde{u}(\mathbf{x})$ pertaining to some finite function space $\mathscr{S}$ generated by $n$ independent trial functions $\phi_j(\mathbf{x})$, such that:

$$\tilde{u}(\mathbf{x}) = \sum_{j=1}^{n} u_j \phi_j(\mathbf{x}), \tag{4.3}$$

with $u_j$ being the unknown coefficients that have to be computed in order to minimize the residue $r(\mathbf{x})$. In addition, the trial functions have to satisfy three requirements:

1. they have to satisfy boundary conditions;
2. they have to be linearly independent from each other;
3. and, finally, they have to be at least $\mathrm{C}^0$ continuous over the domain $\Omega$.

Examples of possible trial functions in the one-dimensional case are:

$$\left.\begin{aligned} \phi_j(x) &= x^{j-1} \\ \phi_j(x) &= \sin(j\pi x) \end{aligned}\right. \qquad \forall \;\; j \in [1, n]$$

Since the trial functions are known, the problem reduces to find the coefficients $u_j$ of Eq. (4.3) that produces an acceptable residue. These coefficients are obtained via a Petrov-Galerkin approach by orthogonalizing the residual $r(\mathbf{x})$ to a set of $n$ independent test (or weight) functions $w_i(\mathbf{x})$ belonging to a finite function space $\mathscr{W}$, that is:

$$\int_{\Omega} w_i(\mathbf{x})\, r(\mathbf{x})\, \mathrm{d}\Omega = 0, \qquad i = 1, \ldots, n. \tag{4.4}$$

In other words, the WRM actually projects the solution into the trial space $\mathscr{S}$ through the test space $\mathscr{W}$. For instance, if $\mathscr{W} = \mathscr{S}$, then an orthogonal projection is obtained (Galerkin method).

In the case of poroelasticity, it is common to choose the trial functions for both pressure and displacements belonging to a first-order Sobolev space:

$$\mathscr{S}_p = \left\{\tilde{p} : \Omega \rightarrow \mathbb{R} \mid \tilde{p} \in H^1, \tilde{p} = \bar{p} \text{ on } \Gamma_d^p\right\} \tag{4.5}$$

$$\mathscr{S}_u = \left\{\tilde{\mathbf{u}} : \Omega \rightarrow \mathbb{R}^3 \mid \tilde{\mathbf{u}} \in \mathbf{H}^1, \tilde{\mathbf{u}} = \bar{\mathbf{u}} \text{ on } \Gamma_d^u\right\}. \tag{4.6}$$

**Figure 4.2** – Example of test and trial functions for a 2-D unstructured grid and the associated element shape functions.

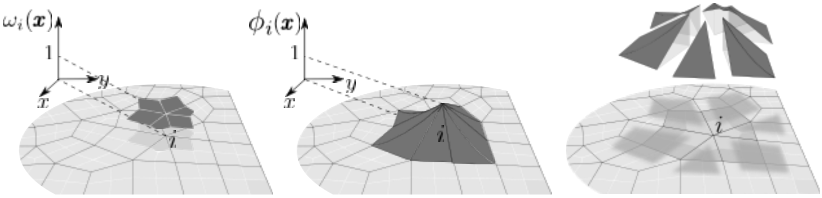

(a) Test function (b) Trial function (c) Shape functions

Source: Own authorship.

where $\Gamma_d^p$ and $\Gamma_d^u$ represent the boundaries of $\Omega$ where the pressure and displacement are prescribed to be $\bar{p}$ and $\bar{\mathbf{u}}$, respectively. Furthermore, discrete subsets $\mathscr{S}_u^h$ and $\mathscr{S}_p^h$ are of particular interest since they can be easily built based on a computational grid, as shown in Figure 4.2b, by assembling the element shape functions sharing a common vertex $i$ (Figure 4.2c). That is, a trial function can be built by:

$$\phi_i(\mathbf{x}) = \bigcup_{e \in \mathscr{E}^i} N_i^e(\mathbf{x}) \tag{4.7}$$

where $\mathscr{E}^i$ represents the set of elements sharing the same vertex $i$ and $N_i^e$ is the shape function associated to vertex $i$ of the element $e$.

### 4.1.1 Finite volume method

A variety of discretization methods is obtained by simply choosing different test functions. In order to derive a finite volume formulation from Eq. (4.4), for instance, it is convenient to partition the domain $\Omega$ into $n$ sub-domains, such that:

$$\Omega = \bigcup_{i=1}^{n} \Omega_i, \qquad \Omega_i \cap \Omega_j = \varnothing \qquad \forall \;\; j \neq i. \tag{4.8}$$

A general FVM is then obtained by setting the test functions to:

$$\omega_i(\mathbf{x}) = \begin{cases} 1, & \text{if} \;\; \mathbf{x} \in \Omega_i \\ 0, & \text{if} \;\; \mathbf{x} \notin \Omega_i \end{cases}, \qquad i = 1, \ldots, n, \tag{4.9}$$

which is depicted in Figure 4.2a for a two-dimensinoal case. As a consequence, Eq. (4.4) reduces to:

$$\int_{\Omega} \omega_i(\mathbf{x}) r(\mathbf{x})\, \mathrm{d}\Omega = \int_{\Omega_i} r(\mathbf{x})\, \mathrm{d}\Omega_i = 0, \qquad i = 1, \ldots, n \tag{4.10}$$

where the residue of the differential equation is integrated over the control volume $\Omega_i$ only, instead of the whole domain $\Omega$. It is clear that, when $\Omega_i \to 0$, i.e, $n \to \infty$, equation (4.10) ensures that $r(\mathbf{x}) = 0$ for any $\mathbf{x} \in \Omega$, hence $\tilde{u}(\mathbf{x})$ converges to the exact solution $u(\mathbf{x})$.

Equation 4.10 represents the standard procedure of the FVM for obtaining the discretized equations, i.e. the conservative form of the differential equation is integrated over each control volume of the grid. By applying the Gauss' divergence theorem to each volumetric integral, Equation 4.10 can be finally expressed as a function of the fluxes crossing the control volume's surface. The key point of this formulation is that the flux crossing a given face is exactly the same for both control volumes sharing this face, which is the reason the FVM is regarded as conservative method. One of the things that has a major impact on the flux approximations at the faces is the way the control volumes are built with respect to the computational grid. In the Element-based Finite Volume Method (EbFVM), the control volumes are built so as to provide both accuracy for the flux approximation and geometrical flexibility for the computational grid. This technique is discussed in the following section.

## 4.2 Element-based Finite Volume Method

The Element-based Finite Volume Method (EbFVM) was first proposed by Baliga (1978) and later improved by Schneider & Raw (1987). Also known as the Control Volume Finite Element Method (CVFEM), the EbFVM has attracted attention of the CFD community due to two main features: (i) it preserves the conservativeness property at each discrete control volume, which is particularly important for fluid flow problems, and (ii) the geometrical flexibility provided by the use of fully unstructured grids that can freely combine different types of elements.

As a cell-vertex method, in the EbFVM the control volumes are built around every grid node. Each element of the grid can be subdivided into

**Figure 4.3** – Control volume construction and geometrical entities.

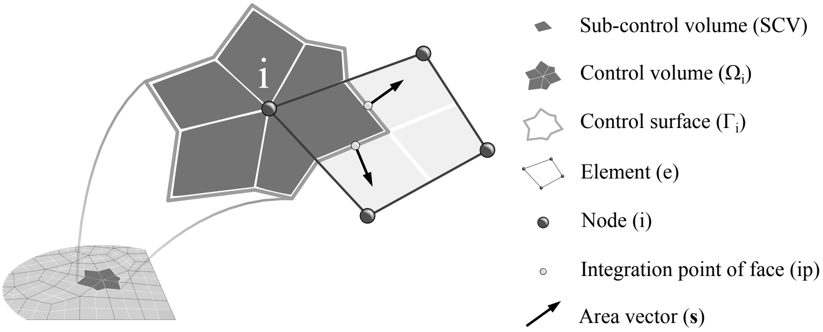

Source: Own authorship.

sub-elements, or sub-control volumes, associated to each element vertex. The control volume is then built by the union of all sub-elements sharing a common node (Figure 4.3). Every control volume $\Omega_i$ is bounded by a control surface, $\Gamma_i$, which is composed of faces identified by one integration point, *ip*, on its centroid and an area vector, **s**, pointing outwards the control volume. Since every integration point is located inside one element, all the calculations on a given face require the information associated to that element only. This "element-based" approach is also useful for building all geometrical entities, as discussed in Chapter 3. In addition, the domain is swept in an element-by-element fashion computing all fluxes in each element, which are then used to build the conservation equations for the control volumes. For a quadrilateral element, for example, Figure 4.4 illustrates the four fluxes that have to be computed by using the nodal points $A$, $B$, $C$ and $D$.

As a general rule that must be obeyed by all finite volume methods, the fluxes leaving a control volume's surface must be the same entering a neighboring control volume. Figure 4.4 shows two adjacent control volumes, $\Omega_A$ and $\Omega_B$, and the fluxes exchanged through their common faces. Computing fluxes at the faces of a control volume is the most important task to be performed by any finite volume technique. As shown in the following sections, the poroelastic equations require the evaluation of mass fluxes ($\nabla p$ and $\mathbf{u}$) and forces ($p$ and $\nabla_s \mathbf{u}$) at the integration points of the control volumes' faces. The EbFVM provides a very convenient way for evaluating these quantities by taking advantage of the shape functions

**Figure 4.4** – Fluxes crossing the faces shared by control volumes $A$ and $B$.

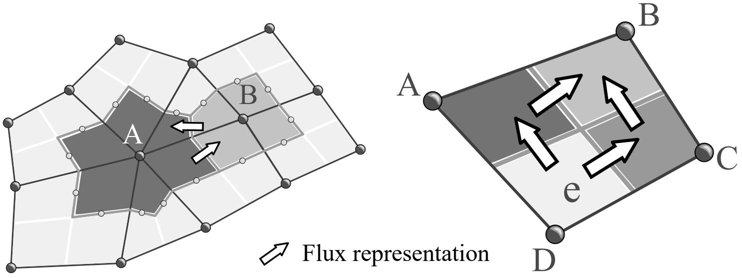

Source: Own authorship.

defined for the elements. Considering an integration point with local coordinates $\bar{\mathbf{x}}_{ip} = (\xi, \eta, \gamma)_{ip}$, for any type of element, the pressure, displacement and their gradients are evaluated as follows:

$$p\left(\bar{\mathbf{x}}_{ip}\right) \approx \mathbf{N}\left(\bar{\mathbf{x}}_{ip}\right)\mathbf{p}^e \tag{4.11}$$

$$\nabla p\left(\bar{\mathbf{x}}_{ip}\right) \approx \mathbf{B}\left(\bar{\mathbf{x}}_{ip}\right)\mathbf{p}^e \tag{4.12}$$

$$\mathbf{u}\left(\bar{\mathbf{x}}_{ip}\right) \approx \mathbf{N}_s\left(\bar{\mathbf{x}}_{ip}\right)\mathbf{u}^e \tag{4.13}$$

$$\nabla_s\mathbf{u}\left(\bar{\mathbf{x}}_{ip}\right) \approx \mathbf{B}_s\left(\bar{\mathbf{x}}_{ip}\right)\mathbf{u}^e \tag{4.14}$$

where the matrices $\mathbf{N}\left(\bar{\mathbf{x}}_{ip}\right)$, $\mathbf{N}_s\left(\bar{\mathbf{x}}_{ip}\right)$, $\mathbf{B}\left(\bar{\mathbf{x}}_{ip}\right)$ and $\mathbf{B}_s\left(\bar{\mathbf{x}}_{ip}\right)$ are all defined in Chapter 3. The pressure and displacement vectors ($\mathbf{p}^e$ and $\mathbf{u}^e$, respectively) defined for an element $e$ with $m$ vertices are represented as:

$$\mathbf{p}^e = \left[p_1 \cdots p_m\right]^T \tag{4.15}$$

$$\mathbf{u}^e = \left[u_1 \cdots u_m \quad v_1 \cdots v_m \quad w_1 \cdots w_m\right]^T \tag{4.16}$$

with the sub-indices inside brackets identifying the vertex of the element the variable is associated to and $u$, $v$ and $w$ represent the three Cartesian components of the displacement vector. Therefore, for an element $e$ with $m$ vertices, vectors $\mathbf{p}^e$ and $\mathbf{u}^e$ have dimensions $(m \times 1)$ and $(3m \times 1)$, respectively.

## 4.3 Discretized equations

The discretization procedure of a differential equation by a finite volume method begins by applying a volumetric integral over a control volume $\Omega_i$ followed by the application of the divergence theorem. Once the volumetric integrals of the divergence terms are converted into surface integrals, the mass and momentum (force) fluxes at each face of the control volume's surface have to be evaluated. In order to perform this task, the control volumes have to be built in such a way that the integration points of the control surface are located at convenient positions on the grid. In this manner, the fluxes crossing the control volumes faces can be easily computed by Equations 4.11-4.14. The detailed procedure for building the control volumes of the grid is discussed in Chapter 3, where the reader can also find some numerical aspects of the grid related to the EbFVM.

In the following subsections, the discrete representation of the stress equilibrium equations (Equation 2.25) and the mass conservation equation (Equation 2.46) is presented.

### 4.3.1 Stress equilibrium equations

The stress equilibrium equations, or the momentum equations (Equation 2.25), are integrated over a control volume $\Omega_i$ in order to obtain their discrete form, that is,

$$\int_{\Omega_i} \nabla_s \cdot \left( \mathbb{C} \nabla_s \mathbf{u} - \alpha p \mathbf{I} \right) \mathrm{d}\Omega_i + \int_{\Omega_i} \rho \mathbf{g} \mathrm{d}\Omega_i = 0 \tag{4.17}$$

Each term of the left-hand side of Equation 4.17 is separately treated below. First, the gravitational vector $\mathbf{g}$ and the density $\rho$ are assumed to be constant over the control volume, which leads to:

$$\int_{\Omega_i} \rho \mathbf{g} \mathrm{d}\Omega_i = \rho \mathbf{g} \Delta\Omega_i \tag{4.18}$$

Moreover, the divergence theorem is applied to the first volumetric integral in the left-hand side of Equation 4.17, converting it into the following surface integral:

$$\int_{\Omega_i} \nabla_s \cdot (\mathbb{C}\nabla_s \mathbf{u} - \alpha p \mathbf{I})\, \mathrm{d}\Omega_i = \int_{\Gamma_i} (\mathbb{C}\nabla_s \mathbf{u} - \alpha p \mathbf{I}) \cdot \hat{\mathbf{n}}_s\, \mathrm{d}\Gamma_i \tag{4.19}$$

with $\hat{\mathbf{n}}_s$ being the symmetric arrangement of the unit normal vector point outwards the control surface $\Gamma_i$. This special arrangement takes the form:

$$\hat{\mathbf{n}}_s^T = \begin{bmatrix} n_x & 0 & 0 & n_y & 0 & n_z \\ 0 & n_y & 0 & n_x & n_z & 0 \\ 0 & 0 & n_z & 0 & n_y & n_x \end{bmatrix}. \tag{4.20}$$

Since the control surface $\Gamma_i$, by construction, is $C^0$ continuous, the surface integral of Equation 4.19 can be split into surface integrals over each face of $\Gamma_i$. By the midpoint rule, the integrand of these surface integrals are evaluated at integration points $ip \in \Gamma_i$, so the surface integrals can be replaced by a summation over these integration points. That is,

$$\int_{\Gamma_i} (\mathbb{C}\nabla_s \mathbf{u} - \alpha p \mathbf{I}) \cdot \hat{\mathbf{n}}_s\, \mathrm{d}\Gamma_i \approx \sum_{\mathrm{ip}\in\Gamma_i} \left[(\mathbb{C}\nabla_s \mathbf{u} - \alpha p \mathbf{I}) \cdot \mathbf{s}_s\right]_{\mathrm{ip}}, \tag{4.21}$$

where the symmetric area vector is defined as $\mathbf{s}_s = \hat{\mathbf{n}}_s \Delta s$, with $\Delta s$ being the area of the face.

Now, Equations 4.21 and 4.18 are substituted into Equation 4.17, yielding to:

$$\sum_{\mathrm{ip}\in\Gamma_i} \left[(\mathbb{C}\nabla_s \mathbf{u} - \alpha p \mathbf{I}) \cdot \mathbf{s}_s\right]_{\mathrm{ip}} = \mathbf{b}_i^{\mathbf{u}} \tag{4.22}$$

where the source term reads $\mathbf{b}_i^{\mathbf{u}} = -\rho \mathbf{g} \Delta\Omega_i$. It should be noticed that the constitutive matrix $\mathbb{C}$ has to be evaluated at the integration point, where the effective stresses are required. It is a common practice in the EbFVM, however, to define a constitutive matrix for each element of the grid, such as $\mathbb{C}_{ip} = \mathbb{C}^e$, with $e$ being the element containing the integration point *ip*. Still on Equation 4.22, one can notice that,

$$(p\mathbf{I})_{\mathrm{ip}} = \begin{bmatrix} p_{\mathrm{ip}} & p_{\mathrm{ip}} & p_{\mathrm{ip}} & 0 & 0 & 0 \end{bmatrix}^T. \tag{4.23}$$

But, according to Equation 4.11, $p_{\mathrm{ip}} \approx \mathbf{N}\left(\bar{\mathbf{x}}_{\mathrm{ip}}\right) \mathbf{p}^e$, so we can define another matrix $\mathbf{N_i}$ such that,

$$(p\mathbf{I})_{\text{ip}} = \begin{bmatrix}\mathbf{N}^T & \mathbf{N}^T & \mathbf{N}^T & 0 & 0 & 0\end{bmatrix}^T \mathbf{p}^e = \mathbf{N_i}\mathbf{p}^e \tag{4.24}$$

where it can be verified that the dimension of $\mathbf{N_i}$ is $(6 \times m)$ with $m$ being the number of vertices of the element $e$ containing the integration point *ip*. In addition, the symmetric gradient of the displacement vector in Equation 4.17 is evaluated by Equation 4.14. The dot product in Equation 4.22 can also be reinterpreted as a matrix product, which leads to:

$$\sum_{\text{ip}\in\Gamma_i} \left[\mathbf{s}_s^T \left(\mathbb{C}\mathbf{B}_s\mathbf{u}^e - \alpha\mathbf{N_i}\mathbf{p}^e\right)\right]_{\text{ip}} = \mathbf{b}_i^{\mathbf{u}} \tag{4.25}$$

Finally, by the defining the matrices below:

$$\mathbf{M}_{\text{ip}} = \left(\mathbf{s}_s^T\mathbb{C}\mathbf{B}_s\right)_{\text{ip}} \qquad \text{and} \qquad \mathbf{L}_{\text{ip}} = \left(\alpha\mathbf{s}_s^T\mathbf{N_i}\right)_{\text{ip}} \tag{4.26}$$

the discretized equilibrium equations can be written in a compact form, such as:

$$\sum_{\text{ip}\in\Gamma_i} \left(\mathbf{M}_{\text{ip}}\mathbf{u}^e - \mathbf{L}_{\text{ip}}\mathbf{p}^e\right) = \mathbf{b}_i^{\mathbf{u}} \tag{4.27}$$

Equation 4.27 unfolds into three equations, each representing the balance of forces acting on the control volume $\Omega_i$ in one of the three coordinate directions. The vectors $\mathbf{u}^e$ and $\mathbf{p}^e$ represent the displacement and pressure unknowns stored at the vertices of element $e$, that is, the nodes of the grid. It is important to have in mind that, when the summation is performed over all the integration points belonging to $\Gamma_i$, the element $e$ always refer to the element that contains the current integration point. In other words, the superscript $e$ in Equation 4.27 refers to the set of elements sharing the same vertex $i$.

### 4.3.2 Mass conservation equation

Given that $\alpha$ and $M$ are time independent, the global mass conservation equation can be conveniently written as:

$$\frac{\partial}{\partial t}\left(\frac{p}{M} + \alpha\nabla\cdot\mathbf{u}\right) + \nabla\cdot\mathbf{v} = q. \tag{4.28}$$

Since Equation 4.28 also time dependent, the time interval $I = \left]0, T\right]$ is subdivided into sub-intervals of size $\Delta t$. In this manner, Equation 4.28 can be integrated between a given time $t$ and $t+\Delta t$,

$$\int_t^{t+\Delta t} \frac{\partial}{\partial t}\left(\frac{p}{M}+\alpha\nabla\cdot\mathbf{u}\right)\mathrm{d}t+\int_t^{t+\Delta t}\nabla\cdot\mathbf{v}\,\mathrm{d}t=\int_t^{t+\Delta t} q\,\mathrm{d}t. \tag{4.29}$$

The fundamental theorem of calculus and an implicit first-order accurate backward Euler scheme is applied to Equation 4.29, and after a few manipulations the following expression is obtained:

$$\frac{1}{M}\frac{p-p^o}{\Delta t}+\nabla\cdot\left[\mathbf{v}+\frac{\alpha}{\Delta t}\left(\mathbf{u}-\mathbf{u}^o\right)\right]=q \tag{4.30}$$

where superscript $o$ indicates the variables evaluated at the previous time step $t$. When variables are evaluated at $t+\Delta t$, no superscript is used. Now, Equation 4.30 is integrate over the control volume $\Omega_i$, the divergence theorem is applied along with the midpoint rule, which leads to:

$$\frac{\Delta\Omega_i}{M\Delta t}\left(p_i-p_i^o\right)+\sum_{\mathrm{ip}\in\Gamma_i}\left[\mathbf{v}_{\mathrm{ip}}+\frac{\alpha}{\Delta t}\left(\mathbf{u}_{\mathrm{ip}}-\mathbf{u}_{\mathrm{ip}}^o\right)\right]\cdot\mathbf{s}_{\mathrm{ip}}=q_i\Delta\Omega_i, \tag{4.31}$$

with $q_i$ indicating that the source term is evaluated at node $i$ (or $\Omega_i$). In Equation 4.31, the total volumetric flux crossing the integration point *ip* is composed of two contributions: one of them due to Darcy's velocity ($\dot{\omega}_{\mathrm{ip}}$) and another one due to the solid velocity ($\dot{\omega}_{\mathrm{ip}}^s$). These two contributions are recognized as:

$$\dot{\omega}_{\mathrm{ip}}=\mathbf{v}_{\mathrm{ip}}\cdot\mathbf{s}_{\mathrm{ip}}=-\frac{\mathbf{K}^e}{\mu}\cdot\left(\nabla p-\rho_f\mathbf{g}\right)_{\mathrm{ip}}\cdot\mathbf{s}_{\mathrm{ip}} \tag{4.32}$$

and

$$\dot{\omega}_{\mathrm{ip}}^s=\mathbf{v}^s\cdot\mathbf{s}_{\mathrm{ip}}=\frac{\alpha}{\Delta t}\left(\mathbf{u}-\mathbf{u}^o\right)_{\mathrm{ip}}\cdot\mathbf{s}_{\mathrm{ip}}. \tag{4.33}$$

These two volumetric fluxes can be approximated at the integration by employing Equations 4.12 and 4.13,

$$\dot{\omega}_{\mathrm{ip}}=\rho_f\mathbf{G}_{\mathrm{ip}}\mathbf{g}-\mathbf{H}_{\mathrm{ip}}\mathbf{p}^e \tag{4.34}$$

$$\dot{\omega}_{\mathrm{ip}}^s=\frac{\mathbf{Q}_{\mathrm{ip}}}{\Delta t}\left[\mathbf{u}^e-\left(\mathbf{u}^e\right)^o\right] \tag{4.35}$$

where the matrices $\mathbf{G}_{\text{ip}}$, $\mathbf{H}_{\text{ip}}$ and $\mathbf{Q}_{\text{ip}}$ are defined as:

$$\mathbf{G}_{\text{ip}} = \frac{1}{\mu}\mathbf{s}_{\text{ip}}^{T}\mathbf{K}^{e} \tag{4.36}$$

$$\mathbf{H}_{\text{ip}} = \mathbf{G}_{\text{ip}}\mathbf{B}_{\text{ip}} \tag{4.37}$$

$$\mathbf{Q}_{\text{ip}} = \alpha\mathbf{s}_{\text{ip}}^{T}\left(\mathbf{N}_{\text{s}}\right)_{\text{ip}} \tag{4.38}$$

It is important to highlight that the volumetric fluxes represented in Equations 4.34 and 4.35 are written in terms of the nodal values $\mathbf{p}^{e}$ and $\mathbf{u}^{e}$, as desired. Finally, the discretized mass conservation equation for single-phase flows in deformable porous media is obtained by substituting Equations 4.34 and 4.35 into Equation 4.31. After rearranging the terms, the following expression is obtained:

$$\frac{\Delta\Omega_i}{M\Delta t}p_i + \sum_{\text{ip}\in\Gamma_i}\left(\frac{1}{\Delta t}\mathbf{Q}_{\text{ip}}\mathbf{u}^{e} - \mathbf{H}_{\text{ip}}\mathbf{p}^{e}\right) = b_i^{p}, \tag{4.39}$$

where the independent term, in the right-hand side, contains the source term, the gravitational term and the known values of pressure and displacement from the previous time step, that is:

$$b_i^{p} = q_i\Delta\Omega_i + \frac{\Delta\Omega_i}{M\Delta t}p_i^{o} + \sum_{\text{ip}\in\Gamma_i}\left[\frac{1}{\Delta t}\mathbf{Q}_{\text{ip}}\left(\mathbf{u}^{e}\right)^{o} - \rho_f\mathbf{G}_{\text{ip}}\mathbf{g}\right]. \tag{4.40}$$

### 4.3.3 Linear system assembling

The discretized mass and momentum conservation equations (Equations 4.27 and 4.39, respectively) are built for every control volume (node) $i$ of the grid. When grouped together these equations compose a linear system of the following form:

$$\begin{bmatrix} \dfrac{\mathbb{A}}{\Delta t} - \mathbb{H} & \dfrac{\mathbb{Q}}{\Delta t} \\ \mathbb{L} & -\mathbb{M} \end{bmatrix} \begin{bmatrix} \mathbf{p} \\ \mathbf{u} \end{bmatrix} = \begin{bmatrix} \mathbf{b}^{p} \\ \mathbf{b}^{u} \end{bmatrix}, \tag{4.41}$$

which is a $(4n \times 4n)$ system, with $n$ being the number of nodes of the grid. In this case, $\mathbb{A}$ is a $(n \times n)$ diagonal matrix with entries $a_{ii} = \Delta\Omega_i / M$ from the transient terms. Matrix $\mathbb{H}$ has the same dimension as $\mathbb{A}$ and it represents the mass fluxes due to the fluid velocities. Matrices $\mathbb{Q}$ and $\mathbb{L}$ are the coupling matrices that represent the volumetric strain and pressure gradient terms. The stiffness matrix $\mathbb{M}$ is a $(3n \times 3n)$ matrix which represents the balance of forces in the three coordinate directions. It is also helpful to recognize that matrices $\mathbb{H}$, $\mathbb{Q}$, $\mathbb{L}$ and $\mathbb{M}$ are composed by assembling the contributions of $\mathbf{H}_{\text{ip}}$, $\mathbf{Q}_{\text{ip}}$, $\mathbf{L}_{\text{ip}}$ and $\mathbf{M}_{\text{ip}}$, respectively, for all integration points belonging to the grid. Finally, vectors $\mathbf{b}^p$ and $\mathbf{b}^u$ are the right-hand side of mass and stress equilibrium equations, respectively.

CHAPTER

# 5

# STABILIZED FORMULATION

In this chapter the stabilization technique proposed in this thesis is presented for one and three-dimensional elements. A discussion on the mathematical aspects of numerical instabilities in geomechanics is performed and a review of the main strategies proposed for solving this problem is presented. In the sequence, the similarities between geomechanics and general fluid flows are identified in order to prepare the ground for presenting the Physical Influence Scheme (PIS) as an alternative strategy for treating numerical instabilities in poroelasticity.

## 5.1 Stabilization techniques

The trial functions belonging to $\mathscr{S}_p^h$ and $\mathscr{S}_u^h$ for solving Biot's consolidation model is an attractive choice as it provides at least second-order approximations for both pressure and displacement fields. However, as it does not satisfy the LBB-condition (Babuška, 1971; Brezzi, 1974), this pair of approximations may lead to oscillatory solutions in the limit of undrained conditions. For this reason, several authors choose elements that provide interpolation functions one order higher for the displacements than those of pressure (Murad & Loula, 1994; Reed, 1984), thus satisfying the LBB-condition. Other researchers, by distinction, developed mixed formulations (Ferronato *et al.*, 2010; Phillips & Wheeler, 2007a,b; Tchonkova *et al.*, 2008). Ferronato *et al.* (2010) and Castelletto *et al.* (2016), for instance, used the lowest order Raviart–Thomas interpolation for pressure and fluxes and a linear or trilinear interpolation for displacements, thus keeping the advantage of using simple elements. They show that the oscillatory pressure field is successfully mitigated, but the increase of the number of unknowns is a serious issue and requires the development of ad hoc preconditioners for solving the resulting linear systems.

In order to avoid such drawbacks, several stabilization techniques were developed to allow for the use of equal-order interpolation pairs for both pressure and displacement fields. Basically, most of such techniques consist of introducing stabilization terms into the mass balance equation in order to compensate, at some degree, the inability at satisfying the LBB-requirements. The way these terms are obtained may differ according to the selected approach. For instance, Truty & Zimmermann (2006) computed a stabilization term based on the minimum time step criterion of Vermeer & Verruijt (1981), which they called FPL (Fluid Pressure Laplacian). White & Borja (2008) have used the concept of Polynomial-Pressure-Projection in order to derive a stable formulation for solving poromechanics in double-porosity media. Another stabilization method, called Finite Increment Calculus (FIC), was developed by Oñate (1998) in the context of advective-diffusive transport and fluid flow problems. This technique was also employed for solving incompressible solids (Oñate *et al.*, 2004) and poroelastic media (Preisig & Prèvost, 2011). More recently, Rodrigo *et al.* (2016) have advanced a stabilization technique for P1-P1 elements. Although these stabilization strategies are not exhaustive, they represent the efforts for providing stable solutions for poroelasticity problems in the finite element context.

The finite volume formulation proposed in this work also employ equal-order approximations for pressure and displacements (see Equations 4.5 and 4.6), thus numerical instabilities are also expected to be observed in critical situations. In order to avoid such instabilities, the proposed strategy consists of employing the so-called Physical Influence Scheme (PIS), developed by Schneider & Raw (1987), for evaluating the face displacements[1] in the mass conservation equation. The basic idea of PIS relies on introducing a modification to the discretized governing equations by properly evaluating the nodal displacements at the faces of

---

[1] The face displacements refer to the displacement vector evaluated at the integration point of a face.

the control volumes, where they are required for computing the volumetric strains. This technique was originally advanced for solving incompressible flows of Newtonian fluids governed by the continuity equation and the Navier-Stokes equations. In this case, much like what happens in poroelasticity, a pathologic oscillatory behavior of the pressure solution is experienced when all variables are collocated, i.e., when the control volume is the same for both pressure and velocities. The idea of using the Physical Influence Scheme in this work is based on the similarities between the pressure-velocity coupling in general fluid flows[2] (not in porous media) and the pressure-displacement coupling encountered in geomechanics. In the next section these similarities are discussed.

## 5.2 Coupling similarities

The coupling between pressure and displacement in poromechanics is similar to the one between pressure and velocities observed in the Navier-Stokes equations for general flows. In the latter case, the velocity field is required to satisfy mass and momentum conservation. This task cannot be accomplished if a finite volume technique with a collocated arrangement of variables is used, since the discretized continuity equation requires velocities at the cell faces (integration points), where they are not directly available. At this point, a special interpolation function must be devised in order to properly evaluate such velocities. This is precisely what PIS is responsible for. It is well established that performing a simple average of the adjacent velocities results in an inaccurate velocity field and an oscillatory pressure field (Patankar, 1980). A proper evaluation of the face velocities is the key point for avoiding the oscillating pressure pathology when solving the Navier-Stokes equations by a finite volume method with collocated variables. It has been shown by a number of researchers (Majumdar, 1986; Marchi & Maliska, 1994; Peric, 1985; Rhie & Chow, 1983; Schneider & Raw, 1987) that the inclusion of pressure effects in the evaluation of the face velocities is very important for avoiding such problems.

In the poroelastic case, although the pathology is similar to the one in general fluid flows, the mass conservation equation presents some details

---

[2] The term "general fluid flow" refers to all types of flows governed by the Navier-Stokes equations. It will be used henceforth to make a distinction from fluid flows in porous media.

that deserve further attention. Recall the mass conservation equation for deformable porous media (Equation 2.46):

$$\frac{1}{M}\frac{\partial p}{\partial t} + \nabla \cdot (\mathbf{v} + \alpha \mathbf{v}^s) = 0 \tag{5.1}$$

where the source term $q$ has been disregarded. By its turn, considering an ideal gas with density $\rho$ and specific gas constant $R$, the mass conservation equation for isothermal compressible flow can be written as:

$$\frac{1}{RT}\frac{\partial p}{\partial t} + \nabla \cdot (\rho \mathbf{v}) = 0 \tag{5.2}$$

with $T$ being the temperature and $\mathbf{v}$ the fluid velocity vector, which is also present in the Navier-Stokes equations.

The main difference between Equations 5.1 and 5.2 is that, whereas only the fluid velocity $\mathbf{v}$ appears in the latter equation, the velocity responsible for satisfying mass conservation for the deformable porous medium is composed of two contributions: namely the Darcy velocity, $\mathbf{v}$, and the solid velocity, $\mathbf{v}^s$. After the discretization, both velocities have to be computed at the cell faces (integration points). The fluid velocity in Equation 5.1 is proportional to the pressure gradient through Darcy's law, so it can be easily computed by the shape function derivatives (matrix $\mathbf{B}_{ip}$). The solid velocity, on the other hand, is given by the time derivative of the displacement vector, which can be approximated at the integration point by the following expression:

$$\mathbf{v}^s_{\text{ip}} = \left.\frac{\partial \mathbf{u}}{\partial t}\right|_{ip} \approx \frac{\mathbf{u}_{\text{ip}} - \mathbf{u}^o_{\text{ip}}}{\Delta t}, \tag{5.3}$$

from where it becomes clear that the displacement vectors are required at the integration points ($\mathbf{u}_{ip}$ and $\mathbf{u}^o_{ip}$). In Equation 4.33, the element shape functions were employed to approximate the solid velocity, as already indicated in Equation 4.14. However, similarly to what happens in general flow problems, where the velocity vector itself must be evaluated at the integration points, the use of the element shape functions does not provide the necessary stability for the solution (Schneider & Raw, 1987).

By contrast, it is important to observe that a poor approximation of the displacements at integration points (e.g. by using the element shape functions) does not necessarily imply an inaccurate solution of equation 5.1, since $\mathbf{v}^s$ is usually a small contribution compared to $\mathbf{v}$. The problem arises during undrained consolidation, where the Darcy velocity is nearly zero. In this situation the solid velocity $\mathbf{v}^s$ is totally responsible for satisfying the mass conservation and a condition similar to Equation 5.2 is restored. In this case, a full analogy between pressure-displacement and pressure-velocity coupling can be established. The natural conclusion that comes from this analogy is that the same techniques already advanced for avoiding pressure instabilities in the Navier-Stokes equations can also be applied in poromechanics, as the source of these instabilities is the same for both types of problems.

## 5.3 The Physical Influence Scheme

Suppose the values of a general scalar field, $\Phi$, are known only at two nodal points $A$ and $B$, as illustrated in Figure 5.1. If the value of this scalar field is required, for some reason, at a position $i$ between the two nodal points, then a profile of variation of $\Phi$ between $A$ and $B$ must be assumed in order to compute $\Phi_i$. In other words, an interpolation function must be chosen so $\Phi_i$ can be represented as a function of $\Phi_A$ and $\Phi_B$. When the scalar field comes from a physical phenomenon it is reasonable to expected the value of $\Phi_i$ to be affected by the physics occurring between points $A$ and $B$. From this viewpoint, it would be logical to try to include these effects into the profile of variation of $\Phi_i$, i. e., the interpolation function of $\Phi_i$. As it turns out, the differential governing equation naturally balances these effects, so it could be used as a base for obtaining such an interpolation function. This is precisely the underlying idea behind the Physical Influence Scheme.

**Figure 5.1** – A scalar field stored at nodal points $A$ and $B$ is interpolated to position $i$ considering diffusion and advective effects.

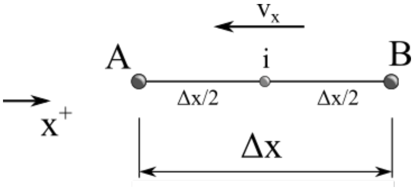

Source: Own authorship.

The procedure for obtaining the interpolation function then consists of evaluating the governing differential equation at the desired position, where the scalar is to be interpolated. Suppose, for example, the value of $\Phi$ is to be interpolated at position $i$ of Figure 5.1 as a function of $\Phi_A$ and $\Phi_B$. If one-dimensional diffusion is the only physical phenomenon governing $\Phi$, then an interpolation function can be devised at position $i$ as follows:

$$\Gamma \left.\frac{d^2\Phi}{dx^2}\right|_i \approx \frac{\Gamma}{\Delta x^2}\left(\Phi_A - 2\Phi_i + \Phi_B\right) = 0 \qquad \therefore \qquad \Phi_i = \frac{\Phi_A + \Phi_B}{2}, \tag{5.4}$$

where $\Gamma$ is the diffusivity. Equation 5.4 is a reasonable approximation since diffusion has an elliptic nature, so the value of $\Phi_i$ should be equally influenced by $\Phi_A$ and $\Phi_B$.

However, if advection also plays a role in the process, then the value of $\Phi_i$ would be computed as:

$$\rho v_x \left.\frac{d\Phi}{dx}\right|_i - \Gamma \left.\frac{d^2\Phi}{dx^2}\right|_i \approx \frac{\rho v_x}{\Delta x}\left(\Phi_i - \Phi_u\right) - \frac{\Gamma}{\Delta x^2}\left(\Phi_A - 2\Phi_i + \Phi_B\right) = 0 \tag{5.5}$$

where $\rho$ is the density and $v_x$ is the velocity in the $x$ direction. For the $v_x$ pointing to the left, as depicted in Figure 5.1, the upstream value $\Phi_u$ would be equal to $\Phi_B$. In this case, the interpolated value would be:

$$\Phi_i = \left(\frac{2\Gamma}{\Delta x^2} + \frac{\rho v_x}{\Delta x}\right)^{-1} \left[\frac{\Gamma}{\Delta x^2}\Phi_A + \left(\frac{\Gamma}{\Delta x^2} + \frac{\rho v_x}{\Delta x}\right)\Phi_B\right]. \tag{5.6}$$

It can be noticed that Equation 5.6 reduces to Equation 5.4 if $v_x = 0$. On the other hand, the bigger the velocity the bigger the influence of $\Phi_B$ on the value of $\Phi_i$, that is, the advection effects become predominant.

For solving general fluid flows, Schneider & Raw (1987) derived an interpolation function based on the momentum differential equations (Navier-Stokes equations) evaluated at the integration points of the control volumes. In their work, special attention was dedicated in properly evaluating the advective and diffusive terms. Nevertheless, the authors emphasized the importance of keeping the pressure term from the Navier-Stokes equations in the interpolation function. In the present work, the very same procedure is applied to obtain an interpolation function for computing the displacement vector at the integration points. The momentum equation, in this case, is slightly different and a complete description of this methodology is described in the following sections.

### 5.3.1 One-dimensional analysis

In order to elucidate how PIS operates, a one-dimensional case is first described. Figure 5.2 represents a 1-D domain, uniformly discretized in two linear elements of length $\Delta x$ each. The control volume centered at node $P$ has unitary cross-section area, and the nodal pressure and displacements are stored at nodes $W$, $P$, $E$ and $EE$. It has been shown that, during the discretization process, the displacements are also required to be computed at the control volume faces, $w$ and $e$, in order to account for the solid velocities. A general expression for evaluating $u_e$, for example, can be obtained by using Taylor series to perform a backward and a forward expansion around face $e$ up to the quadratic terms, that is,

$$u_E \approx u_e + \frac{\Delta x}{2}\frac{\partial u}{\partial x}\bigg|_e + \frac{\Delta x^2}{8}\frac{\partial^2 u}{\partial x^2}\bigg|_e \tag{5.7}$$

$$u_P \approx u_e - \frac{\Delta x}{2}\frac{\partial u}{\partial x}\bigg|_e + \frac{\Delta x^2}{8}\frac{\partial^2 u}{\partial x^2}\bigg|_e \tag{5.8}$$

By adding Equations 5.7 and 5.8, the first derivatives of $u$ cancel each other and $u_e$ can be isolated, leading to:

$$u_e \approx \frac{u_E + u_P}{2} - \frac{\Delta x^2}{8}\frac{\partial^2 u}{\partial x^2}\bigg|_e . \tag{5.9}$$

If the second derivative in Equation 5.9 is dropped, then a second-order accurate central differencing scheme is resembled. This is the same result that would have been obtained by evaluating $u_e$ through the linear

**Figure 5.2** – One-dimensional control volume on node $P$.

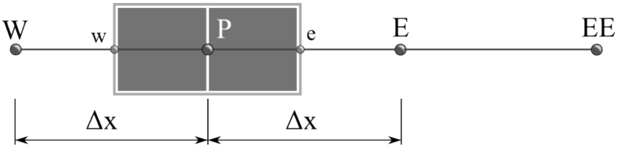

Source: Own authorship.

shape functions associated to the element between nodes $P$ and $E$. If a higher order approximation is desired for Equation 5.9, the second derivative of $u$ cannot be neglected. Approximating this second derivative with points $u_e$, $u_E$ and $u_P$ only, as in Equation 5.4, would reduce Equation 5.9 to a linear (second order) approximation again, which is not the goal. An alternative could be to involve also points $W$ and $EE$ to approximate the second derivative, but this procedure would increase the complexity of the formulation specially for three-dimensional problems.

The Physical Influence Scheme provides a very convenient way for computing the quadratic term in Equation 5.9 without increasing the stencil, i.e., without involving extra nodal points. The idea consists of evaluating the 1-D stress equilibrium equation (see Equation 2.27) at the integration point of face $e$, that is,

$$(\lambda+2G)\left.\frac{\partial^2 u}{\partial x^2}\right|_e = \alpha\left.\frac{\partial p}{\partial x}\right|_e \quad \rightarrow \quad \left.\frac{\partial^2 u}{\partial x^2}\right|_e = \frac{\alpha}{(\lambda+2G)}\left.\frac{\partial p}{\partial x}\right|_e. \tag{5.10}$$

Equation 5.10 tells that the second derivative of displacement is proportional to the first derivative of pressure. Therefore, instead of computing the second derivative of displacement, one can simply approximate the first derivative of pressure at the integration point, which is particularly interesting as it only requires nodal points $P$ and $E$, as initially desired. The pressure derivative can be approximated by a central differencing scheme, or equivalently by using the element shape function derivatives, which yields to:

$$\left.\frac{\partial^2 u}{\partial x^2}\right|_e \approx \frac{\alpha}{(\lambda+2G)}\frac{(p_E-p_P)}{\Delta x}. \tag{5.11}$$

Finally, substitution of Equation 5.11 into Equation 5.9 provides the following expression for the face displacement:

$$u_e \approx \frac{u_E+u_P}{2} - \frac{\alpha\Delta x}{8(\lambda+2G)}(p_E-p_P) \tag{5.12}$$

The pressure term in Equation 5.12 provides a third-order accurate approximation for the face displacements. In this manner, the Physical Influence Scheme can be regarded as way of mimicking a higher order approximation for the displacements in the mass conservation equation, which is a necessary condition for obtaining stable solutions (Babuška, 1971; Brezzi, 1974). It is important to emphasize, however, that the displacement approximations are still of second order in the stress equilibrium equations, as it can be verified in convergence tests presented in the next chapter.

From a physical perspective, the ability of providing better approximations through Equation 5.12 can be grasped by considering two extreme situations at face $e$ of Figure 5.2. The first one occurs in the absence of pressure gradient at this face ($p_P = p_E$), in which the same result would be obtained by Equation 5.12 or Equation 5.9 with the quadratic term dropped. However, if the nodal displacements are arbitrarily set to zero ($u_P = u_E = 0$) and a strong (just for the sake of imagination) pressure gradient is acting on face $e$ ($p_P >> p_E$, for example), it would be perfectly reasonable to expect a non-zero displacement to occur at face $e$. This behavior is correctly captured by Equation 5.12, whereas Equation 5.9 with the quadratic term dropped would result a zero displacement at face $e$, which is a serious inconsistency. These examples illustrates the importance of including the physical effects into the interpolation function in order to obtain reliable and consistent approximations.

## 5.3.2 Three-dimensional formulation

The same idea can be extended to three-dimensional problems. In this case, an equivalent but slightly different procedure is adopted for obtaining the expression for the face displacements. For this purpose, consider the three-dimensional stress equilibrium equations (Equation 2.27) and assume no body forces. In addition, the term $(\lambda + G)\nabla(\nabla \cdot \mathbf{u})$ is neglected, since it is a reasonable approximation in some geomechanical applications Ferronato *et al.* (2006). The resulting differential equation is then evaluated at the integration point *ip*:

$$G\nabla^2 \mathbf{u}_{\text{ip}} = \alpha \nabla p_{\text{ip}}. \tag{5.13}$$

As suggested by Schneider & Raw (1987), and also shown in section 5.5 for a three-dimensional element, the Laplacian term of Equation 5.13 can be approximated as:

$$\nabla^2 \mathbf{u}_{\text{ip}} \approx \frac{1}{L_d^2}\left[(\mathbf{N}_s)_{\text{ip}}\,\mathbf{u}^e - \mathbf{u}_{\text{ip}}\right], \tag{5.14}$$

where $(\mathbf{N}_s)_{\text{ip}}$ is the symmetric arrangement of the shape function derivatives evaluated at the integration point (see Equation 3.8), and the diffusive length $L_d$ has to be properly defined such that a second-order approximation is obtained for each type of element (see section 5.5).

The pressure gradient on the right-hand side of Equation 5.13 is readily evaluated by the element shape functions stored at matrix **B** of Equation 3.26. Thereby,

$$\nabla p_{\text{ip}} \approx \mathbf{B}_{\text{ip}} \mathbf{p}^e. \tag{5.15}$$

Finally, substitution of Equations 5.14 and 5.15 into Equation 5.13 and isolating $\mathbf{u}_{\text{ip}}$ leads to the following interpolation function for the face displacement vector:

$$\mathbf{u}_{\text{ip}} \approx (\mathbf{N}_s)_{\text{ip}} \mathbf{u}^e - \frac{\alpha L_d^2}{G} \mathbf{B}_{\text{ip}} \mathbf{p}^e \tag{5.16}$$

It can be easily verified that the same discussion held in the last paragraph of the previous subsection is totally valid for equation 5.16. That is, both Equations 5.16 and 5.12 correctly captures the influence of the pressure gradient on the displacement $\mathbf{u}_{\text{ip}}$ by means of the momentum equations (stress equilibrium equations). Evidently, Equation 5.16 also reduces to a second-order approximation in the absence of pressure gradients. However, although this argument is also valid for the three-dimensional case, Equation 5.16 cannot be regarded as a third-order approximation, as Equation 5.12 does, because the term $(\lambda + G)\nabla(\nabla \cdot \mathbf{u})$ has been neglected from the stress equilibrium equations. Therefore, Equation 5.16 may lie somewhere in between second and third-order approximation for the displacement vector at the integration points.

In order to compute the solid velocity in Equation 5.3, the displacement vector at the previous time step has to be evaluated as well. This is done substituting $(\mathbf{u}^e)^o$ and $(\mathbf{p}^e)^o$ into Equation 5.16, that is:

$$\mathbf{u}_{\text{ip}}^o \approx (\mathbf{N}_s)_{\text{ip}} (\mathbf{u}^e)^o - \frac{\alpha L_d^2}{G} \mathbf{B}_{\text{ip}} (\mathbf{p}^e)^o. \tag{5.17}$$

Finally, substitution of Equations 5.16 and 5.17 into Equation 5.3 leads to the following expression for computing the solid velocity at the integration points:

$$\mathbf{v}^s_{\mathrm{ip}} = \frac{\alpha}{\Delta t}(\mathbf{N}_s)_{\mathrm{ip}}\left[\mathbf{u}^e - (\mathbf{u}^e)^o\right] - \frac{\alpha^2 L_d^2}{\Delta t G}\mathbf{B}_{\mathrm{ip}}\left[\mathbf{p}^e - (\mathbf{p}^e)^o\right] \tag{5.18}$$

It is interesting to notice that the solid velocity in Equation 5.18 also depends on the rate of pressure gradient, represented by the second term in the right-hand side of these equation. Therefore, abrupt changes in the pressure gradient field as time passes will greatly affect the solid velocity vector. On the other hand, Equation 5.18 tells that, even in the presence of sharp pressure gradient fields, if a steady state condition is reached for pressure, then the solid velocity depends only on the displacement vectors.

## 5.4 Stabilized mass conservation equation

Considering the solid velocity in Equation 5.3, Equation 4.31 can be written as follows:

$$\frac{\Delta\Omega_i}{M\Delta t}\left(p_i - p_i^o\right) + \sum_{\mathrm{ip}\in\Gamma_i}\left(\mathbf{v}_{\mathrm{ip}} + \alpha\mathbf{v}^s_{\mathrm{ip}}\right)\cdot\mathbf{s}_{\mathrm{ip}} = q_i\Delta\Omega_i. \tag{5.19}$$

Before substitute velocities $\mathbf{v}_{\mathrm{ip}}$ and $\mathbf{v}^s_{\mathrm{ip}}$ into Equation 5.19, it is convenient, for specific purposes, to define a mobility[3] tensor as:

$$\boldsymbol{\lambda} = \frac{\mathbf{K}}{\mu}, \tag{5.20}$$

and a pseudo-mobility tensor as follows:

$$\tilde{\boldsymbol{\lambda}} = \frac{\alpha^2 L_d^2}{\Delta t G}\mathbf{I}, \tag{5.21}$$

with **I**, in this case, representing a second-order identity tensor (not in Voigt notation). For the sake of completeness, the numerical approximation of Darcy's velocity at the integration point is given by the follow expression:

---

[3] Traditionally, mobility is defined as the ratio between the relative permeability and viscosity, which results in a scalar quantity. However, given our purposes, we intentionally apply this concept to the absolute permeability tensor as the idea of fluid mobility through the pore channels also applies for single-phase flows.

$$\mathbf{v}_{\text{ip}} = -\boldsymbol{\lambda}^e \left(\nabla p_{\text{ip}} - \rho_f \mathbf{g}\right) \approx -\boldsymbol{\lambda}^e \mathbf{B}_{\text{ip}} \mathbf{p}^e + \rho_f \boldsymbol{\lambda}^e \mathbf{g} \tag{5.22}$$

At this point, velocities $\mathbf{v}_{\text{ip}}$ and $\mathbf{v}^s_{\text{ip}}$ are replaced in Equation 5.19 by Equations 5.22 and 5.18, respectively. By considering definitions 5.20 and 5.21, the resulting discretized mass conservation equations reads:

$$\frac{\Delta\Omega_i}{M\Delta t} p_i - \sum_{\text{ip}\in\Gamma_i} \left[ \mathbf{s}^T_{\text{ip}} \left(\boldsymbol{\lambda}^e + \tilde{\boldsymbol{\lambda}}_{\text{ip}}\right) \mathbf{B}_{\text{ip}} \mathbf{p}^e - \frac{\alpha}{\Delta t} \mathbf{s}^T_{\text{ip}} \left(\mathbf{N}_{\text{s}}\right)_{\text{ip}} \mathbf{u}^e \right] = b^p_i + \tilde{b}^p_i, \tag{5.23}$$

where $b^p_i$ is given by Equation 4.40 and the additional term in the right-hand side is:

$$\tilde{b}^p_i = -\sum_{\text{ip}\in\Gamma_i} \left[ \mathbf{s}^T_{\text{ip}} \tilde{\boldsymbol{\lambda}}_{\text{ip}} \mathbf{B}_{\text{ip}} \left(\mathbf{p}^e\right)^o \right]. \tag{5.24}$$

It is important to notice the pseudo-mobility tensor, $\tilde{\boldsymbol{\lambda}}_{\text{ip}}$, in Equations 5.23 and 5.24 carries the subscript *ip* to indicate it is computed at a given integration point. The reason for this is because the diffusive length may vary from one integration point to another, even if they belong to the same element. In addition, the superscript *e* is suppressed from $\tilde{\boldsymbol{\lambda}}_{\text{ip}}$ because it is implicit the element it refers to. On the other hand, there would make no sense to use the subscript *ip* in the mobility tensor $\boldsymbol{\lambda}$ since a single absolute permeability tensor is defined for each element, thereby only the superscript *e* is required.

Equation 5.23 is the stabilized form of the mass conservation equation for deformable porous media. For the sake of comparison, the mobility tensor can also be applied to represent the non-stabilized mass conservation equation (Equation 4.39), which yields to:

$$\frac{\Delta\Omega_i}{M\Delta t} p_i - \sum_{\text{ip}\in\Gamma_i} \left[ \mathbf{s}^T_{\text{ip}} \boldsymbol{\lambda}^e \mathbf{B}_{\text{ip}} \mathbf{p}^e - \frac{\alpha}{\Delta t} \mathbf{s}^T_{\text{ip}} \left(\mathbf{N}_{\text{s}}\right)_{\text{ip}} \mathbf{u}^e \right] = b^p_i. \tag{5.25}$$

The concept of pseudo-mobility provides an interesting interpretation of how PIS operates. By looking at the second term inside brackets in Equations 5.23 and 5.25, it can be said that the face displacements are still computed by means of the shape functions (trial functions), but this is compensated by the addition of the pseudo-mobility in Equation 5.23.

The role of the pseudo-mobility can be better appreciated by defining a pseudo-velocity as:

$$\tilde{\mathbf{v}}_{\text{ip}} = -\tilde{\boldsymbol{\lambda}}_{\text{ip}} \mathbf{B}_{\text{ip}} \mathbf{p}^e. \tag{5.26}$$

In this case, the stabilized mass conservation equation takes the following form:

$$\frac{\Delta\Omega_i}{M\Delta t} p_i + \sum_{\text{ip}\in\Gamma_i} \left[ \mathbf{s}_{\text{ip}}^T \left( \mathbf{v}_{\text{ip}} + \tilde{\mathbf{v}}_{\text{ip}} + \alpha \mathbf{v}_{\text{ip}}^s \right) \right] = \frac{\Delta\Omega_i}{M\Delta t} p_i^o + \sum_{\text{ip}\in\Gamma_i} \left( \mathbf{s}_{\text{ip}}^T \tilde{\mathbf{v}}_{\text{ip}}^o \right), \tag{5.27}$$

where $\tilde{\mathbf{v}}_{\text{ip}}^o$ is computed by Equation 5.26 with $(\mathbf{p}^e)^o$ instead of $\mathbf{p}^e$.

The pseudo-velocity $\tilde{\mathbf{v}}$ represents the mechanism through which the lack of accuracy in the solid velocity approximation is compensated. In undrained consolidation, the fluid velocity $\mathbf{v}$ is nearly zero, so the solid velocity is responsible for satisfying mass by itself. This situation is known to cause locking in finite element formulations and the same mechanism seems to play a role here. In this context, the pseudo-velocity actuates as a relaxation to this condition by providing an extra mobility to the fluid. Moreover, undrained consolidation often occurs in very beginning of the simulation with small time step sizes, which causes the pseudo-mobility tensor to increase (see Equation 5.21). As a consequence, the pseudo-velocity in Equation 5.27 is active in the early stages of consolidation, and it gradually vanishes as the difference between $\tilde{\mathbf{v}}$ and $\tilde{\mathbf{v}}^o$ tends to zero.

### 5.4.1 Linear system assembling

For the stabilized formulation, Equation 5.23 replaces Equation 5.25 in the system of equations. In order to write the linear system in the same structure as in Equation 4.41, the stabilized mass conservation equation can be expressed in the following terms:

$$\frac{\Delta\Omega_i}{M\Delta t} p_i + \sum_{\text{ip}\in\Gamma_i} \left[ \frac{1}{\Delta t} \mathbf{Q}_{\text{ip}} \mathbf{u}^e - \left( \mathbf{H}_{\text{ip}} + \frac{1}{\Delta t} \tilde{\mathbf{H}}_{\text{ip}} \right) \mathbf{p}^e \right] = b_i^p + \tilde{b}_i^p, \tag{5.28}$$

where,

$$\tilde{\mathbf{H}}_{\text{ip}} = \frac{\alpha^2 L_d^2}{G} \mathbf{s}_{\text{ip}}^T \mathbf{B}_{\text{ip}} \mathbf{p}^e. \tag{5.29}$$

In this manner, Equations 5.28 and 4.27 for every node of the grid are grouped together and the resulting linear system takes the following form:

$$\begin{bmatrix} \dfrac{(\mathbb{A}-\tilde{\mathbb{H}})}{\Delta t}-\mathbb{H} & \dfrac{\mathbb{Q}}{\Delta t} \\ \mathbb{L} & -\mathbb{M} \end{bmatrix} \begin{bmatrix} \mathbf{p} \\ \mathbf{u} \end{bmatrix} = \begin{bmatrix} \mathbf{b}^p \\ \mathbf{b}^u \end{bmatrix} + \begin{bmatrix} \tilde{\mathbf{b}}^p \\ 0 \end{bmatrix} \tag{5.30}$$

Matrix $\tilde{\mathbb{H}}$ in Equation 5.30 is the result of assembling the contributions of $\tilde{\mathbf{H}}_{\text{ip}}$, as defined in Equation 5.29, and the vector $\tilde{\mathbf{b}}^p$ contains the values $\tilde{b}_i^p$.

It can be noticed that the linear system 5.30 can be obtained by simply adding the stabilization matrix $\tilde{\mathbb{H}}$ and vector $\tilde{\mathbf{b}}^p$ to the linear system of Equation 4.41. Adding stabilization terms to the linear system originated from equal-order approximations is a common procedure performed by a number of stabilization techniques already proposed in the FEM context (Choo & Borja, 2015; Oñate *et al.*, 2004; Preisig & Prèvost, 2011). From this perspective, the use of PIS can be regarded as a stabilization technique applied to EbFVM. It is important to emphasize that the application of PIS is not restricted to EbFVM, as it can be perfectly applied to the traditional (cell-center) finite volume formulation for generalized grids as well.

**Figure 5.3** – Regular hexahedron considered for the diffusive length calculation.

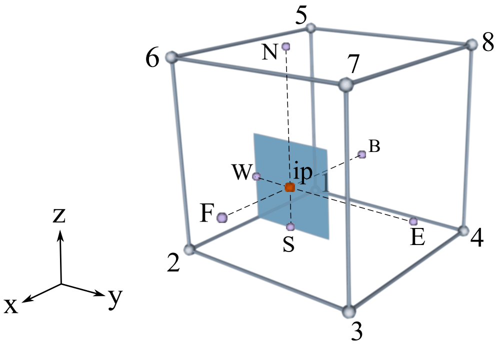

Source: Own authorship.

## 5.5 Diffusive length

The diffusive length presented in Equation 5.14 has to be determined for each type of element such as to ensure a proper approximation of the Laplacian term at the integration point. The procedure for obtaining this diffusive length is now detailed only for a hexahedron, since the procedure is exactly the same for the other types of elements.

Let us consider the finite difference approximation of the Laplacian of a generic scalar $\Phi$ at the integration point *ip* of the face contained by the regular hexahedron depicted in Figure 5.3. Assuming that $\Phi$ is known at the element vertices, the value of $\Phi$ at the auxiliary points $F$, $B$, $N$, $S$, $E$ and $W$ can be obtained evaluating the shape function derivatives at these positions. This yields to:

$$\begin{aligned}
\Phi_F &= \frac{9}{16}\Phi_2 + \frac{3}{16}\Phi_3 + \frac{3}{16}\Phi_6 + \frac{1}{16}\Phi_7 \\
\Phi_B &= \frac{9}{16}\Phi_1 + \frac{3}{16}\Phi_4 + \frac{3}{16}\Phi_5 + \frac{1}{16}\Phi_8 \\
\Phi_N &= \frac{3}{8}\Phi_5 + \frac{3}{8}\Phi_6 + \frac{1}{8}\Phi_7 + \frac{1}{8}\Phi_8 \\
\Phi_S &= \frac{3}{8}\Phi_1 + \frac{3}{8}\Phi_2 + \frac{1}{8}\Phi_3 + \frac{1}{8}\Phi_4 \\
\Phi_E &= \frac{3}{8}\Phi_3 + \frac{3}{8}\Phi_4 + \frac{1}{8}\Phi_8 + \frac{1}{8}\Phi_7 \\
\Phi_W &= \frac{3}{8}\Phi_1 + \frac{3}{8}\Phi_2 + \frac{1}{8}\Phi_6 + \frac{1}{8}\Phi_5 .
\end{aligned} \tag{5.31}$$

Now, let us define the following distances:

$$\Delta x = x_F - x_B, \qquad \Delta y = y_E - y_W, \qquad \Delta z = z_N - z_S. \tag{5.32}$$

The second derivative of $\Phi$ along each one of the three coordinate directions at the point *ip* can be approximated by finite differences, that is:

$$\left.\frac{\partial^2\Phi}{\partial x^2}\right|_{ip} \approx \frac{4}{\Delta x^2}\left(\Phi_F - 2\Phi_{ip} + \Phi_B\right) \tag{5.33}$$

$$\left.\frac{\partial^2\Phi}{\partial y^2}\right|_{ip} \approx \frac{32}{3\Delta y^2}\left(\frac{1}{4}\Phi_E - \Phi_{ip} + \frac{3}{4}\Phi_W\right) \tag{5.34}$$

$$\left.\frac{\partial^2\Phi}{\partial z^2}\right|_{ip} \approx \frac{32}{3\Delta z^2}\left(\frac{1}{4}\Phi_N - \Phi_{ip} + \frac{3}{4}\Phi_S\right), \tag{5.35}$$

Equations 5.31 are substituted in Equations 5.33, 5.34 and 5.35 and the terms multiplying the nodal values are grouped together and they are recognized to be the shape function values evaluated at the integration point *ip* of Figure 5.3. This procedure results in the following expressions:

$$\begin{aligned}
\left.\frac{\partial^2\Phi}{\partial x^2}\right|_{ip} &\approx \frac{1}{L_x^2}\left(\mathbf{N}^T\Phi^e - \Phi_{ip}\right)\\
\left.\frac{\partial^2\Phi}{\partial y^2}\right|_{ip} &\approx \frac{1}{L_y^2}\left(\mathbf{N}^T\Phi^e - \Phi_{ip}\right)\\
\left.\frac{\partial^2\Phi}{\partial z^2}\right|_{ip} &\approx \frac{1}{L_z^2}\left(\mathbf{N}^T\Phi^e - \Phi_{ip}\right),
\end{aligned} \tag{5.36}$$

where,

$$L_x^2 = \frac{\Delta x^2}{8}, \qquad L_y^2 = \frac{3\Delta y^2}{32}, \qquad L_z^2 = \frac{3\Delta z^2}{32}. \tag{5.37}$$

The coefficients $L_x^2$, $L_y^2$ and $L_z^2$ can be regarded as a diffusive length along each coordinate direction $x$, $y$ and $z$, respectively. In the same way, the 3-D Laplacian of $\Phi$ can be approximated at the point *ip* as:

$$\left.\nabla^2\Phi\right|_{ip} \approx \frac{1}{L_d^2}\left(\mathbf{N}^T\Phi^e - \Phi_{ip}\right), \tag{5.38}$$

regarded that a suited evaluation of the diffusive length $L_d^2$ is performed. In this work, this quantity is set as the resultant length of the three coordinate diffusive lengths:

$$L_d^2 = \frac{\Delta x^2}{8} + \frac{3\Delta y^2}{32} + \frac{3\Delta z^2}{32}. \tag{5.39}$$

Despite of equation (5.38) being valid in any case, equation (5.39) is suitable only for a regular hexahedron, as the one depicted in Figure 5.3. For irregular elements, the diffusive length $L_d^2$ may differ. Schneider & Raw (1987), however, suggested that equation (5.39) can be extended also for irregular elements by modifying the way the distances $\Delta x$, $\Delta y$ and $\Delta z$ are evaluated. Similar to what has been done in Schneider & Raw

**Figure 5.4** – Configuration of the auxiliary points for the regular elements: tetrahedron, prism and pyramid, from left to right.

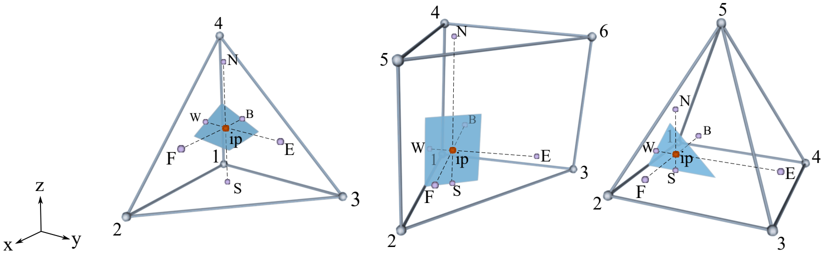

Source: Own authorship.

(1987) for two dimensions, in this work the calculation of these distances are performed by:

$$\Delta y = \Delta z = \sqrt{|\mathbf{s}_{ip}|}, \qquad \Delta x = \frac{1}{8}\frac{|\mathbf{J}_{ip}|}{|\mathbf{s}_{ip}|} \tag{5.40}$$

where $|\mathbf{s}_{ip}|$ is the area of the face containing the integration point and $|\mathbf{J}_{ip}|$ represents the determinant of the Jacobian matrix evaluated at the integration point *ip*. The value $|\mathbf{J}_{ip}|/8$ represents a sort of "volume" at the, even if it does not make sense geometrically speaking.

**Table 5.1** – Diffusive lengths for each type of element.

| | $\Delta x$ | $\Delta y$ | $\Delta z$ | $L_d^2$ |
|---|---|---|---|---|
| Hexahedron | $\frac{1}{8}\frac{\lvert\mathbf{J}_{ip}\rvert}{\lvert\mathbf{S}_{ip}\rvert}$ | $\sqrt{\lvert\mathbf{S}_{ip}\rvert}$ | $\sqrt{\lvert\mathbf{S}_{ip}\rvert}$ | $\frac{1}{8}\Delta x^2 + \frac{3}{32}\Delta y^2 + \frac{3}{32}\Delta z^2$ |
| Tetrahedron | $\sqrt{\lvert\mathbf{S}_{ip}\rvert}$ | $\sqrt{\lvert\mathbf{S}_{ip}\rvert}$ | $\frac{1}{24}\frac{\lvert\mathbf{J}_{ip}\rvert}{\lvert\mathbf{S}_{ip}\rvert}$ | $\frac{119}{4608}\Delta x^2 + \frac{119}{4608}\Delta y^2 + \frac{289}{4608}\Delta z^2$ |
| Prism | $\sqrt{\lvert\mathbf{S}_{ip}\rvert}$ | $\sqrt{\lvert\mathbf{S}_{ip}\rvert}$ | $\frac{1}{12}\frac{\lvert\mathbf{J}_{ip}\rvert}{\lvert\mathbf{S}_{ip}\rvert}$ | $\frac{25}{288}\Delta x^2 + \frac{5}{144}\Delta y^2 + \frac{3}{32}\Delta z^2$ |
| Pyramid | $\frac{1}{18}\frac{\lvert\mathbf{J}_{ip}\rvert}{\lvert\mathbf{S}_{ip}\rvert}$ | $\sqrt{\lvert\mathbf{S}_{ip}\rvert}$ | $\sqrt{\lvert\mathbf{S}_{ip}\rvert}$ | $\frac{8}{81}\Delta x^2 + \frac{13}{216}\Delta y^2 + \frac{1}{54}\Delta z^2$ |

Equation (5.38) is valid also for the other types of elements, as those depicted in Figure 5.4. In fact, it can be verified that equation (5.38) is always obtained for any type of element, with the auxiliary points represented in Figure 5.4. The computation of the diffusive length for each type of element is performed in the same way as described before for the hexahedral element. The values of $L_d^2$, $\Delta x$, $\Delta y$ and $\Delta z$ for each type of element, obtained by the procedure described above, are summarized in Table 5.1. The expressions presented in Table 5.1 are used for computing the diffusive length of each face the grid's elements.

CHAPTER

6

# RESULTS

The numerical formulation for poroelasticity problems, proposed in this work, is implemented in a in-house C++ object-oriented library named EFVLib (Maliska *et al.*, 2011). The main feature of this library is the grid handler, which is responsible for reading the data from the grid generator and building the topology[1] of the grid. Different from traditional finite element methods, the EbFVM requires additional geometrical entities such as faces, facets, sub-control volumes and control volumes to be constructed, which is precisely what is performed by the EFVLib. Moreover, this library is able to handle unstructured grids composed of different types of elements (tetrahedra, hexahedra, prisms and pyramids for three-dimensional grids and triangles and quadrangles for two-dimensional grids), thus it perfectly fits for the purposes of this work.

The poroelasticity equations in this work are solved in a monolithic way as they appear in Equations 4.41 and 5.30. Also known as fully-implicit solution, the benefit of this approach is that it treats the coupling between the governing equations in a implicit manner during the solution of the linear system, which provides robustness and stability specially for tightly coupled problems. Furthermore, preliminary tests performed during this thesis suggests the monolithic strategy is also faster than sequential techniques. However, as extensively reported in the literature (Gambolati *et al.*, 2011; Janna *et al.*, 2013; Zienckiewicz *et al.*, 1990), the

---

[1] Here, topology refers to the relationships between the different geometrical entities.

poroelasticity equations result in a saddle-point problem so the linear system becomes very ill-conditioned in some situations. When large scale problems are to be solved, one must rely on iterative solvers, usually based on Krylov sub-spaces. As the linear system becomes ill-conditioned, *ad-hoc* preconditioners must be devised in order to ensure efficiency of the iterative solver, or even to prevent it from diverging. In order to avoid these issues, the linear systems of Equations 4.41 and 5.30 are solved in this work by a LU-decomposition implementation found in PETSc (Balay *et al.*, 2017a,b). In spite of being a direct solver, the LU-decomposition provided by PETSc is a very efficient implementation and it performed quite well for the size of problems considered in this thesis.

In order to assess the performance of the Physical Influence Scheme in eliminating spurious oscillations, the stabilized (Equation 5.30) and non-stabilized (Equation 4.41) formulations are employed for solving all the problems presented in this chapter. First, test problems are solved and compared with analytical solutions for verifying the correct implementation and consistency of the formulations. In addition, some three-dimensional problems are designed to simulate situations close to reality. Although analytical solutions are not available for these problems, a simple comparison between both formulations can give an indication about the consistency of the additional terms introduced by PIS. Finally, its shown how spurious pressure modes can appear in all of these problems when the non-stabilized formulation is employed, and thus the effectiveness of using PIS can be assessed.

In all problems presented hereafter, the fluid is assumed to be water at 20°C, with the properties indicated in Table 6.1. The solid phase can be comprised of sand, silt, silty clay and clay (or a combination of them in some cases). The poroelastic properties of these materials are summarized in Table 6.2, where $k_{ii}$ are the components of the permeability tensor, $G$ is the shear modulus, $\lambda$ is the Lamé's first parameter, $c_s$ is the solid phase compressibility, $\alpha$ is Biot's coefficient and $\phi$ is porosity.

**Table 6.1** – Fluid phase properties.

| | $\mu$ (Pa.s) | $\rho$ (kg/m$^3$) | $c_f$ (MPa$^{-1}$) |
|---|---|---|---|
| Water at 20 °C | $1.002 \times 10^{-3}$ | 998.2 | $4.59 \times 10^{-4}$ |

**Table 6.2** – Poroelastic properties.

| | Sand | Silt | Silty Clay | Clay |
|---|---|---|---|---|
| $k_{xx} = k_{yy}$ (m$^2$) | $9.98 \times 10^{-10}$ | $9.98 \times 10^{-12}$ | $9.98 \times 10^{-13}$ | $9.98 \times 10^{-15}$ |
| $k_{zz}/k_{xx}$ | 0.1 | 1.0 | 1.0 | 1.0 |
| $G$ (MPa) | 1.732 | 0.819 | 0.819 | 0.819 |
| $\lambda$ (MPa) | 2.597 | 1.227 | 1.227 | 1.227 |
| $c_s$ (MPa$^{-1}$) | 0.0 | 0.0 | 0.0 | 0.0 |
| $\alpha$ | 1.0 | 1.0 | 1.0 | 1.0 |
| $\phi$ | 0.3 | 0.3 | 0.3 | 0.3 |

## 6.1 Verification

For verifying the correct implementation and consistency of the numerical formulations, Terzaghi's poroelastic column and Mandel's problem are numerically solved by both stabilized and non-stabilized formulations, and the results are compared with the analytical solutions of these problems. A description of these problems is provided in the following sub-sections.

### 6.1.1 Terzaghi's problem

Terzaghi's problem consists of a one-layered poroelastic column with impermeable boundaries, except for the top draining boundary ($p_T = 0$), where a compressive load is applied. The lateral boundaries are prevented from lateral movement and the bottom boundary is fixed, such as in a oedometric test. A schematic representation of its boundary conditions is illustrated in Figure 6.1. The analytical solution for pressure and displacement in time and space can be found in several works, e.g. Verruijt (2016). The results presented in this section are obtained for the geometry depicted in Figure 6.1, which consists of a 6 m high column with a 1 m$^2$ cross-section area. At the top boundary, a constant compressive load $\sigma_T = 10$ kPa is applied and the pressure is kept equal to zero in order to allow the fluid to flow out of the structure. The poroelastic column is composed of silt, with the poroelastic properties presented in Table 6.2.

In addition, Figure 6.1 also show some details about the grids employed for solving this problem. As it can be noticed in this figure, the grids are generated in a structured manner. The grid composed of prisms

**Figure 6.1** – Boundary conditions and grids for the solution of Terzaghi's problem.

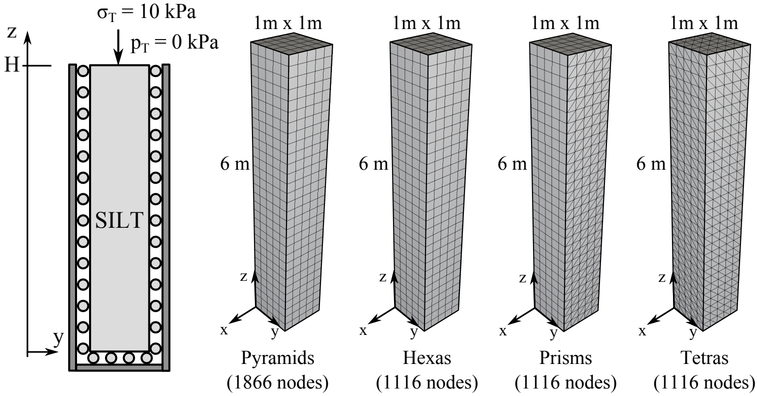

Source: Own authorship.

is built by dividing each hexahedron in half along its diagonal. Similarly, the tetrahedral grid is generated by dividing each hexahedron in six tetrahedra. For building the pyramids, an additional node is created inside each hexahedron and then six pyramids are created from it. Moreover, the grids present 30 layers of elements in the vertical direction and 5 in the horizontal directions.

This problem is numerically solved with a time step size of $\Delta t = 100$ s until the solution reaches the final time of 200 000 s. The pressure and vertical displacement profiles are taken along a vertical line (parallel to $z$ axis) and plotted against the vertical position for the time steps 100, 5 000, 30 000, 80 000 and 200 000 seconds. The numerical solutions are compared with the analytical solution (see Appendix A). Figures 6.2 and 6.3 show the numerical results obtained with the non-stabilized and the stabilized (PIS) formulations, respectively. These two figures also show the numerical results obtained with the grids depicted in Figure 6.1. As expected, both numerical formulations provided solutions with good agreement with the analytical profiles of pressure and vertical displacement. Except for the first time step ($t = 100$ s), where the stabilized and non-stabilized formulations provided slightly different results for pressure near the draining boundary, both formulations produced virtually identical results. Besides, it should be stressed that the solution is not reliable at the very first time step, since the solution perceives a very "coarse grid" in time. For the sake of clarification, this would be the same as obtaining the solution for $t = 200\,000$ s with a time step size of $\Delta t = 200\,000$ s. The solution in this case would be completely unreliable.

### 6.1.2 Mandel's problem

For Mandel's problem, a two-dimensional porous matrix is considered. As depicted in Figure 6.4, the bottom boundary ($z = -H$) is impermeable and prevented from vertical movement ($u_z = 0$). The top boundary ($z = H$) is also impermeable and a compressive force $2F = 20$ kN is applied. Additionally, the top boundary is always horizontal, that is, $\partial_y u_z = \partial_x u_z = 0$. The lateral boundaries ($y = L$ and $y = -L$) are permeable and can move freely in any direction. This problem has two planes of symmetry, $y = 0$ and $z = 0$, thereby the domain of calculus can be reduced to only one quarter, as illustrated in Figure 6.4. In this case, the boundary conditions applied at $y = 0$ and $z = 0$ are zero normal displacement and zero mass flux. Although Mandel's problem has only two dimensions, a three-dimensional cube ($1m \times 1m \times 1m$) is employed with the faces $x = -1$ and $x = 0$ prevented from normal displacement ($u_x = 0$)

**Figure 6.2** – Pressure and displacement profiles for Terzaghi's problem obtained with the non-stabilized formulation.

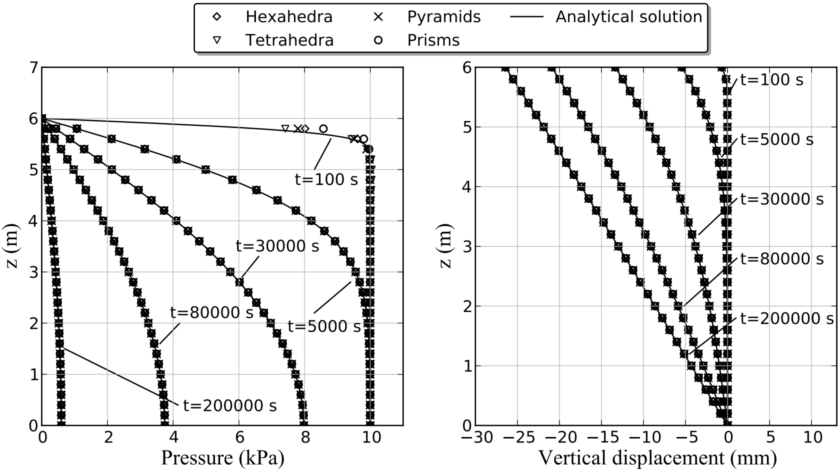

Source: Own authorship.

**Figure 6.3** – Pressure and displacement profiles for Terzaghi's problem obtained with the stabilized formulation.

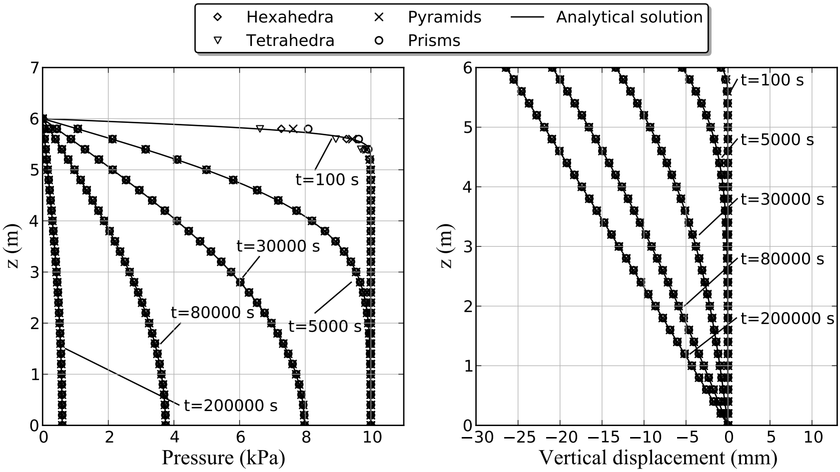

Source: Own authorship.

and impermeable. The grids employed are shown in Figure 6.4, and they present 15 nodes in each direction (the grid composed of pyramids has extra nodes).

**Figure 6.4** – Boundary conditions and grids for the solution of Mandel's problem.

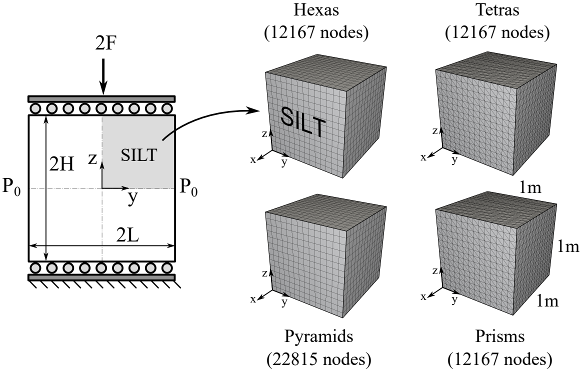

Source: Own authorship.

**Figure 6.5** – Pressure and displacement profiles obtained with the stabilized formulation with different types of grids.

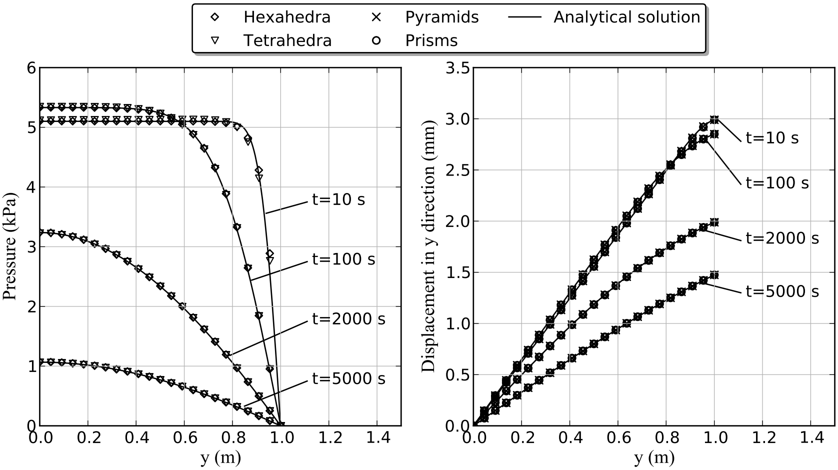

Source: Own authorship.

**Figure 6.6** – Pressure and displacement profiles obtained with the non-stabilized formulation with different types of grids.

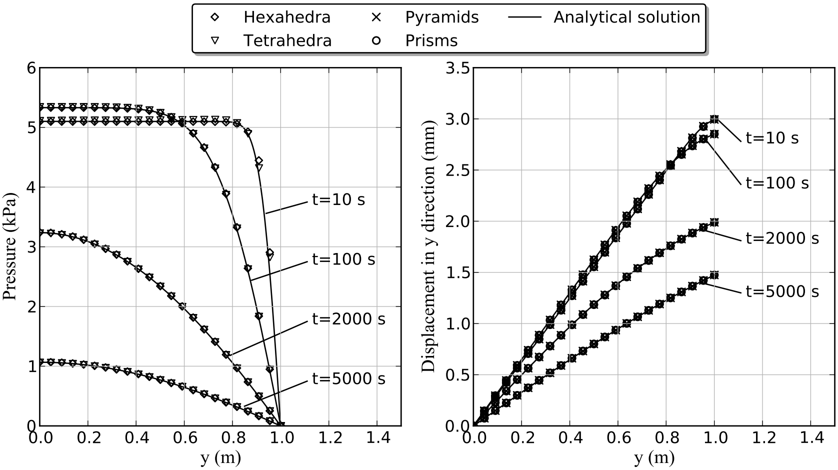

Source: Own authorship.

This problem is solved with both stabilized and non-stabilized formulations for all the grid types depicted in Figure 6.4. These are equally spaced grids with the same number of elements in the three coordinate directions. The numerical solutions are obtained with a fixed time step size of $\Delta t = 5$ s, and the analytical solutions for the pressure and displacement $(u_y)$ fields are presented in Appendix A. Figures 6.5 and 6.6 show the pressure and displacement profiles obtained with the stabilized and non-stabilized formulations, respectively, for different time levels, as indicated. These figures show good agreement between the analytical and numerical profiles for both formulations. Each type of grid produced a slightly different solution for the pressure profile at $t = 10$ s, but this is due to the time step size employed.

In Figures 6.5 and 6.6, it can be observed a small pressure increase for early times ($t = 100$ s) followed by a descendant behavior. This is known as Mandel-Cryer's effect (Cryer, 1963; Mandel, 1953), and it can be better visualized in Figure 6.7, where the pressure is monitored at coordinates $(0,0,1)$ and plotted against time. The displacement component $u_y$ is monitored at position $(0,1,0)$ and it also show good agreement with the analytical solutions. In this figure, only the results obtained from stabilized formulation are shown, since the non-stabilized version produced virtually the same results.

## 6.2 Three-dimensional test cases

The spatial domain for both three-dimensional problems presented in this section is a 50 meters high cylinder with a 200 meters radius. Due to symmetry of the boundary conditions applied in both cases, only one quarter of the cylinder is considered. As depicted in Figure 6.8, the porous matrix is composed of different strata representing a highly permeable sandy aquifer entrapped by two silty clayey aquitards with low permeability, all of them resting upon a silty layer. The bottom ($z = 0$ m) and circular ($x^2 + y^2 = 250^2$) boundaries are fixed and impermeable, while the top boundary is traction-free and fully-drained. To ensure the symmetry of the problem, the internal boundaries, defined by planes $y = 0$ m and $x = 0$ m, are impermeable and prevented from displacement in their normal directions. In the following subsections the particularities of each problem are discussed and the results are presented.

**Figure 6.7** – Pressure and displacement profiles obtained with the stabilized formulation with different types of grids.

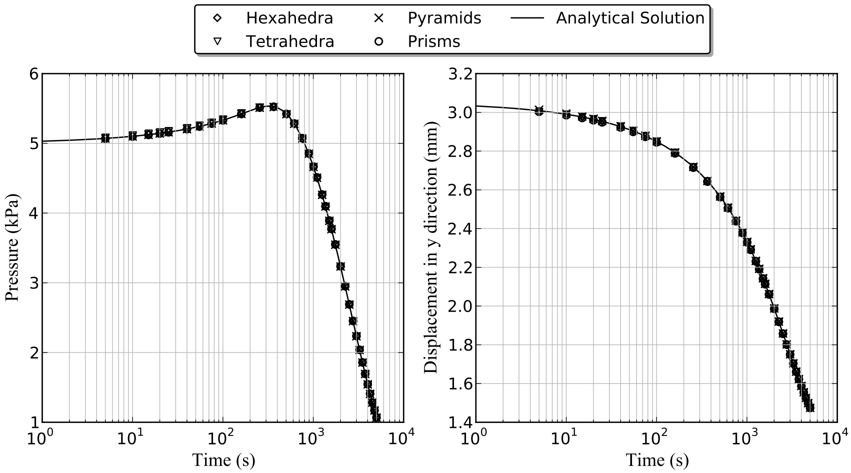

Source: Own authorship.

### 6.2.1 Strip-footing problem

In this problem, a time-dependent compressive load $\sigma(t)$ is applied on the top boundary over a circular area of 10 meters radius positioned at $x = y = 0$ meter. The external load linearly increase from 0,0 to 8,0 kPa in three days, and then remains constant, as represented in Figure 6.9. Under these conditions, the pore pressure in the region below the area where the external load is applied is expect to increase as it is subjected

**Figure 6.8** – Representation of a sandy aquifer entrapped by two aquitards.

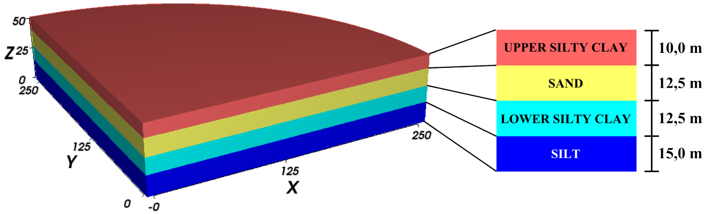

Source: Own authorship.

to a compressive volumetric strain. The material stiffness and permeability play key roles for the pressure field development. Under an external load, the amount of volumetric strain a porous matrix is subjected to directly depends on the material stiffness. By its turn, the rate of volumetric strain is intimately related to the pore pressure changes. For instance, if all boundaries are impermeable, the mass conservation equation reduces to:

$$p = -\alpha\epsilon_v = -\alpha\nabla\cdot\mathbf{u}. \tag{6.1}$$

Thus, the softer the material the more pressure increase is observed under an external compressive load. Hence, a small pressure increase and a fast dissipation is expected in the sandy layer, since it is stiffer and more permeable than the other layers (see Table 6.2). By contrast, an opposite behavior should be observed in the silty clayey and silty layers. In particular, the upper silty clayey layer should experience the largest overpressure, since it is softer than the sandy layer and has a low permeability. This is actually the physics behind the Mandel-Cryer's effect (Cryer, 1963; Mandel, 1953), which is the clearest effect of poromechanical coupling.

For solving this problem, a grid composed of 20.518 tetrahedral elements and 4.193 nodes is used for representing the geometry illustrated in Figures 6.8 and 6.9. As shown in Figure 6.10, the grid is locally refined in the region near the center line, where significant changes in pressure and displacements are most likely to occur. The average size of the elements in the refined region is approximately 1,0 meter.

The numerical solutions are run until 10 days with a time step size of $\Delta t = 0{,}01$ day. Figure 6.11 shows the pressure field at different times. The colorbars in this figure represent the pressure range for each time

**Figure 6.9** – Time dependent compressive load over a 10 meters radius region.

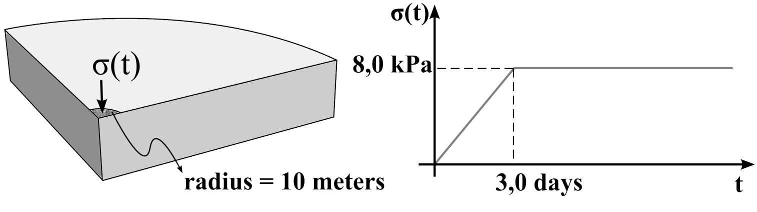

Source: Own authorship.

indicated. It can be observed that the pore pressure increases mainly in the silty clayey and silty layers, as they are softer than the sandy layer, which causes them to be subjected to higher levels of volumetric strains. In addition to this, the sandy layer is more permeable thus it dissipates pressure more quickly than in the other layers. These behaviors can be better appreciated in Figure 6.12, where the pressure and vertical displacement are monitored at specific points in each layer along the line $x = y = 0$. In fact, these points are taken at $z = 4{,}81$ m (silty layer), $z = 21{,}76$ m (lower silty clayey layer), $z = 34{,}39$ m (sandy layer) and $z = 44{,}21$ m (upper silty clayey layer). This figure show that the pressure increases until the third day, suggesting it depends on the rate at which the external load is applied. Once the external load becomes constant, the pore pressure in each layer starts to dissipate. The rightmost graph in Figure 6.12 also show that the rate of compaction in each layer also changes when the external load becomes constant.

The pressure profile along line $x = y = 0$ m is represented in Figure 6.13, where the pore pressure behavior in each layer can be clearly observed. Figure 6.13 also show the subsidence along radial direction. This figure shows that a circular region of approximately 60 meters is affected by the external load. It is also important to stress that both Figures 6.12 and 6.13 show the numerical results obtained with the stabilized and non-stabilized formulations. As shown in these figures, both formulations produced virtually the same results.

**Figure 6.10** – Grid composed of 20.518 tetrahedral elements and 4.193 nodes.

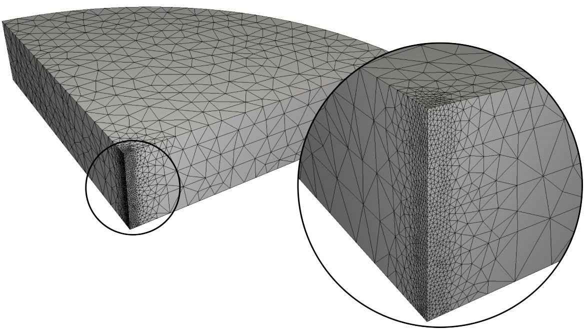

Source: Own authorship.

### 6.2.2 Groundwater withdrawal

For the groundwater withdrawal problem, a producing vertical well is placed at the centerline $x = y = 0$ m of the geometry and no external

**Figure 6.11** – Three-dimensional pressure field at different times.

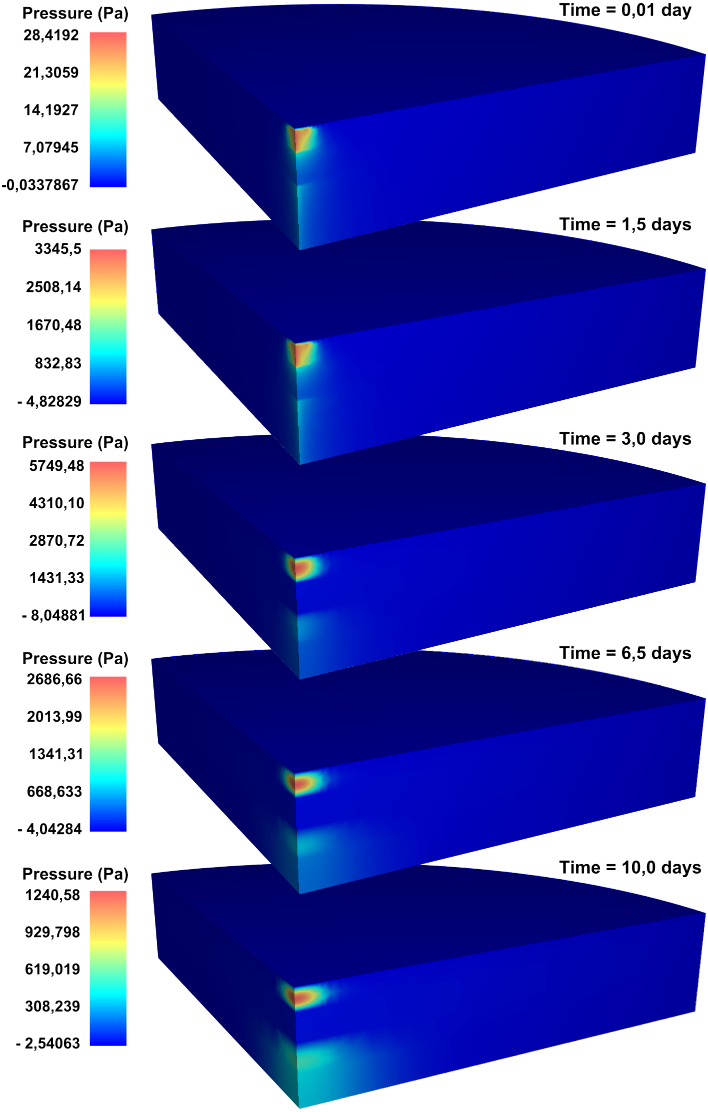

Source: Own authorship.

**Figure 6.12** – Pressure and displacement vs. time at different layers.

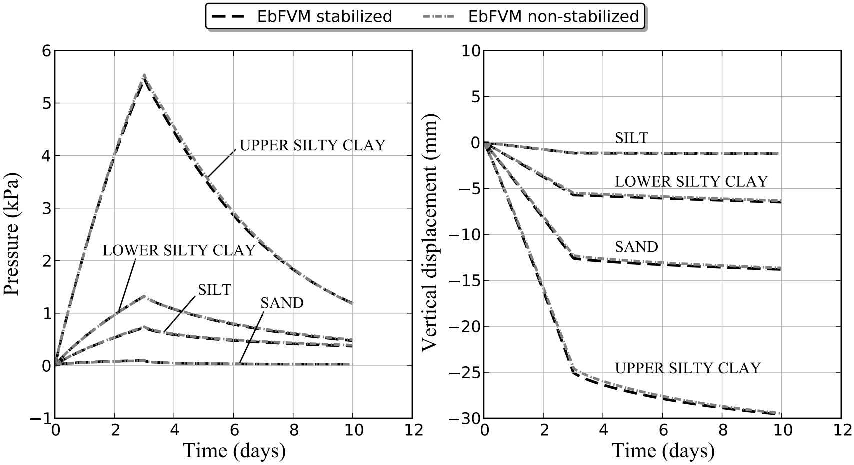

Source: Own authorship.

**Figure 6.13** – Pressure profile at the center line and subsidence along the radial direction.

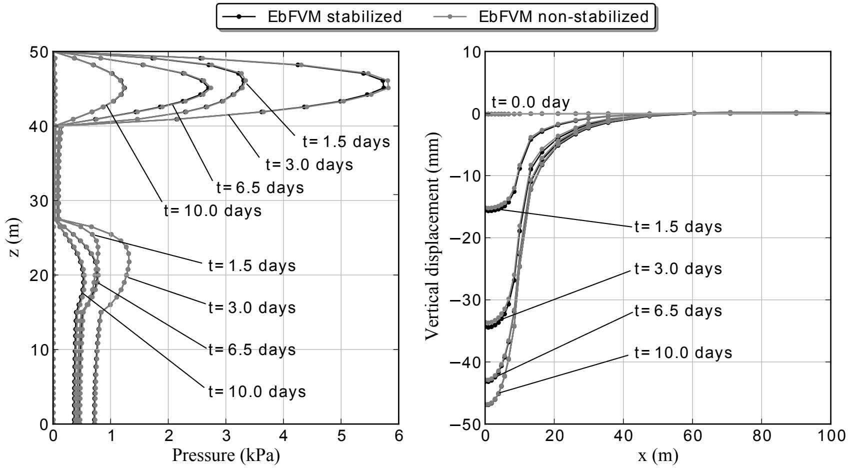

Source: Own authorship.

load is on its boundaries. The well radius is 5 cm and it produces at a constant volumetric flow rate of $q_T = 8 \times 10^{-5}$ m$^3$/s only in the sandy layer (i.e., for $27,5 \leqslant z \leqslant 40$). The mass conservation equation for the control volumes intercepted by the well must consider the mass flux due to the presence of the well. Notice that the volumetric flow rate, $q_i$, at the segments of well of each control volume $i$ is not known. Only the total volumetric flow rate $q_T$ is known. However, a mass balance on the well implies that the sum of the volumetric flow rate at each segment of well equals the total volumetric flow $q_T$, that is,

$$\sum_{i \in \Lambda} q_i = q_T, \tag{6.2}$$

where $\Lambda$ denotes the set of control volumes intercepted by the producing region of the well. The volumetric flow rate $q_i$'s are modeled in terms of the difference between the pressure of the control volume $p_i$ and the pressure inside the well, denoted by $\Pi$. In addition, $q_i$ is inversely proportional to the fluid viscosity and is directly proportional to a well index $WI_i$ defined for each control volume $i$. That is:

$$q_i = \frac{WI_i}{\mu} \left(p_i - \Pi\right). \tag{6.3}$$

Although other choices are possible, the well pressure $\Pi$ in this work is regarded to be constant at any position. Despite of that, the value of $\Pi$ is unknown, thus it requires an additional equation to be added to the linear system. This equation is the mass balance for the well, which is obtained by substituting Equation 6.3 into Equation 6.2, leading to:

$$\sum_{i \in \Lambda} \frac{WI_i}{\mu} \left(p_i - \Pi\right) = q_T. \tag{6.4}$$

An adaptation of Peaceman's well model (Peaceman, 1983) is employed for computing the well indexes $WI_i$, as detailed in Appendix B.

In order to better capture the radial pattern of the fluid flow in the near-well region, a radial grid composed 90 prisms and three layers of hexahedra (adding up to 270 hexahedra), as shown in Figure 6.14. The rest of the domain is composed of 31.655 tetrahedra and the transition between the hexahedral and tetrahedral elements is performed by 108 pyramids. The total number nodes is 6.764.

The solution is obtained with a time step size of $\Delta t = 1,0$ day and the

**Figure 6.14** – Hybrid grid used for solving the groundwater withdrawal. The detailed zoom shows the radial grid in the near-well region (the upper silty layer has been removed for better visualization).

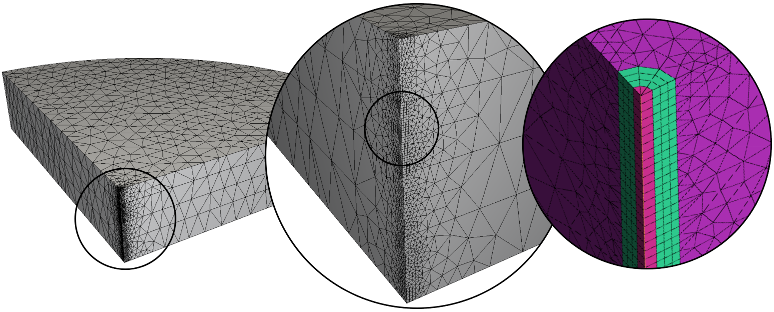

Source: Own authorship.

well produces for 1.000 days. Figure 6.15 shows the pressure fields for the time steps indicated. Since the inital pressure is set to zero and the well is pumping fluid out of the domain, negative values for pressure should be expected over the entire domain. Indeed, in the near-well region, the most negative values are found, denoted by dark blue. However, for the first two selected times (5 and 40 days), positive values of pressure can be observed by noticing the correspondent color bars. In fact, these positive values vanish only after day number 110, after which only negative values of pressure are observed.

Figure 6.16 shows the pressure and vertical displacement profiles along the vertical centerline ($x = y = 0$ m) for a few selected times, as indicated. It can be verified that slightly different solutions for pressure and vertical displacement are obtained with the stabilized and non-stabilized formulations for early times (first and fifth days). An interesting behavior of the vertical displacement is observed in the rightmost graphic of Figure 6.16 for early times. When the well starts to produce, a negative pressure field suddenly appears in the near-well region, which pulls the solid grains in the nearby towards the well due to the steep pressure gradient. As a consequence, the solid grains immediately above the well are pulled down (negative displacement), whereas the solid gains below the well are attracted upwards (positive displacement). This phenomenon is observed in Figure 6.16 for the first and fifth days. Eventually, the elastic behavior of

**Figure 6.15** – Three-dimensional pressure field at different times.

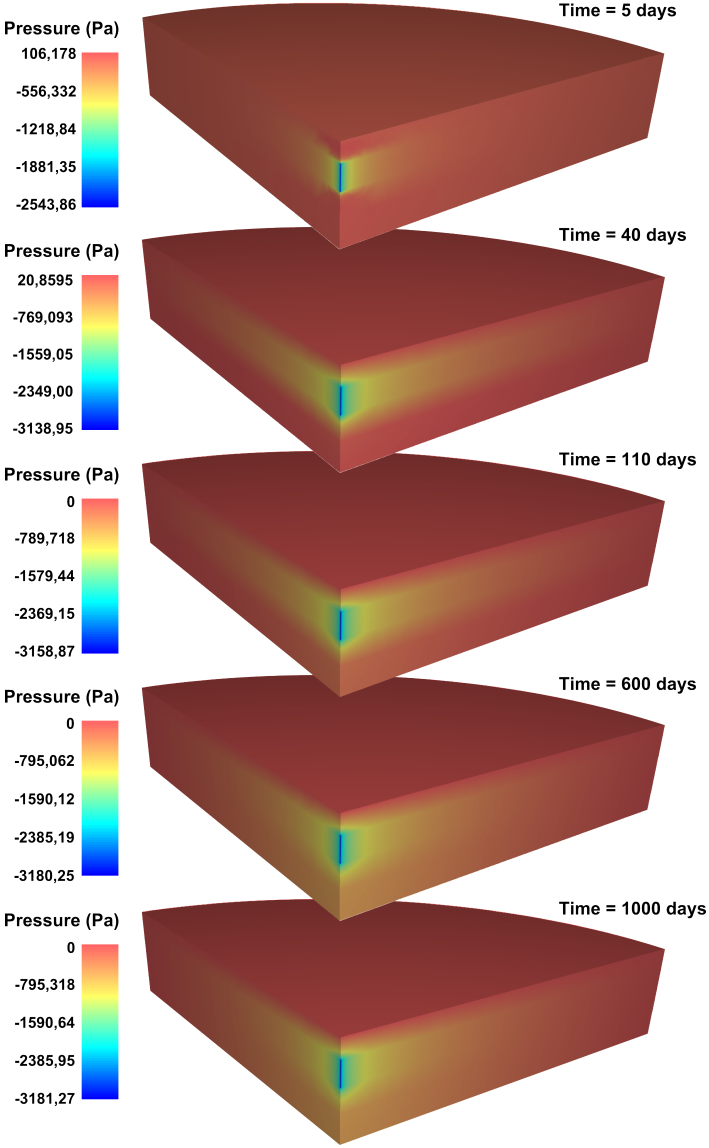

Source: Own authorship.

the porous matrix counterbalances the suction effect caused by the well and the whole structure starts to settle down.

The leftmost graphic in Figure 6.16 allows for a clear view of the positive values of pressure mentioned before. These values are observed in the adjacent layers of the aquifer (upper and lower silty clayey layers and the silty layer) and they are more pronounced in the upper silty clayey layer during the first day of production. This is actually a well-known phenomenon called “reverse-water level fluctuation” (Kim & Parizek, 1997; Verruijt, 1969) and it was first reported in the village of Noordbergum, the Netherlands, which is why it is also known as the Noordbergum effect. This is a clear evidence of the coupling between geomechanics and fluid flow in porous media and indeed it can only be captured by a coupled consolidation model.

Figure 6.17 provide a better view on the Noordbergum effect. For building these graphics, the pore pressure and vertical displacement are monitored as time passes at the upper silty clayey layer ($z = 47,0$ m), the lower silty clayey layer ($z = 20,1$ m) and the silty layer ($z = 4,5$ m). In addition, the time step size has been reduced to 6 hours (0,25 day). As shown, the pore pressure of the three adjacent layers initially rises and

**Figure 6.16** – Pressure and vertical displacement profiles along the centerline ($x = y = 0$).

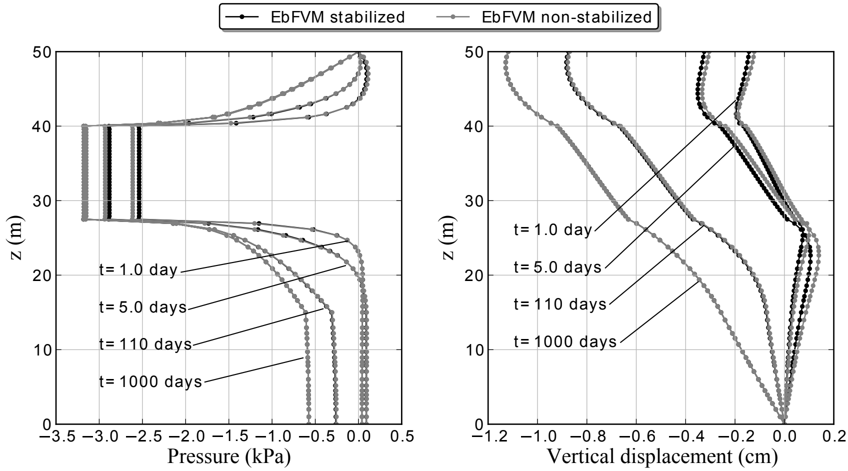

Source: Own authorship.

**Figure 6.17** – Pressure and vertical displacement profiles along the centerline ($x = y = 0$).

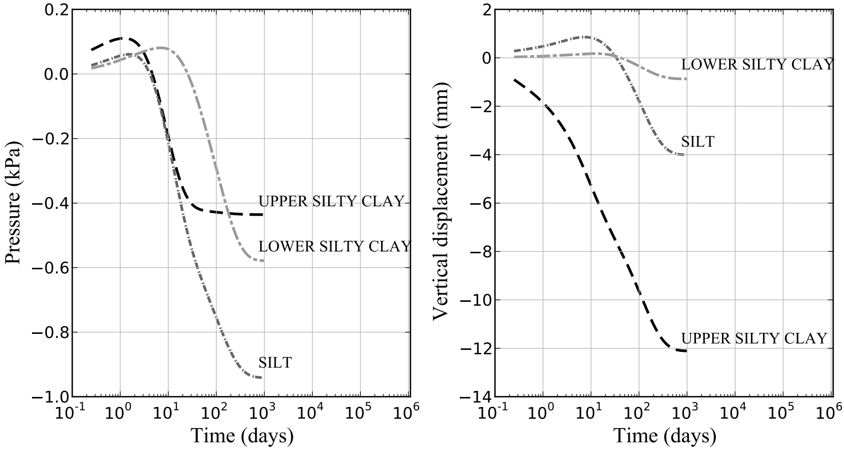

Source: Own authorship.

then it starts to fall after 10 days approximately. This figure also show the positive vertical displacements in the lower silty clayey and silty layers. After 1.000 days the solution seems to reach a steady-state condition.

## 6.3 Convergence analysis

According to the LBB condition (Babuška, 1971; Brezzi, 1974) for stability, non-physical solutions may be obtained when the same order of approximation is employed for both pressure and displacement fields in Biot's model equations. With the purpose of predicting if pressure instabilities are to be expected, this section aims at verifying the order of approximation of pressure and displacement for the different types of grids. The errors are computed by taking the $L^2$ norm of the error vectors of pressure and displacement, as presented in Equation 6.5 for a general scalar $\Phi$. The error vectors are obtained by subtracting the numerical solution vector from the analytical solution of Mandel's problem.

**Figure 6.18** – $L^2$ norm of the error vectors of pressure and displacement for the non-stabilized formulation.

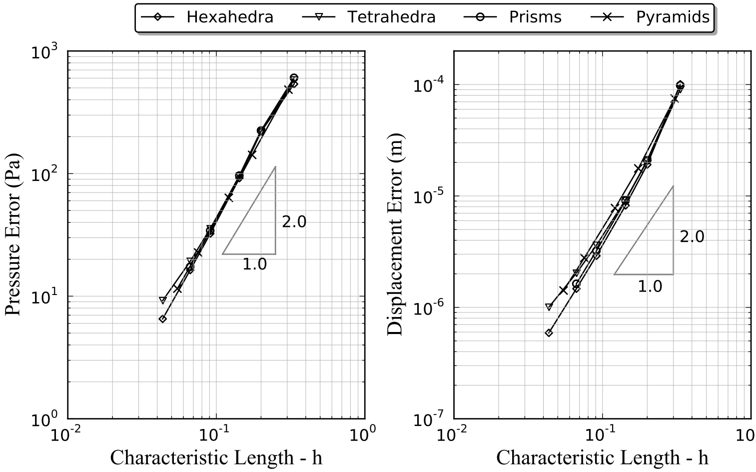

Source: Own authorship.

$$\text{error} = \sqrt{\sum_{i=1}^{n} \Delta\Omega_i \left[\Phi_i - \Phi(\mathbf{x}_i)\right]^2} \tag{6.5}$$

In Equation 6.5, $\Phi_i$ represent the numerical solution of $\Phi$ at the control volume $i$ and $\Phi(\mathbf{x}_i)$ is the analytical (continuous) solution evaluated at position $\mathbf{x}_i$.

The order of approximation of the pressure and displacement fields can be verified by analyzing the error decay as the grid size is reduced. The grid size is represented by a characteristic length $h$ computed as the cubic root of the average volume of the control volumes of the grid. Mandel's problem is numerically solved with progressively refined grids, as the ones depicted in Figure 6.4. By analyzing the slope of the error decay for the grids composed of different types of elements, it is possible to assess the order of approximation provided by the shape functions (as detailed in Chapter 3) associated to these elements.

Figures 6.18 and 6.19 show the convergence behavior of pressure and displacement for the non-stabilized and stabilized formulations, respectively. The numerical results for pressures and displacement profiles are

**Figure 6.19** – $L^2$ norm of the error vectors of pressure and displacement for the stabilized formulation.

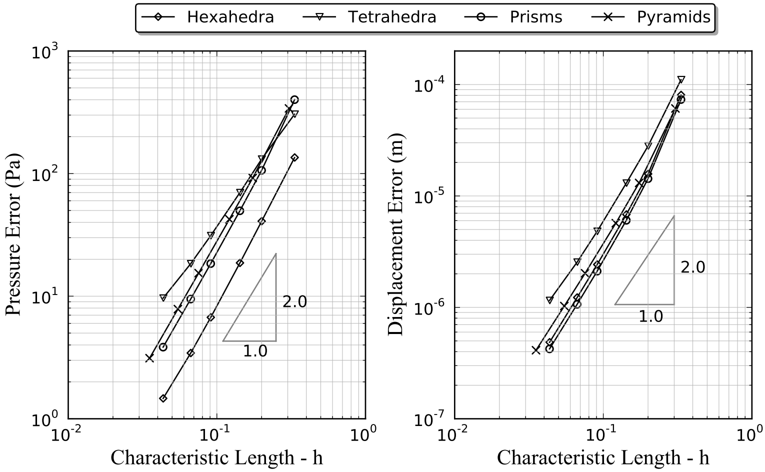

Source: Own authorship.

taken at $t = 100$ s with a time step size of $\Delta t = 0.1$ s. The important thing to notice in these two figures is that both pressure and displacement present a second-order decay of the $L^2$ norm of the error vector as the grid is refined, thus revealing a second-order approximation for both pressure and displacement. Although it is a positive characteristic from an accuracy standpoint, these formulations, according to Babuška (1971) and Brezzi (1974), are prone to suffer from numerical instabilities under certain situations, which are investigated latter in this chapter.

In addition, it should be pointed out that, even though a higher order approximation is employed by the PIS for approximating the displacement vector at the integration points in the mass conservation equation, the overall approximation of the displacement still remains of second-order. This is the reason it was stated in Subsection 5.3.1 that PIS mimics a higher order approximation for displacement, instead of actually providing it. Although it does not actually improve the order of approximation of the displacement field, it does eliminate the pressure instabilities, as shown in the following sections.

Another interesting point that deserves attention is that the pressure and displacement errors obtained by the stabilized formulation, presented in Figure 6.19, are smaller than the ones produced by the non-stabilized formulation, as presented in Figure 6.18. This suggests that the Physical Influence Scheme actually improves the accuracy of the numerical solution, though the order of approximation remains the same.

## 6.4 Numerical instabilities

As expected, the convergence analysis presented in the previous section revealed the same order of approximation for both pressure and displacement fields. According to (Babuška, 1971; Brezzi, 1974), equal-order interpolation pairs are prone to suffer from instabilities, particularly when undrained consolidation takes place close to a draining boundary. In this situation, the pressure gradient near the draining boundary must be accurately captured in order to compute the correct fluid velocities for mass conservation. For instance, Figure 6.20 illustrates a one-dimentional grid, where a pressure equal to zero is prescribed to node 1 (drained boundary) and the exact pressure profile is shown. As discussed in Chapter 4, the pressure gradient must be computed at the integration points in order to compute the Darcy velocities. For the grid shown in Figure 6.20a, the correct pressure gradient provided by the exact solution is zero at the integration point, but the numerical approximation "perceives" a non-zero gradient, which causes a non-zero velocity to appear where it should not

**Figure 6.20** – Pressure profiles at (a) $t = t_0$, (b) $t = t_1 > t_0$ and (c) $t = t_0$ with a refined grid.

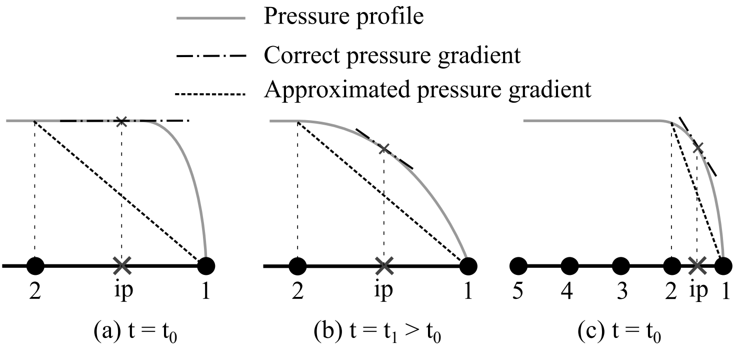

(a) $t = t_0$ (b) $t = t_1 > t_0$ (c) $t = t_0$

Source: Own authorship.

be. From the perspective of the grid in Figure 6.20a, an undrained consolidation is taking place, because the Darcy velocity at the first integration point near the draining boundary is still zero. At a latter time (Figure 6.20b), pressure at node 2 is already disturbed by the pressure front, thus a good approximation of the pressure gradient is obtained at the integration point. However, if it is mandatory to solve at $t = t_0$, a remedy to correctly capture the pressure gradient is to refined the grid until the node 2 is affected by the pressure front, as shown in Figure 6.20c. In this case, the grid does not “perceive” an undrained consolidation anymore, since the first integration point near node 1 already experience a non-zero Darcy velocity (pressure gradient).

The purpose of the discussion above is to clarify that the term “undrained consolidation”, in the context of the present work, actually depends on the grid size close to the draining boundary. It can be stated that, given a time step size and a porous material, an undrained consolidation can always be obtained by simply coarsening the grid. By choosing a porous material and a relatively fine grid, a sufficiently small time step size can also produce an undrained condition. Finally, for a given grid size and a time step size, an undrained consolidation can be achieved by choosing a porous material with a sufficiently low permeability (more specifically, a small consolidation coefficient, as pointed out by Vermeer & Verruijt (1981)). In the following subsections, undrained consolidations are induced in different situations in order to investigate the performance of the stabilized and non-stabilized formulations.

### 6.4.1 One-layered poroelastic column

Terzaghi’s problem is solved with the same grids depicted in Figure 6.1. The time step size is set to $\Delta t = 1,0$ second and the solutions are obtained with the stabilized and non-stabilized formulations. The pressure profiles are taken at $t = 10,0$ seconds and compared with the analytical solution in Figure 6.21 for each type of grid. It can be observed in this figure that the anlytical pressure solution at the first node below the top draining boundary is still not affected by the pressure front. This is precisely the situation described in Figure 6.20, in which the grid “perceives” an undrained consolidation. Figure 6.21 shows that spurious modes of pressure are obtained with the non-stabilized formulation. By contrast, the stabilized formulation effectively prevent the solution from numerical

**Figure 6.21** – Terzaghi's problem: pressure profiles at $t = 10,0$ seconds obtained with both stabilized and non-stabilized formulations for different types of grids.

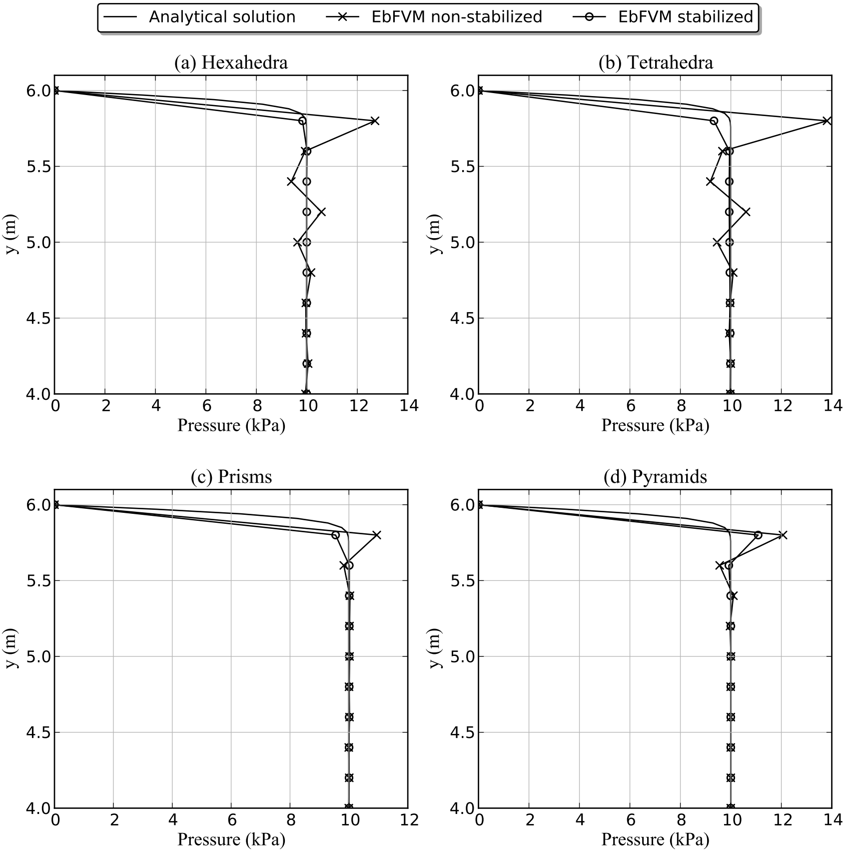

Source: Own authorship.

instabilities for the grids composed of hexahedra, tetrahedra and prisms. A small numerical diffusion is observed in Figures 6.21b and 6.21c for the grids composed of tetrahedra and prisms, respectively. For the grid composed of pyramids, however, although the stabilized formulation does reduce the instability at the node immediately below the draining boundary, it is not able to completely remove it. This failure probably occur because of the way the diffusive length $L_d$ is computed for the pyramidal element.

As discussed in Chapter 3, the internal faces associated to the edges of the base of the pyramid are always triangular, whereas the faces associated to the edges connecting to the top vertex (vertex number 5 in Figure 3.7) are always quadrilateral. However, the diffusive length derived in Section 5.5 for the pyramid (presented in Table 5.1) considered only the triangular face, and this expression has been used for every internal face of the pyramid, regardless of its geometrical shape. In other words, the computer program calculates a diffusive length for a quadrilateral face of the pyramid as if it was a triangular face, which is clearly an inconsistency. At first, it was not believed it would cause much problem as the sizes of both triangular and quadrilateral faces of a pyramid are approximately the same. Nevertheless, the results shown in Figure 6.21d have proven quite the opposite, that is, the diffusive length has to be accurately computed in order to provide a second-order approximation for the Laplacian term, otherwise it might not provide the necessary stabilization for the solution.

**Figure 6.22** – Two-layered poroelastic column: boundary conditions, geometry and computational grids.

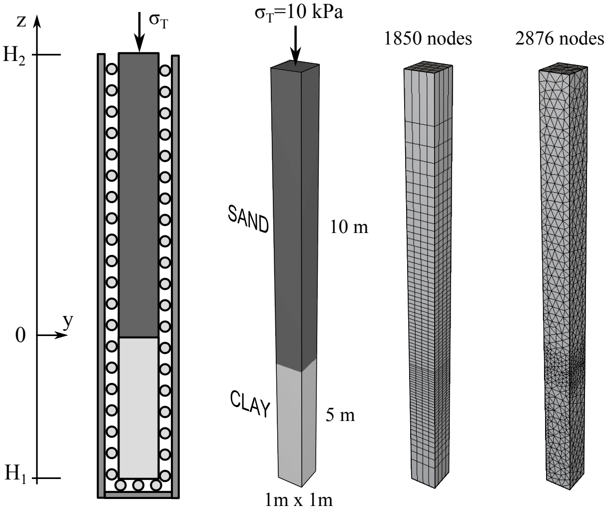

Source: Own authorship.

### 6.4.2 Two-layered poroelastic column

In this case, a 15 meters poroelastic column composed of two layers of different materials is considered. The boundary conditions are basically the same as the one-layered poroelastic column of the previous subsection. As illustrated in Figure 6.22, a 10 meters layer of sand rests upon a 5 meters layer of clay. According to Table 6.2, the absolute permeability of sand and clay differ from each other 5 orders of magnitude, so the pressure field is expected to develop much faster along the sandy layer while the pore pressure remains practically unaffected in the clayey layer. This problem is solved for two types of grids: one composed of hexahedra with 1850 nodes, and another one composed of tetrahedra with 2876 nodes. Both of them locally refined in the interface between the two layers in order to better capture the steep pressure gradient that establishes in this region.

**Figure 6.23** – Pressure fields obtained with the non-stabilized and stabilized formulations for the (a) hexahedral and (b) tetrahedral grids.

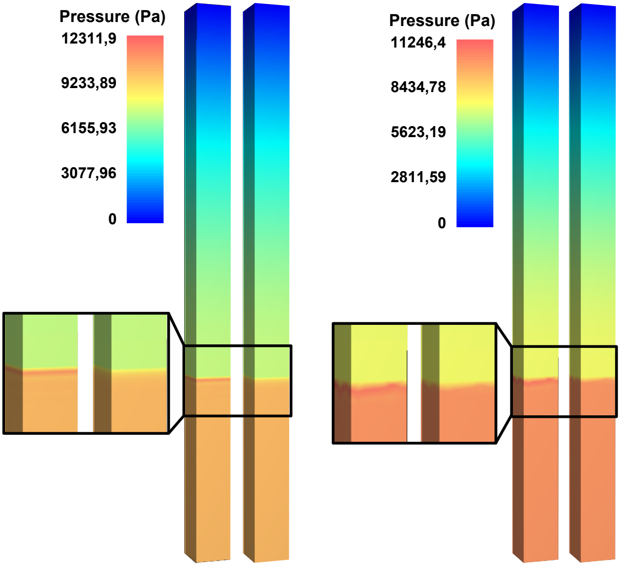

(a) Hexahedral grid

(b) Tetrahedral grid

Source: Own authorship.

**Figure 6.24** – Pressure profiles at $t = 1000$ seconds for both formulations.

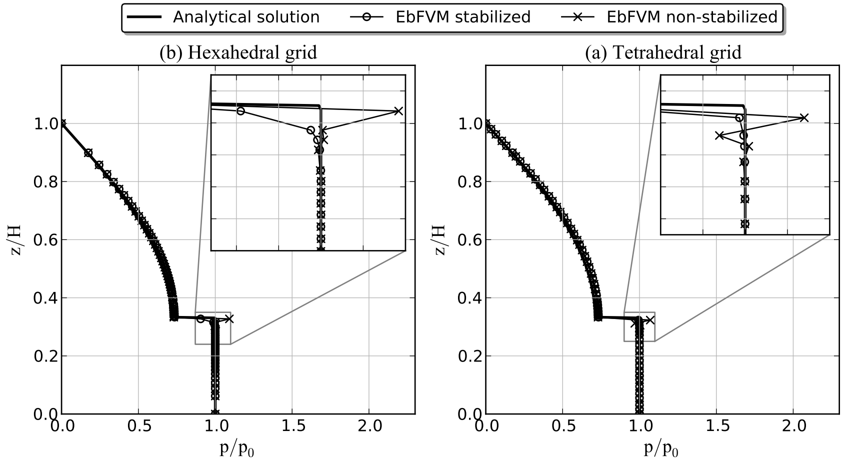

Source: Own authorship.

Figure 6.23 shows the pressure fields at $t = 1000$ seconds for the two types of grids, as indicated, obtained with both non-stabilized (on the left) and stabilized (on the right) formulations. In both grids a zoom is placed on the interface between the two materials, where some pressure peaks can be identified by the color red (according to the color bar provided) for the non-stabilized formulation. These values can be better visualized in Figure 6.24, where the pressure profile is plotted along one of the geometry's vertical edges. It can be observed that the pressure wiggles are effectively removed by the PIS in the two grids, although an overly diffusive solution is produced for the hexahedral one.

### 6.4.3 Mandel's problem

In order to induce an undrained consolidation for Mandel's problem, the time step size is reduced to $\Delta t = 0,1$ second and the numerical pressure profiles are taken at $t = 3,0$ seconds and compared to the analytical solution. Moreover, coarser grids, similar to those of Figure 6.4, are employed. The grids composed of hexahedra, tetrahedra and prisms have 1331 nodes, whereas the grid composed of pyramids almost doubles the

**Figure 6.25** – Pressure field at $t = 3,0$ seconds obtained with the non-stabilized formulation.

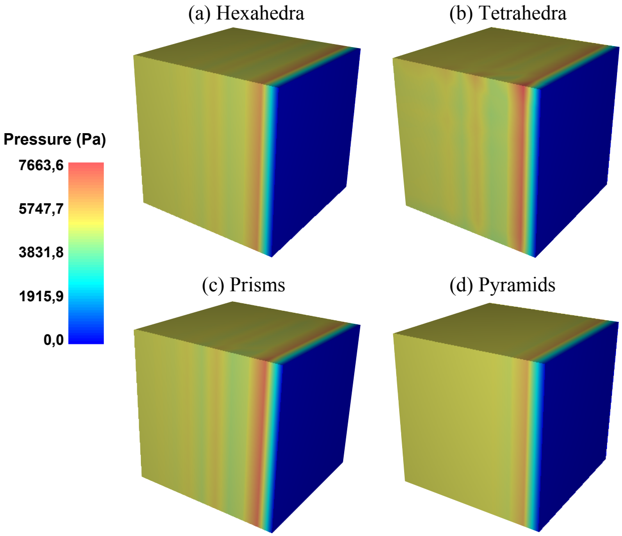

Source: Own authorship.

number of nodes (2331 nodes) since they build an extra vertex at the barycenter of each hexahedral element.

Figures 6.25 and 6.26 show the numerical pressure fields obtained with the non-stabilized and stabilized formulations, respectively. The pressure fields presented in Figure 6.25 are clearly inappropriate since there is no physical reason to explain the pressure peaks that can be observed in this figure. By employing PIS to compute the volumetric strains, smooth solutions are obtained for the hexahedral and tetrahedral grids, as shown in Figures 6.26a and 6.26b, respectively. For the grids composed of prisms and pyramids, however, Figures 6.26c and 6.26d show that, although the pressure instabilities are reduced, the Physical Influence Scheme implemented is not able to provide oscillation-free solutions.

The pressure profiles along the horizontal direction, perpendicular to the draining boundary (zero pressure), are shown in Figure 6.27 and compared with the analytical solution. In this figure it can be observed that the PIS applied to the hexahedral grid produces a high quality solution, whereas for the tetrahedral grid some numerical diffusion is introduced to the solution. The stabilized formulation for the grid composed

**Figure 6.26** – Pressure field at $t = 3,0$ seconds obtained with the stabilized formulation.

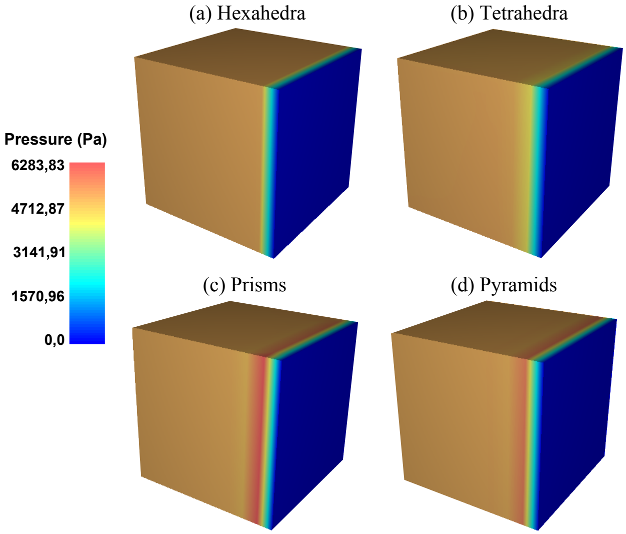

Source: Own authorship.

of prisms, shown in Figure 6.27c, is able to remove most of the instabilities but it fails to provide smooth solutions close to the draining boundary, which is the critical region. The grid composed of pyramids present solutions with less instabilities because of its greater number of nodes. Figure 6.27d shows a slight reduction of the pressure instabilities when PIS is employed but it is not able to completely remove them.

The failure of the Physical Influence Scheme in eliminating the numerical instabilities is probably linked to the way the diffusive length is computed, as already discussed in the previous subsection. Although the Physical Influence Scheme was effective for the grid composed of prisms in Terzaghi's problem (Figure 6.21c), it did not perform as well for Mandel's problem, as shown in Figure 6.27c. This fact suggests that computing diffusive length for the prism as presented in Table 5.1 is not always suitable. The expression presented in Table 5.1 was derived for the face illustrated in Figure 5.4 for the prism, which is perpendicular to the triangular facets of this element. This very same expression was also used to compute the diffusive length of the other faces, including those faces parallel to the triangular facets of the prism, which is clearly incorrect and it does affect the performance of PIS. What prisms and pyramids have in common is that both of them are composed of triangular and quadrilateral facets, thus their internal faces are not all similar to each other. For instance, a pyramid have four triangular faces and four quadrilateral faces and a prism have four faces parallel and four faces perpendicular to its base. This suggests that particular expressions should be derived for each type of face. Interestingly enough, the internal faces of hexahedra and tetrahedra are all similar to each other so the same expression obtained for one face can be used for the other ones. Indeed, the results presented

**Figure 6.27** – Pressure field at $t = 3,0$ seconds.

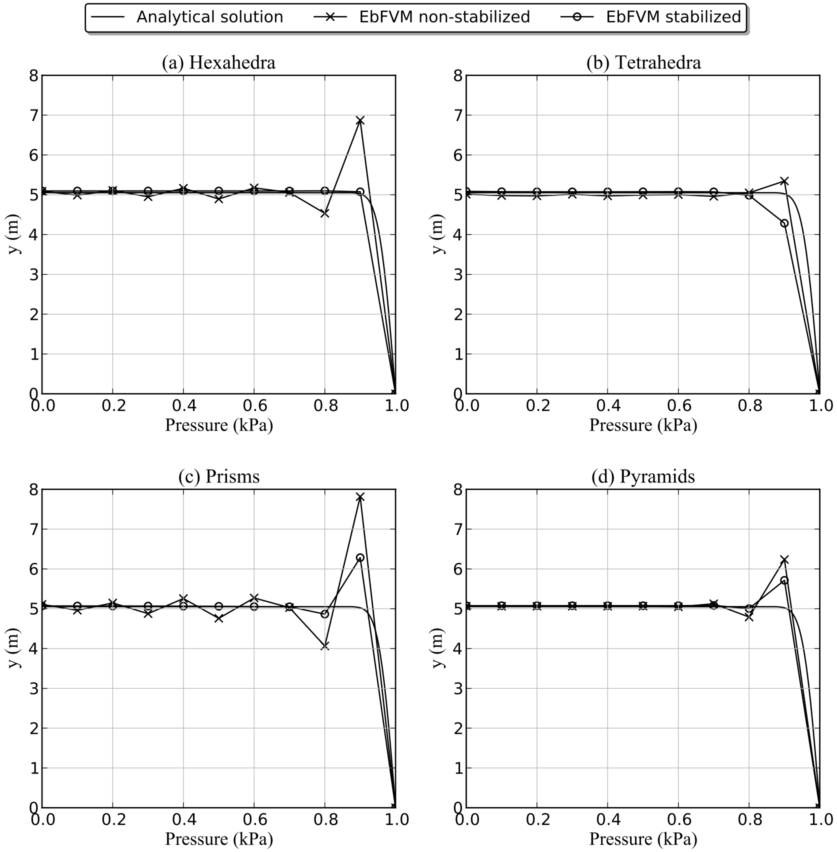

Source: Own authorship.

so far show that PIS effectively remove pressure wiggles for hexahedral and tetrahedral elements, even though the same expression for the diffusive length is used for all faces inside the element.

### 6.4.4 Strip-footing problem

By this time, the solution for the strip-footing problem is obtained at time $t = 0{,}01$ day, that is, 14 minutes and 24 seconds after the time dependent load started to be applied over the top surface, as indicated in Figure 6.9. The pressure fields obtained with both formulations are shown in Figure 6.28, where a three-dimensional oscillatory pattern can be observed for the non-stabilized formulation. By contrast, a smooth pressure field is obtained by using the Physical Influence Scheme.

By plotting the pressure solution along the vertical central line ($x = y = 0$ m), as in Figure 6.29, a more detailed comparison between the two solutions is possible. As it can be observed in this figure, although both formulations provide oscillation-free solutions along the sandy layer ($27{,}5 < z < 40{,}0$ m), pronounced non-physical pressure wiggles appear in the two silty clayey layers ($15{,}0 < z < 27{,}5$ m and $40{,}0 < z < 50{,}0$ m) and smaller oscillations can be identified in silty layer. By distinction,

**Figure 6.28** – Pressure field at $t = 0{,}01$ day.

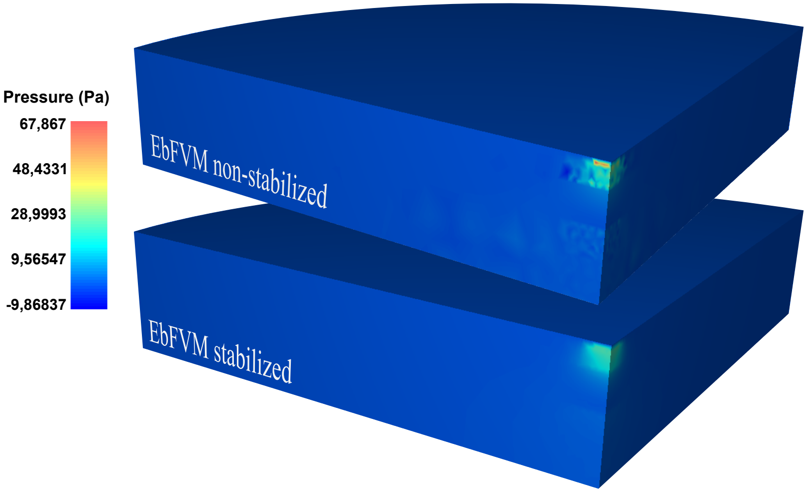

Source: Own authorship.

**Figure 6.29** – Strip-footing problem: pressure profiles along the center vertical line at $t = 0,01$ day.

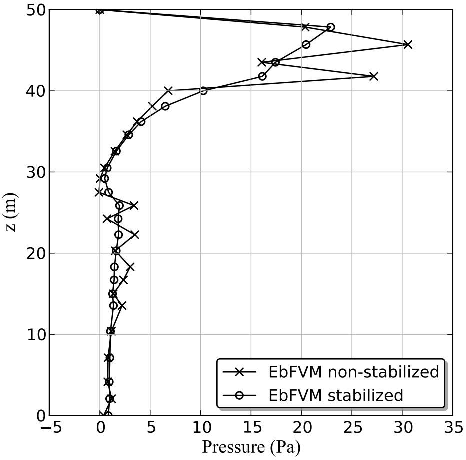

Source: Own authorship.

the stabilized EbFVM provides a smooth solution for the pressure profile along all layers. It must be kept in mind that — considering the numerical tests presented in the previous subsections and comparing the pressure profiles in Figure 6.29, specially in the two interfaces of the sandy layer — the stabilized solution, despite its smoothness, it probably present some degree of numerical diffusion.

## 6.4.5 Groundwater withdrawal

The time step size for the groundwater withdrawal problem is reduced to $\Delta t = 1 \times 10^{-4}$ day (or 8,64 seconds) and the numerical solutions obtained with the stabilized and non-stabilized formulations are taken at $t = 1 \times 10^{-3}$ day (1 minute and 26,4 seconds after beginning of production). It is interesting to notice that, although there is no external loads applied to the structure, numerical instabilities are observed in the regions immediately above and below the well, as presented in Figure 6.30. By distinction, the stabilized formulation effectively prevent the solution from spurious modes, as shown in Figure 6.30.

**Figure 6.30** – Pressure field at $t = 1 \times 10^{-3}$ day.

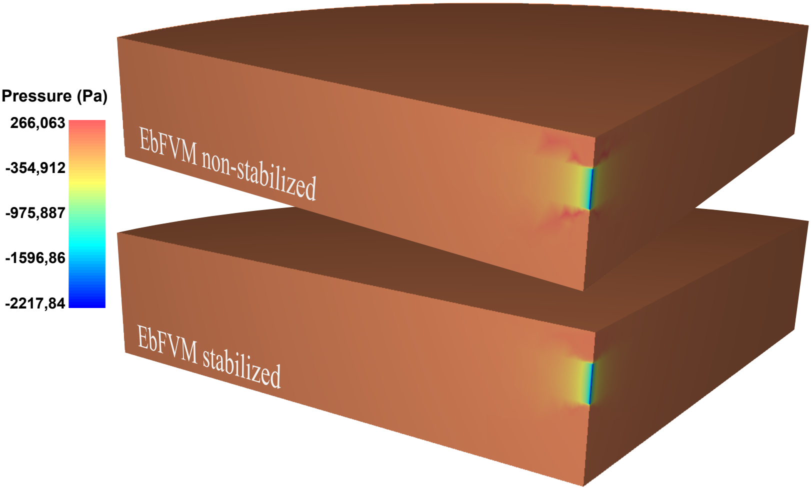

Source: Own authorship.

**Figure 6.31** – Groundwater withdrawal problem: pressure profiles along the center vertical line at $t = 1 \times 10^{-3}$ day.

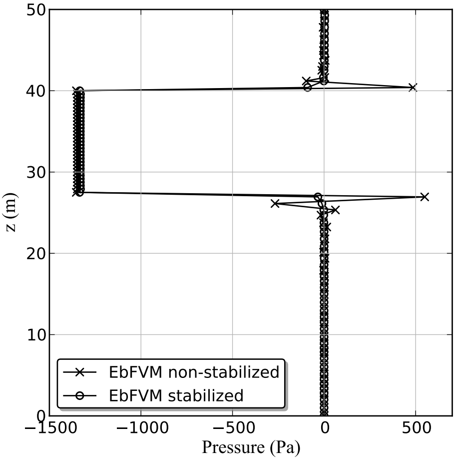

Source: Own authorship.

Figure 6.31 shows the pressure profiles along the vertical center line of the structure at time $t = 1 \times 10^{-3}$ day. A uniform pressure profile is obtained on the control volumes intercepted by the well (along the sandy layer), while the pressure in the adjacent layers are still not affected. It can be said that, by this time, the Noordbergum effect is not present yet since any positive pressure is observed in the adjacent layers. The important thing to be pointed out in Figure 6.31 is the pressure oscillations in the interfaces between the sandy layer and the upper and lower silty clayey layers obtained by the non-stabilized formulations, which are not observed when the Physical Influence Scheme is employed for evaluating the volumetric strains. Apart from these two regions, both formulations provided the same solutions, indicating that the additional terms introduced by the Physical Influence Scheme does not ruin the solution, but only prevent it from numerical instabilities.

CHAPTER

# 7

# CONCLUSION

A finite volume formulation has been proposed in this work for solving three-dimensional single-phase fluid flows in deformable porous media coupled with geomechanics. The partial differential equations of Biot's consolidation model have been discretized by the Element-based Finite Volume Method, thus resulting in a mass and momentum conservative numerical scheme. Moreover, the numerical formulation is able to handle unstructured grids composed of a combination of hexahedra, tetrahedra, prisms and pyramids, which provides great flexibility for discretizing specific regions of the domain.

The main contribution of this work has been to provide an alternative interpolation function that prevents the solution from numerical instabilities in the limiting case of undrained consolidation. This technique has been widely used for solving incompressible and compressible fluid flows governed by the Navier-Stokes equations, and its application to coupled poroelasticity is a novelty. The idea of using the Physical Influence Scheme in this work came to the surface by recognizing the similarities between the pressure-velocity coupling in general fluid flows and pressure-displacement coupling in poroelasticity. By this recognition, it was straightforward to realize that the problems encountered when solving the Navier-Stokes equations are the same as those that appear in poroelasticity under undrained conditions. As a consequence, the same techniques already advanced for obtaining stable solutions in fluid mechanics could be readily applied to geomechanics as well, which is the case of PIS.

As already discussed, during the discretization process the finite volume method requires the computation of the displacement vector at the integration points in order to account for the solid velocities. A natural procedure is to use the element shape functions to perform linear interpolations for the displacement field. However, since linear interpolations are also employed for the pore pressure field, this formulation is prone to suffer from numerical instabilities because this pair of approximations does not satisfy the LBB-condition. From a physical perspective, using the shape functions to evaluate the displacement vector at the integration points does not provide the necessary coupling between pressure and displacement, since it is not able to accurately capture the underlying physics of the problem.

By contrast, since the Physical Influence Scheme considers the stress equilibrium equations for obtaining an interpolation function for the displacements, it naturally considers the effects of the pressure gradient, which is claimed in this work to be an important piece of the puzzle. From another viewpoint, it has been shown that PIS provides a way of mimicking a third-order approximation for the displacement vector at the integration points, at least for one-dimensional problems. For the three-dimensional case the approximation probably falls somewhere in between second and third-order depending on how the diffusive lengths are computed. Additionally, although it seems to play a secondary role in consolidation problems, the term dropped from the stress equilibrium equations could somehow benefit the numerical scheme if it was considered in the interpolation function of PIS.

The numerical formulation obtained with PIS is referred to as the stabilized formulation, whereas the non-stabilized formulation refers to case where the displacements are interpolated by the element shape functions only. The results presented in chapter 6 reveals that both formulations provided virtually the same results in all test cases presented. This means that PIS is a consistent procedure since the stabilization terms vanish when the consolidation progresses deep enough into the formation (drained consolidation). These evidences where revealed by solving the classical Terzaghi's and Mandel's problems with analytical solutions to compare. In addition, the strip-footing problem with a time dependent load and a groundwater withdrawal problem in heterogeneous media have been solved, where some interesting effects of poromechanical coupling have been shown.

A convergence analysis has been carried out and, as expected, second-order approximations were observed for both pressure and displacements for the stabilized formulation, which is the reason it was stated that PIS only mimics a higher order approximation for displacements. In the sequence, critical situations were created for Terzaghi's and Mandel's problems and the stabilized and non-stabilized formulations were employed for obtaining the numerical solutions. These problems were solved with computational grids composed of only one type of element at a time in order to assess the performance of PIS in each case. The results showed that for hexahedral and tetrahedral elements the Physical Influence Scheme is able to completely remove the pressure wiggles, although some numerical diffusion is often observed. For prisms and pyramids, however, the pressure instabilities were reduced but not completely mitigated. The reason for this is probably the way the diffusive length has been computed for these two types of elements. As discussed in chapter 6, the internal faces of pyramids are not similar to each other (some of them are triangular and some are quadrangular). A similar situation happens for prisms. This point, along with the results obtained, leads to the conclusion that the procedure proposed for computing the diffusive length is not suitable for these two types of elements.

By distinction, hexahedral and tetrahedral elements have similar internal faces, so the expressions derived for on face can be readily applied for computing the diffusive length to the other ones. This statement is backed up by the results presented for the one-layered and two-layered poroelastic columns and Mandel's problems. In addition, grids mainly composed of tetrahedral elements were used for solving the strip-footing and the groundwater withdrawal problems under undrained consolidations, in which cases no instabilities at all were observed for the stabilized formulation. In fact, this discussion provides evidence of the importance of a proper evaluation of the diffusive length for obtaining oscillation-free solutions through the Physical Influence Scheme.

As a final conclusion, the EbFVM poses itself as interesting numerical scheme for solving coupled geomechanics as it is mass and momentum conservative and it provides great geometrical flexibility by employing hybrid unstructured grids. Additionally, the Physical Influence Scheme has been proven to be a promising alternative for stabilizing finite volume formulations for coupled poroelasticity problems.

## 7.1 Suggestions for future investigations

The discussion above provides some insights on possible investigation paths in the field of coupled geomechanics. Regarding stability issues, the performance of the Physical Influence Scheme can be improved by properly computing the diffusive lengths for prisms and pyramids. For pyramids, for example, different expressions for the diffusive length should be derived for the triangular and quadrangular faces. The same procedure should be carried out for prisms as well. In this manner, when computing the solid velocities the algorithm should identify the type of face being visited and use the proper expression for computing the diffusive length. This procedure might eliminate the pressure instabilities obtained with PIS when grids composed of prisms and pyramids are used.

Another interesting topic to be considered for future developments still regards to stabilization strategies. By recognizing the similarities between fluid mechanics and coupled geomechanics, another alternative for obtaining a physically consistent interpolation function for the displacement vector is to employ the Rhie–Chow technique. This strategy has been widely used for computing the face velocities for the mass conservation equation in fluid mechanics. Instead of discretizing the momentum equations at the integration point, as performed by PIS, Rhie–Chow considers the discretized momentum equations for the element vertices surrounding the integration point and computes an averaged discretized equation for the displacements at the integration point. Evidently, this procedure also considers the underlying physics of the problem since the interpolation function is also obtained by means of the momentum equations. In addition to carrying the pressure effects, this strategy would not disregard any term of the stress equilibrium equations, as PIS does. Moreover, since the interpolation function is obtained by an average of the discretized stress equilibrium equations of the element vertices, the Rhie–Chow method eliminates the necessity of computing diffusive lengths, which can be an advantage. The main concern of applying this technique, however, should be on the fact that it increases the stencil of pressure, which can be tricky to implement and reduce the efficiency of linear solvers.

From the viewpoint of oil and gas industries, it might be interesting to solve the geomechanical model on corner-point grids as well, since the reservoir simulators are based on this type of grids. Most of commercial reservoir simulators routinely used by oil and gas companies are based on corner-point grids because they are easier to build and produce sparse linear systems, which improves the efficiency of linear solvers. In this type of grids, the pore pressure (and eventually saturation or mass fractions) is stored at the barycenter of cells (cell-center method), and the mass conservation equation is built for each cell of the grid usually by a finite volume method. The stress equilibrium equations can also be computed for each cell of the grid using a finite volume formulation and the displacement vectors can be stored at the cell centers as well. Additionally, since this formulation might also suffer from numerical instabilities, the Physical Influence Scheme can be easily applied for computing the solid velocities at the cell faces. As a consequence, a robust and unified finite volume formulation would be obtained for solving coupled geomechanics in traditional reservoir simulators already used by oil and gas companies on a daily basis. It should be stressed, however, that this alternative goes in the opposite direction of employing unstructured grids for solving porous media flows, which seems to be a trend in the scientific community and also in some commercial reservoir simulators.

A clear drawback of giving up unstructured grids in favor of corner-point grids is that, although it is possible to locally refine specific cells of corner-point grids, it is not possible to build radial grids to better capture the flow patterns in the near-well region. Therefore, another possibility for future works could be to explore and highlight the potentialities of unstructured grids for solving the near-well region giving emphasis on the geomechanical effects for assessing wellbore stability. When high pressure gradients are involved, specially in this region, the

# REFERENCES

ALISADEGHI, H.; KARIMIAN, S. **Comparison of different solution strategies for collocated method of MCIM to calculate steady and unsteady incompressible flows on unstructured grids**. *Computers & Fluids*, v. 46, pp. 94–100, 2011.

BABUŠKA, I. **Error bounds for finite-element method**. *Numerische Mathematik*, v. 16, pp. 322–333, 1971.

BALAY, S.; ABHYANKAR, S.; ADAMS, M. F.; BROWN, J.; BRUNE, P.; BUSCHELMAN, K.; DALCIN, L.; EIJKHOUT, V.; GROPP, W. D.; KAUSHIK, D.; KNEPLEY, M. G.; MAY, D. A.; MCINNES, L. C.; RUPP, K.; SANAN, P.; SMITH, B. F.; ZAMPINI, S.; ZHANG, H.; ZHANG, H. **PETSc Users Manual**. Technical Report, Argonne National Laboratory, 2017.

BALAY, S.; ABHYANKAR, S.; ADAMS, M. F.; BROWN, J.; BRUNE, P.; BUSCHELMAN, K.; DALCIN, L.; EIJKHOUT, V.; GROPP, W. D.; KAUSHIK, D.; KNEPLEY, M. G.; MAY, D. A.; MCINNES, L. C.; RUPP, K.; SMITH, B. F.; ZAMPINI, S.; ZHANG, H.; ZHANG, H., 2017. PETSc Web page. http://www.mcs.anl.gov/petsc.

BALIGA, B. R. **A Control-Volume Based Finite Element Method for Convective Heat and Mass Transfer**. Ph.D. Thesis, University of Minnesota, 1978.

BERRYMAN, J. G. **Effective stress for transport properties of inhomogeneous porous rock**. *Journal of Geophysical Research: Solid Earth*, v. 97, n. B12, pp. 2156–2202, 1992.

BIOT, M. A. **General theory of three-dimensional consolidation**. *Journal of Applied Physics*, v. 12, pp. 155–164, 1941.

BIOT, M. A. **Theory of elasticity and consolidation for a porous anisotropic solid**. *Journal of Applied Physics*, v. 26, pp. 182–185, 1955.

BIOT, M. A. **Theory of deformation of a porous viscoelastic anisotropic solid**. *Journal of Applied Physics*, v. 27, pp. 459–467, 1956.

BIOT, M. A. **Theory of propagation of elastic waves in a fluid-saturated porous solid i. low frequency range**. *Journal of Acoustical Society of America*, v. 28, pp. 168–178, 1956.

BIOT, M. A.; WILLIS, D. G. **The elastic coefficients of the theory of consolidation**. *Journal of Applied Mechanics*, pp. 594–601, 1957.

BOTH, J.; BORREGALES, M.; NORDBOTTEN, J.; KUMAR, K.; RADU, F. **Robust fixed stress splitting for Biot's equations in heterogeneous media**. *Applied Mathematics Letters*, v. 68, pp. 101–108, 2017.

BREZZI, F. **On the existence of uniqueness and approximation of saddle-point problems arising from lagrangian multipliers**. *Revue Française d'Automatique Informatique et Recherche Operationnelle*, v. 8, pp. 129–151, 1974.

CASTELLETTO, N.; WHITE, J.; FERRONATO, M. **Scalable algorithms for three-field mixed finite element coupled poromechanics**. *J. Comput. Phys.*, v. 327, pp. 894–918, 2016.

CHOO, J.; BORJA, R. **A stabilized mixed finite elements for deformable porous media with double porosity**. *Computer Methods in Applied Mechanics and Engineering*, v. 293, pp. 131–154, 2015.

COMERLATI, A.; FERRONATO, M.; GAMBOLATI, G.; PUTTI, M.; TEATINI, P. **Saving Venice by seawater**. *Journal of Geophysical Research*, v. 109, 2004.

COUSSY, O. **Poromechanics**. J. Wiley & Sons Ltd., 2004.

COUSSY, O. **Mechanics and Physics of Porous Solids**. J. Wiley & Sons Ltd., 2010.

CRYER, C. **A comparison of the three dimensional consolidation theories of Biot and Terzaghi**. *Quaterly Journal of Mechanics and Applied Mathematics*, v. 4, pp. 401–412, 1963.

DAL PIZZOL, A. **Análise dos efeitos geomecânicos na simulação de reservatórios**. Master's Thesis, Universidade Federal de Santa Catarina, 2013.

DAL PIZZOL, A. **Análise dos efeitos geomecânicos na simulação de reservatórios**. Master's Thesis, Universidade Federal de Santa Catarina, 2013.

DAL PIZZOL, A.; MALISKA, C. R. **A finite volume method for the solution of fluid flows coupled with the mechanical behavior of compacting porous media**. *Porous Media and its Applications in Science, Engineering and Industry,* v. 1453, pp. 205–210, 2012.

DETOURNAY, E.; CHENG, A. H. D. **Fundamentals of poroelasticity**. *Comprehensive Rock Engineering: Principles, Practice and Projects,* v. 2, pp. 113–171, 1993.

FERRONATO, M.; GAMBOLATI, G.; PUTTI, M.; TEATINI, P. **A diffusion model for land subsidence**. *In P.J. Binning et al. (eds.), Proceedings of the XVI International Conference on Computational Methods in Water Resources,* Copenhagen, Denmark, 2006.

FERRONATO, M.; CASTELLETTO, N.; GAMBOLATI, G. **A fully coupled 3-d mixed finite element model of Biot consolidation**. *Journal of Computational Physics,* v. 229, pp. 4813–4830, 2010.

FREY, P. J.; GEORGE, P. L. **Mesh generation: application to finite elements**, paris, france edition. Hermes Science Publications, 2000.

GAMBOLATI, G.; FERRONATO, M.; JANNA, C. **Preconditioners in computational geomechanics: A survey**. *Int. J. Numer. Anal. Meth. Geomech.,* v. 35, pp. 980–996, 2011.

GERSEVANOV, N. M. **Dynamika Gruntovoii Mass**. *Gosstroiizdat, Moscow,* 1934.

GUTIERREZ, M.; LEWIS, R.; MASTERS, I. **Petroleum reservoir simulation coupling fluid flow and geomechanics**. *Society of Petroleum Engineers,* v. 4, pp. 164–172, 2001.

GUZMÁN, J.; SALGADO, A.; SAYAS, F. **A note on the Ladyžhenskaya-Babuška-Brezzi condition**. *J. Sci. Comput.,* v. 56, pp. 219–229, 2013.

HORNBY, A. S. **Oxford Advanced Learning Dictionary of Current English**, sally wehmeier edition. Oxford University Press, 2000.

HURTADO, F. S. V. **Formulação tridimensional de volumes finitos para simulação de reservatórios de petróleo com malhas não-estruturadas híbridas**. Ph.D. Thesis, Universidade Federal de Santa Catarina, 2011.

JANNA, C.; FERRONATO, M.; GAMBOLATI, G. **Enhanced block FSAI preconditioning using domain decomposition techniques**. *SIAM J. Sci. Comput.*, v. 35, pp. 229–249, 2013.

KARIMIAN, S.; SCHNEIDER, G. **Numerical solution of two-dimensional incompressible Navier-Stokes equtions: treatment of velocity-pressure coupling**. *25th AIAA Fluid Dynamics Conference*, Colorado Springs, CO U.S.A., 1994.

KARIMIAN, S.; SCHNEIDER, G. **Pressure-based control-volume finite element method for flow at all speeds**. *AIAA Journal*, v. 44, 1995.

KIM, J.; PARIZEK, R. **Numerical simulation of the Noordbergum effect resulting from groundwater pumping in a layered aquifer system**. *J. Hydrol.*, v. 202, pp. 231–243, 1997.

LEWIS, R. W.; SCHREFLER, B. A. **The Finite Element Method in the Static and Dynamic Deformation and Consolidation of Porous Media**, 2nd edition edition. J. Wiley & Sons Ltd., 1999.

MAJUMDAR, S. **Development of a finite volume procedure for prediction of fluid flow problems with complex irregular boundaries**. *NASA STI/Recon Technical Report N*, v. 87, December, 1986.

MALISKA, C. R. **Transferência de Calor e Mecânica dos Fluidos Computacional**, $2^{a}$ edição edition. LTC Editora, 2004.

MALISKA, C. R.; SILVA, A. F. C.; HURTADO, F. S. V.; DONATI, C. N.; PESCADOR JR., A. V. B. **Manual de classes da biblioteca EFVLib**. Technical Report, Departamento de Engenharia Mecânica - Universidade Federal de Santa Catarina. Florianópolis - Brasil, 2011.

MANDEL, J. **Consolidation des sols**. *Géotechnique*, v. 3, pp. 287–299, 1953.

MARCHI, C. H.; MALISKA, C. R. **A nonorthogonal finite-volume method for the solution of all speed flows using co-located variables**. *Numerical Heat Transfer, Part B*, v. 26, pp. 293–311, 1994.

MURAD, M.; LOULA, A. **Improved accuracy in finite element analysis of Boit's consolidation problem**. *Comp. Meth. Appl. Mech. Eng.*, v. 95, pp. 359–382, 1992.

MURAD, M.; LOULA, A. **On stability and convergence of finite element approximation of Biot's consolidation problem**. *Int. J. Numer. Eng.*, v. 37, pp. 645–668, 1994.

NORDBOTTEN, J. **Cell-centered finite volume discretizations for deformable porous media**. *Int. J. Numer. Meth. Engng.*, v. 100, pp. 399–418, 2014.

NORDBOTTEN, J. **Convergence of a cell-centered finite volume discretization for linear elasticity**. *SIAM J. Numer. Anal.*, v. 53, pp. 2605–2625, 2015.

NORDBOTTEN, J. **Stable cell-centered finite volume discretization for Biot equations**. *SIAM J. Numer. Anal.*, v. 54, pp. 942–968, 2016.

OÑATE, E. **Derivation of stabilized equations for numerical solution of advective-diffusive transport and fluid flow problems**. *Computer Methods in Applied Mechanics and Engineering*, v. 151, pp. 233–265, 1998.

OÑATE, E.; ROJEK, J.; TAYLOR, R. L.; ZIENKIEWICZ, O. **Finite calculus formulation for incompressible solids using linear triangles and tetrahedra**. *International Journal of Numerical Methods in Engineering*, v. 59, pp. 1473–1500, 2004.

PATANKAR, S. V. **Numerical Heat Transfer and Fluid Flow**. Hemisphere Publishing Corporation, 1980.

PEACEMAN, D. **Interpretation of well-block pressures in numerical reservoir simulation with nonsquare grid blocks and anisotropic permeability**. *SPE Journal*, v. 23, pp. 531–543, 1983.

PEREIRA, L. C.; GUIMARÃES, L. J. N.; HOROWITZ, B.; SÁNCHEZ, M. **Coupled hydro-mechanical fault reactivation analysis incorporating evidence theory for uncertainty quantification**. *Computers and Geotechnics*, v. 56, pp. 202–215, 2014.

PERIC, M. **A finite volume method for the prediction of three-dimensional fluid flow in complex ducts**. Ph.D. Thesis, University of London, London, UK, 1985.

PHILLIPS, P.; WHEELER, M. **A coupling of mixed and continuous Galerkin finite element methods for poroelasticity I: the continuous-in-time case**. *Comput. Geosci.*, v. 11, pp. 131–144, 2007.

PHILLIPS, P.; WHEELER, M. **A coupling of mixed and continuous Galerkin finite element methods for poroelasticity II: the continuous-in-time case**. *Comput. Geosci.*, v. 11, pp. 145–158, 2007.

PREISIG, M.; PRÈVOST, J. H. **Stabilization procedures in coupled poromechanics problems: A critical assessment**. *International Journal for Numerical and Analytical Methods in Geomechanics*, v. 35, pp. 1207–1225, 2011.

REED, M. **An investigation of numerical errors in the analysis of consolidation by finite elements**. *Int. J. Numer. Anal. Methods Geomech*, v. 8, pp. 243–257, 1984.

RHIE, C. M.; CHOW, W. L. **Numerical study of the turbulent flow past an airfoil with trading edge separation**. *AIAA J.*, v. 21, pp. 1525–1535, 1983.

RIBEIRO, G. **Volumes finitos baseado em elementos para problemas de poroelasticidade**. Ph.D. Thesis, Universidade Federal de Santa Catarina, 2016.

RICE, J. R.; CLEARY, M. P. **Some basic stress diffusion solutions for fluid saturated elastic porous media with compressible constituents**. *Reviews of Geophysics and Space Physics*, v. 14, pp. 227–241, 1976.

RODRIGO, C.; GASPAR, F.; HU, X.; ZIKATANOV, L. **Stability and monotonicity for some discretizations of Biot's consolidation model**. *Computer Methods in Applied Mechanics and Engineering*, v. 298, pp. 183–204, 2016.

ROOSE, T.; NETTI, P. A.; MUNN, L. L.; BOUCHER, Y.; JAIN, R. K. **Solid stress generated by spheroid growth estimated using linear poroelasticity model**. *Microvascular Research*, v. 66, pp. 637–652, 2003.

SCHNEIDER, G.; KARIMIAN, S. **Advances in control-volume-based finite-element methods for compressible flows**. *Computational Mechanics*, v. 14, pp. 431–446, 1994.

SCHNEIDER, G. E.; RAW, M. J. **Control volume finite-element method for heat transfer and fluid flow using colocated variables - 1. computational procedure**. *Numerical Heat Transfer*, v. 11, pp. 363–390, 1987.

SHAW, G.; STONE, T. **Finite volume methods for coupled stress/fluid flow in commercial reservoir simulators**. *SPE Reservoir Simulation Symposium*, Houston, Texas U.S.A., 2005.

SWAN, C. C.; LAKES, R. S.; BRAND, R. A.; STEWART, K. J. **Micromechanically based poroelastic modeling of fluid flow in haversian bone**. *Journal of Biomechanical Engineering*, v. 125, pp. 25–37, 2003.

TCHONKOVA, M.; PETERS, J.; STURE, S. **A new mixed finite element method for poro-elasticity**. *Int. J. Numer. Anal. Methods Geomech.*, v. 32, pp. 579–606, 2008.

TEATINI, P.; CASTELLETTO, N.; FERRONATO, M.; GAMBOLATI, G.; JANNA, C.; CAIRO, E.; MARZORATI, D.; COLOMBO, D.; FERRETTI, A.; BAGLIANI, A.; BOTTAZZI, F. **Geomechanical response to seasonal gas storage in depleted reservoirs: A case study in the Po River basin, Italy**. *Journal of Geophysical Research*, v. 116, 2011.

TERZAGHI, K. **Die berechnung der durchlassigkeitsziffer des tones aus dem verlauf der hydrodynamischen spannungsercheinungen**. *Sitz. Akad. Wissen. Wien. Math. Naturwis*, v. 2a, pp. 125–128, 1923.

TRUTY, A.; ZIMMERMANN, T. **Stabilized mixed finite element formulations for materially nonlinear partially saturated two-phase media**. *Computer Methods in Applied Mechanics and Engineering*, v. 195, pp. 1517–1546, 2006.

VERMEER, P.; VERRUIJT, A. **An accuracy condition for consolidation by finite elements**. *International Journal of Numerical and Analytical Methods in Geomechanics*, v. 5, pp. 1–14, 1981.

VERRUIJT, A. **Elastic storage of aquifers**. *in: R. De Wiest, (Ed.), Flow Through Porous Media, Academic Press, New York (NY)*, pp. 331–376, 1969.

VERRUIJT, A. **Theory and problems of poroelasticity**. Delft University of Technology, Netherlands, 2016.

WHITE, J.; BORJA, R. **Stabilized low-order finite elements for coupled soliddeformation/fluid-diffusion and their application to fault zone transients**. *Computer Methods in Applied Mechanics and Engineering*, v. 197, pp. 4353–4366, 2008.

YANG, D.; MORIDIS, G.; BLASINGAME, T. **A fully coupled multiphase flow and geomechanics solver for highly heterogeneous porous media**. *Journal of Computational and Applied Mathematics*, Available online 22 December, 2013.

ZIENCKIEWICZ, O.; CHAN, A.; PASTOR, M.; PAUL, D.; SHIOMI, T. **Static and dynamic behaviour of soil: a rational approach to quantitative solutions. I. Fully saturated problems**. *Proc. R. Soc. Lond. A*, v. 429, pp. 285–309, 1990.

APPENDIX

# A

# ANALYTICAL SOLUTIONS

## A.1 One-layered poroelastic column

For a one-dimensional poroelastic column with height $H$ and the origin of the vertical z-axis placed at the bottom of the column, as in Figure 6.4, the analytical pressure and vertical displacement profiles, according to Verruijt (2016), are,

$$p(z,t) = \frac{4\gamma\sigma_T}{\pi}\sum_{i=0}^{\infty}\frac{1}{2i+1}\exp\left[-\frac{(2i+1)^2\pi^2 c\,t}{4H^2}\right]\sin\left[\frac{(2i+1)\pi(H-z)}{2b}\right] \tag{A.1}$$

and

$$\begin{aligned} u_z(z,t) = u_{z,0} + \frac{(1-2\nu)\alpha\gamma\sigma_T}{2G(1-\nu)}\Bigg\{ z - \frac{8H}{\pi^2}\sum_{i=0}^{\infty}\frac{1}{(2i+1)^2} \\ \exp\left[-\frac{(2i+1)^2\pi^2 c\,t}{4H^2}\right]\cos\left[\frac{(2i+1)\pi(H-z)}{2H}\right]\Bigg\} \end{aligned} \tag{A.2}$$

where the consolidation coefficient is defined as:

$$c = \frac{2kG(1-\nu)(\nu_u-\nu)}{\mu\alpha^2(1-\nu_u)(1-2\nu)^2} \tag{A.3}$$

with $\nu$ being the Poisson's coefficient and $\nu_u$ the undrained Poisson's coefficient, compute as $\nu_u = [3\nu + \alpha B(1-2\nu)]/[3-\alpha B(1-2\nu)]$. The Skempton's coefficient is defined as $B = \alpha M/K_u$ and the undrained bulk modulus is $K_u = \lambda + 2G/3 + \alpha^2 M$. Finally, $\gamma = B(1+\nu_u)/[3(1-\nu_u)]$.

## A.2 Two-layered poroelastic column

In this case, the origin of the coordinate system is placed at the interface between the two materials. As depicted in Figure 6.22, the upper and lower layers have heights $H_1$ and $H_2$, respectively. According to Verruijt (2016), the analytical pressure profile for $z < 0$ is given by,

$$\frac{p(z,t)}{p_0} = 2\sum_{i=0}^{\infty} \frac{1}{R_i} \exp\left(-\frac{A_i^2 t}{t_1}\right) \left[\cos(A_i)\cos\left(\frac{A_i z}{H_1}\right) - \sin(A_i)\sin\left(\frac{A_i z}{H_1}\right)\right] \tag{A.4}$$

and for $z > 0$,

$$\frac{p(z,t)}{p_0} = 2\sum_{i=0}^{\infty} \frac{1}{R_i} \exp\left(-\frac{A_i^2 t}{t_1}\right) \left[\cos(A_i)\cos\left(\frac{\beta A_i z}{H_1}\right) - \omega \sin(A_i)\sin\left(\frac{\beta A_i z}{H_1}\right)\right] \tag{A.5}$$

where,

$$R_i = A_i \left[(1-\omega\beta)\cos(\beta A_i)\sin(A_i) + (\omega+\beta)\sin(\beta A_i)\cos(A_i)\right] \tag{A.6}$$

and $A_i$ are the roots of,

$$\omega \sin(\beta A_i)\sin(A_i) - \cos(\beta A_i)\cos(A_i) = 0 \tag{A.7}$$

The time consolidations are,

$$t_1 = \frac{H_1^2}{c_1}; \qquad t_2 = \frac{H_2^2}{c_2} \tag{A.8}$$

and $\beta = \sqrt{t_2/t_1}$. The consolidation coefficients $c_1$ and $c_2$ are defined by Equation A.3 with the corresponding poromechanical properties of the two layers.

## A.3 Mandel's problem

For Mandel's problem, the initial conditions $p_0$ and $u_{y,0}$ are given by:

$$p_0 = p\left(x,z,0\right) = \frac{1}{3L} B\left(1+\nu_u\right) \tag{A.9}$$

$$u_{y,0} = u_y\left(y,z,0\right) = \frac{F\,\nu_u\, y}{2GL} \tag{A.10}$$

where $F$ is the force applied to the top boundary. The analytical solution reads:

$$p(y,z,t) = 2p_0 \sum_{i=1}^{\infty} \frac{\sin A_i}{A_i - \sin A_i \cos A_i} \left(\cos \frac{A_i\, y}{L}\right) \exp\left(-\frac{A_i^2 c\, t}{L^2}\right) \tag{A.11}$$

$$\begin{aligned} u_y(y,z,t) = {} & \frac{F\,\nu y}{GL} - 2u_{y,0} \sum_{i=0}^{\infty} \frac{\sin A_i \cos A_i}{A_i - \sin A_i \cos A_i} \exp\left(-\frac{A_i^2 c\, t}{L^2}\right) \\ & + \frac{F}{G} \sum_{i=0}^{\infty} \frac{\cos A_i}{A_i - \sin A_i \cos A_i} \sin\left(\frac{A_i\, y}{L}\right) \exp\left(-\frac{A_i^2 c\, t}{L^2}\right) \end{aligned} \tag{A.12}$$

where $A_i$ are computed as the positive roots of:

$$\nu A_i + \left(\nu_u - \nu\right) \tan A_i = 0. \tag{A.13}$$

APPENDIX

# B

# WELL MODEL

## B.1 Peaceman's model

Considering a vertical well fully penetrating a porous matrix with isotropic permeability in the radial direction, according to Peaceman (1983) the well index for the $i$-th control volume intercepted by the well can be computed as:

$$WI_i = \frac{2\pi k \Delta z_i}{\ln\left(r_{eq}/r_w\right)}, \tag{B.1}$$

where $\Delta z_i$ is the vertical length of the control volume $i$, $k$ is the permeability in the horizontal direction and $r_{eq}$ is the equivalent radius. The analytical solution for the radial pressure field evaluated at the point $r_{eq}$ should provide the same pressure numerically obtained for the control volume $i$. For a cubic control volume with dimensions $\Delta x$, $\Delta y$ and $\Delta z$, Peaceman (1983) concluded that the equivalent radius should be computed by:

$$r_{eq} = \sqrt{\Delta x^2 + \Delta y^2}. \tag{B.2}$$

Since the control volumes constructed by the EbFVM rarely present a cubic form, the values of $\Delta x$ and $\Delta y$ of equations (B.2) are not directly computed. Instead, knowing the volume $\Delta\Omega_i$ and the control volume height, $\Delta z_i$, they are computed as:

$$\Delta x_i = \Delta y_i = \sqrt{\frac{\Delta\Omega_i}{\Delta z_i}}. \tag{B.3}$$

Therefore, the equivalent radius is calculated by the expression:

$$r_{eq} = \sqrt{2\frac{\Delta\Omega_i}{\Delta z_i}}. \tag{B.4}$$

APPENDIX

# C

# SOLID PHASE DENSITY DERIVATIVE

Consider the porous element depicted in Figure C.1 subjected to an infinitesimal and isotropic total stress $\delta\sigma$. The solid grains have a compressibility $c_s$ and the fluid filling the pore channels has the compressibility denoted by $c_f$. The bulk volume of the element is represented by $V_b$.

**Figure C.1** – Porous element.

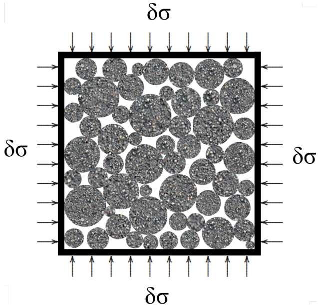

Source: Adapted from Verruijt (2016).

As discussed in Verruijt (2016), a variation in the solid phase volume, $\delta V_s$, is due to a pore pressure variation, $\delta p$, and to an effective stress variation, $\delta\sigma + \delta p$. This is represented by the following expression:

$$\delta V_s = -\left(1-\phi\right) c_s \delta p V_b + \left(\delta\sigma + \delta p\right) c_s V_b. \tag{C.1}$$

The porosity is defined such that the volume of the solid phase is given by:

$$V_s = \left(1-\phi\right) V_b, \tag{C.2}$$

thus, Equation C.1 becomes:

$$\left(1-\phi\right) \frac{\delta V_s}{V_s} = c_s \left(\delta\sigma + \phi \delta p\right). \tag{C.3}$$

Additionally, the solid phase compressibility is defined as:

$$c_s = -\frac{1}{V_b} \left.\frac{\delta V_b}{\delta p}\right|_{\delta\sigma'=0} = \frac{1}{\rho_s} \frac{\delta \rho_s}{\delta p}, \tag{C.4}$$

which implies that,

$$\frac{\delta V_b}{V_b} = -\frac{\delta \rho_s}{\rho_s}. \tag{C.5}$$

Furthermore, using the definition of Equation C.2, then

$$\frac{\delta V_b}{V_b} = \frac{\left(1-\phi\right)}{\left(1-\phi\right)} \frac{\delta V_s}{V_s} \quad \therefore \quad \frac{\delta V_s}{V_s} = -\frac{\delta \rho_s}{\rho_s}. \tag{C.6}$$

Substituting Equation C.6 into Equation C.3 and rearranging the terms leads to:

$$\delta \rho_s = -\frac{\rho_s c_s}{\left(1-\phi\right)} \left(\delta\sigma + \phi \delta p\right). \tag{C.7}$$

Finally, by taking the time derivative on both sides of Equation C.7, the following expression is obtained:

$$\frac{\partial \rho_s}{\partial t} = -\frac{\rho_s c_s}{\left(1-\phi\right)} \left(\frac{\partial \sigma}{\partial t} + \phi \frac{\partial p}{\partial t}\right). \tag{C.8}$$